④

AFGL-TR-89-0011

A Dynamic Model for Forecasting New Cloud Development

William R. Cotton
Ray McAnelly
Craig Tremback
Robert Walko

Aster, Inc.
P.O. Box 466
Ft. Collins, CO 80522

19 December 1988

Final Report
1 November 1987-19 December 1988

Approved for public release; distribution unlimited

AIR FORCE GEOPHYSICS LABORATORY
AIR FORCE SYSTEMS COMMAND
UNITED STATES AIR FORCE
HANSCOM AIR FORCE BASE, MASSACHUSETTS 01731-5000

This technical report has been reviewed and is approved for publication.

Gerald L Freeman
GERALD L. FREEMAN, Captain, USAF
Contract Manager

Donald A Chisholm
DONALD A. CHISHOLM, Chief
Atmospheric Prediction Branch

FOR THE COMMANDER

Robert A. McClatchey
ROBERT A. McCLATCHEY, Director
Atmospheric Sciences Division

This report has been reviewed by the ESD Public Affairs Office (PA) and is releasable to the National Technical Information Service (NTIS).

Qualified requestors may obtain additional copies from the Defense Technical Information Center. All others should apply to the National Technical Information Service.

If your address has changed, or if you wish to be removed from the mailing list, or if the addressee is no longer employed by your organization, please notify AFGL/DAA, Hanscom AFB, MA 01731. This will assist us in maintaining a current mailing list.

Do not return copies of this report unless contractual obligations or notices on a specific document require that it be returned.

TABLE OF CONTENTS

Dynamic Model for Forecasting New Cloud Development

William R. Cotton, Robert L. Walko, Craig J. Tremback, and Ray McAnelly
ASTeR, Inc.
P.O.Box 466
Fort Collins, CO 80521

March 2, 1989

1 Introduction

The primary goal of this research is to develop a mesoscale model capable of predicting regions of convective outbreak. The model is to be initialized by a simple sounding(s) and during the data assimilation period single Doppler radar data are to be assimilated into the model fields. The model should be capable of producing forecasts of convective development on a mini-computer system. The model should cover a 100 km by 100 km domain with a minimum resolution of 5 km. The benchmark mini-computer system used for model development is the DEC Micro-Vax II. The basic model used for this study is the Colorado State University Regional Atmospheric Modeling System(RAMS). The overall features of RAMS are described in Appendix A. In the following sections we describe the various versions of RAMS that have been developed for this project, the methods of four-dimensional assimilation of single Doppler radar data, preliminary testing and evaluation procedures and results. We then describe the real data cases used to test the model, the methods of single Doppler wind retrieval, and the results of testing the model in several cases. We conclude with an overall summary of results and recommendations for future research.

[illegible]

2 Model development

Two versions of the Regional Atmospheric Modelling System (RAMS) were employed for this study. These were (1) a simplified version of the full hydrostatic model with fewer grid points than usually used in a research mode and (2) a mixed layer model developed for this project, similar to the models of Lavoie (1972) and Keyser and Anthes (1977). The two model versions were developed in parallel as it was recognized from the beginning of the project that each configuration had advantages and disadvantages when compared to each other. If execution speed were not a factor, the full model would obviously have been the choice. One of the advantages of the full model is that it incorporates far fewer approximations than the mixed layer model. However, the full model cannot be simplified enough to attain one of the stated goals of this study which is to produce a forecast in 1/6 real time on a MicroVAX II class computer system,which is rated at about 1 million instructions per second (MIPS), and to achieve this speed with the horizontal domain setup of 100 km by 100 km total size and a 5 km resolution. The mixed layer model, on the other hand, has the advantages of computer speed and simplicity. These model versions will be described below.

A. The Hydrostatic Full Numerical Prediction Model

The full model version uses the complete hydrostatic model equation set from RAMS. This set includes prognostic equations for the u and v wind components, potential temperature, and vapor mixing ratio (as a passive tracer only) and diagnostic equations for vertical velocity and pressure. The simplifications necessary for this project include the choice of the simplest numerical schemes and parameterizations that would perform adequately. In addition, a couple of the schemes needed to be modified for the limited height of the domain. Some of these simplifications and modifications are:

1. The number of vertical levels needed to be reduced. This limited the vertical extent

of the atmosphere which could be modelled. A domain of about 4 km depth with 6 layers was first used. The vertical grid spacing was 400 m near the ground, stretched to 750 m near the model top. Also, the number of levels in the soil model was reduced from the usual 11 to 4.

2. The simplest forms of the model numerical schemes needed to be used. These included the second-order advection scheme rather than a sixth order, a constant pressure top boundary condition for the hydrostatic equation, and a radiative lateral boundary condition with a specified phase velocity.

3. The diffusion calculations were modified to reduce the number of calculations involved. For instance, only the vertical shear was used to compute the deformation rather than the three dimensional shear.

4. The radiative parameterizations needed to be modified to account for the atmosphere above the model domain. In the research model, the domain usually extends well into the stratosphere which will account for almost all of the mass of the atmosphere. Since the domain in this case covers only the lower portion of the atmosphere, especially the long wave radiation needed to have information from the remainder of the atmosphere. The long wave parameterization was modified to use the thermal information from the input sounding along with the actual model domain.

5. The convective parameterization also needs information from all of the troposphere and the lower stratosphere. This scheme was also modified to use information from the input sounding.

This model configuration was run successfully in several situations. The convective boundary layer was handled well and realistic slope flows were developed with a ridge-plain topography. The goal of 1/6 real time was not quite realized; the simplified model did achieve 1/5 real time on a MicroVAX II.

However, problems began to arise when the model boundary layer velocity fields were nudged to several generic "observed" fields meant to simulate Doppler observations. As an example of these problems, consider the case of a low level stationary convergence line that is homogeneous in the north-south direction. In the east-west direction, the wind changed from 5 m/s to -5 m/s over a 20 km region in the center of the 100 km domain.

Unlike the mixed layer model, the full model has to satisfy the various physical constraints imposed by the equations, such as mass continuity. When a convergent field is imposed at low levels, the model response is to increase pressure in the center of the domain and force an upward vertical motion. The high pressure forces a compensating outflow above the inflow layer with subsidence occurring on a larger scale than the convergent region. The full model has problems with numerical stability and mass trending if all the parts of the circulation (inflow, outflow, subsidence) are not included in the model domain. In the model configuration required by the computer speed, this was the case. The domain was not deep enough to adequately resolve the outflow and not wide enough for the subsidence to be contained within the domain. The mean domain pressure increased to the point where numerical instability resulted.

Several changes could be made to the model configuration for the nudging to maintain stability. More grid points can be added both horizontally and vertically to increase the size of the domain. Obviously, the 1/6 real time goal on a MicroVAX II would not be realized as, along with the increased number of grid points, the timestep length would also need to be lowered since the phase velocity of the modelled external gravity wave is dependent on the height of the model top. Another option is to lower the resolution so as to expand the area of the domain, but with the expected loss of detail of the modelled circulations. In the validation simulations described below, the 5 km resolution is retained, but more grid points were added. For the real-data simulations, the model was used on a 100 km by 100 km domain to compare it with the mixed-layer model. The domain for both the real-data and validation simulations was increased to about 6 km vertically by adding 2 additional vertical levels. This model configuration executed in about 1/4 real time.

It appears that to attain 1/6 real time forecasts on a MicroVAX II speed machine with a 100 by 100 km domain and a 5 km resolution, the mixed layer version of RAMS must be used. However, if a faster machine is available, a more complete model version can be used which has many fewer approximations than the mixed layer model.

B. The Mixed-Layer Model

The mixed-layer-model (MLM) version of RAMS was developed from similar models described in Lavoie (1972), Keyser and Anthes (1977), and Anthes et al. (1982). The latter two references have been followed most closely in designing the RAMS version. A prognostic equation for moisture, which was only found in the first reference, has been included here also.

The purpose of a MLM is to simplify the full 3-dimensional model equation set by taking into account certain gross features in the vertical structure of the atmosphere. Obviously, this limits the applicability of the model to those problems having approximately the vertical structure assumed in this model. The assumed structure in particular consists of a superadiabatic surface layer 50 or so meters deep, a neutral mixed layer above having constant vertical profiles of momentum, potential temperature, and water mixing ratio, a possible inversion of zero vertical thickness capping the mixed layer, and a stable layer above them all. Some level within the upper stable layer is called the "undisturbed level" and is assumed to be the highest level (as a function of time) to which any perturbations generated in the layers below have penetrated. The best known atmospheric situation which is well described by this structure is the developing convective planetary boundary layer.

Under the assumption of this vertical structure, six prognostic variables fully describe the time varying atmospheric state at all heights below the undisturbed level. They are (1) the potential temperature of the mixed layer, (2) the total water mixing ratio of the mixed layer, (3) the westerly wind component in the mixed layer, (4) the southerly wind component in the mixed layer, (5) the potential temperature immediately above the inversion capping the mixed layer, and (6) the height of the mixed layer top. The field values applying at the undisturbed level H are obtained from the initial sounding, and all quantities are assumed to vary linearly between H and the mixed-layer top. H itself is diagnosed from the mixed-layer height, and vertical velocities are diagnosed from the continuity equation based on the mixed-layer horizontal wind components, the base state density field, and the surface topography.

The assumptions about the vertical structure of the atmosphere permit the full 3-dimensional primitive equations to be integrated vertically and thereby reduced to two dimensions. Thus, only a single vertical level needs to be predicted. The prognostic equations for the mixed-layer variables include the forcing terms for horizontal advection, horizontal diffusion, the horizontal pressure gradient force, the Coriolis force, surface fluxes, entrainment fluxes at the mixed layer top, convective parameterization to prevent a superadiabatic layer from developing at the mixed layer top, and a nudging term for assimilating Doppler-radar-observed horizontal winds.

In order to run the cumulus parameterization of the RAMS model (this is distinct from the convective parameterization for the mixed layer top), 3-dimensional fields are reconstructed from the prognostic and diagnostic mixed layer fields and their assumed vertical structure, and are written into the regular RAMS model 3-dimensional fields in the applicable vertical levels. The cumulus parameterization is then run directly from the latter fields.

The mixed-layer option was designed to be totally unobtrusive on the RAMS model; it requires nothing from the basic model which is not already provided except for a few additional parameters defined in the input namelist. No new arrays need to be dimensioned to run in the MLM mode as sufficient array space is already available. Since running RAMS in MLM mode turns off the prognostic equations for the 3-dimensional model variables, the RAMS tendency arrays FU, FV, FW, FP, and FTH are not needed elsewhere. The MLM code has thus adopted these arrays for nearly all its storage requirements. A minimum of six vertical levels and nine gridpoints in each horizontal direction must be dimensioned in RAMS to provide adequate space for the MLM.

Many of the regular RAMS namelist variables have no function in the MLM and may be ignored when running in that mode. Those not needed in the MLM are indicated in the namelist documentation.

Some comments concerning the variables not needed to run RAMS in MLM mode are the following. The MLM has no soil model or radiation parameterization, and uses its own time- and space-dependent surface fluxes of heat and moisture specified by the user. Since the MLM runs many times faster than a regular RAMS run with several vertical levels, it was decided that a history write and restart would probably never be needed so the MLM variables have not been set up to be written to a history file. The MLM has no small timestep calculations and no need for special computation to minimize lateral boundary reflection. The only reason DELTAZ, DZRAT, and DZMAX are needed is for providing regular 3-dimensional RAMS model levels to be filled with MLM data and used for diagnosing cumulus convection.

3 Validation simulations

Following the construction phase of the two model versions developed for this project, a series of tests was conducted to verify that each version performed properly. These tests were most important in the case of the mixed-layer model since it was started from scratch from equations and other descriptions provided in the literature, and grafted into the RAMS code. The full model version, on the other hand, was constructed as a customized subset of RAMS which is a tested and established model. Nevertheless, verification tests were performed on the full model as well. These also served as benchmarks against which to compare the mixed-layer model solutions.

Basic simulations with the mixed-layer model were first performed to test every individual physical and computational process represented in the code. The processes specifically performed in the new mixed-layer model include the following.

1. Reading parameters set for the model in the namelist data
2. Constructing from the RAMS input sounding a base atmospheric state consistent with the underlying assumptions on the vertical structure of the atmosphere which form the basis of the mixed-layer model
3. Initializing all prognostic variables used in the mixed-layer model including a balanced boundary layer mean Ekman profile computed iteratively.
4. Computing advective tendencies for all prognostic variables
5. Computing the contribution to the mixed-layer horizontal pressure gradient force due to horizontal variations in the mixed-layer potential temperature, the inversion top potential temperature, the mixed-layer top height, and the geostrophic wind
6. Computing the Coriolis force tendency on the horizontal velocity components
7. Computing the contributions to the tendencies of mixed-layer momentum, moisture, and potential temperature due to surface fluxes of each
8. Computing the contributions to the tendencies of mixed-layer momentum, moisture, potential temperature, and depth due to entrainment fluxes at the top of the mixed layer
9. Computing horizontal diffusive tendencies for all prognostic variables

10. Accumulating all prognostic tendencies and advancing prognostic variables forward in time

11. Performing convective adjustment on prognostic variables any time the top of the mixed layer reaches a superadiabatic lapse rate (the parameterizations in the model prevent this from occurring in nearly any situation)

12. Diagnosing vertical velocity and other quantities from the prognostic variables and various model specifications

13. Computing appropriate values for the prognostic variables at the lateral boundaries

14. Filling up the full 3-D version of the model from prognostic variables and their assumed vertical structure in the mixed-layer model so that fields may be plotted and possible convection may be diagnosed

Each of these processes was carefully checked, using the VMS debugger and sometimes a hand calculator where helpful. Examples of the simpler tests performed are the following.

1. The model was run without surface fluxes of any type and without topography. Whether the model was initialized with wind or no wind, it was verified that the solution remained completely balanced and constant in time.

2. The model was run with no surface fluxes except for momentum. The input sounding contained a geostrophic wind. It was verified that the balanced mean Ekman wind in the mixed layer satisfied the equation for the mean Ekman wind for various surface drag coefficient values, and remained balanced and constant in time during a model integration.

3. The model was initialized with no wind. A surface heat flux was specified and the growth of the mixed layer was simulated. It was verified that the model-computed

entrainment fluxes at the top of the mixed layer obeyed the referenced equations used to design the model, and that the mixed layer growth rate and temperature increase were consistent with the surface heating rate.

4. The evolution of the mixed-layer moisture field was verified for consistency with the surface and top entrainment fluxes of moisture in a no-wind simulation.
5. The individual contributions in the hydrostatically-computed pressure field in the mixed layer were checked at individual grid points against the original equations for a model state containing a complicated thermal structure.
6. Both the entrainment and convective adjustments made to the prognostic variables were checked to verify that the adjustments were being made correctly.

Once these basic checks were completed, regular simulations of fairly standard processes were performed to see if the expected solution would develop. We report on two such simulations here. The first was a sea breeze circulation, set up as a result of the horizontal temperature contrast between a constant temperature water surface and a rapidly heating dry land surface on a summer day. Because such a circulation will tend to advance toward the land surface, it is customary in test simulations to initialize the model with a weak wind blowing from land to sea. This was done here using a 2 m/s wind blowing from the east, the land occupying the eastern half of the domain and the sea the western half. The computational domain used in both models spanned 200 km in the east-west direction and 100 km in the north-south direction with 5 km resolution in both directions.

The initial potential temperature field used in both models is shown in a vertical/east-west cross section through the center of the domain in Figure 3.1. It is weakly stable up to a height of 3 km and strongly stable above that. After a simulation period of 4 hours, the land surface has warmed considerably while the sea surface has not. This is illustrated in the potential temperature fields for both the full and mixed-layer versions of the model in figures 3.2a and 3.3a, respectively. The surface heat fluxes in the two models were not made equal, so the full model has undergone more land warming. The highly baroclinic region near x = 0 drives a solenoidal circulation illustrated in the u-component and w-component velocity fields in figures 3.2b and 3.2c for the full model and in figures 3.3b and 3.3c for the mixed-layer model. The circulation is considerably stronger in the full model because of the stronger land heating, but both models exhibit a similar structure in the horizontal wind field. Note that the mixed-layer model does not have an explicit return flow above the mixed-layer, so only the single layer wind is shown. The v-component (the north-south direction, into the page) wind fields for the two models are shown in figures 3.2d and 3.3d. The v-component has developed under the influence of the Coriolis force acting on the solenoidal circulation. The main difference between the two cases for this field is that the mixed-layer solution lacks the positive v-component region at the two-kilometer level just west of the domain center. This is another consequence of the absence of an explicit return flow above the mixed layer.

The second regular simulation reported here contained a solenoidal circulation driven by strong surface heating of sloping terrain. This simulation used a 150 km by 150 km horizontal domain in which the southwest fourth of the domain contained a mesa-like topographic formation having a horizontal top and straight sloping surfaces on its north and east sides. A 2.8 m/s southwesterly flow was specified as the initial sounding wind, and the vertical temperature profile was initialized as in the sea breeze experiments above. Figures 3.4a and 3.4b show a horizontal cross section of the mixed-layer horizontal winds two hours into the simulation. The u-component, which initially was 2.0 m/s throughout the domain has decreased everywhere, attaining a value of -2.0 m/s along the eastern side of the mesa. This indicates a well-developed upslope flow. The v-component shows a similar pattern on the north slope of the mesa. However it only achieves a minimum value near 0 m/s and actually increases above its initial 2.0 m/s value in the northern and eastern parts of the domain. The asymmetry between u and v is due to the Coriolis effect. The southwestern location of the higher terrain causes the mean upslope circulation to flow toward the southwest. The Coriolis force acting on this ageostrophic perturbation from the initial flow is toward the northwest. Hence, the Coriolis force acts to increase the v-component and decrease the u-component. The mesa rim, being the location where the horizontal Laplacian of the terrain height is negative, is a region of surface convergence and upward vertical motion. This can be seen in the w-component of motion shown in figure 3.4c. At the northeast corner of the mesa top, where the northern and eastern rims meet, the upward motion is enhanced. All these results are physically expected.

4 Testing of wind data assimilation

A primary goal of the software development phase of this project was to design and implement a technique for assimilating wind data obtained from single Doppler radar into the numerical prediction models. After consulting various references on the subject, we decided that a nudging method would be appropriate for both versions of the model. The nudging algorithm is implemented by adding a forcing term to both horizontal equations of motion. This term appears for each component in the form d/dt(VMOD) = (VOBS-VMOD)/SCLNUD where VOBS is the observed value of the component obtained from the Doppler radar, VMOD is the current model value of the component, and SCLNUD is a time scale determining the rate at which VMOD is to be forced toward VOBS. Typically, SCLNUD would be on the order of 1/2 hour, a time short enough for relaxation to take place in a fraction of the total simulation time and long enough so that the model is not completely forced to the observed wind but is allowed to retain some of its own history. We developed nudging algorithms for assimilating both cartesian wind components derived from the single Doppler analysis technique described by Easterbrook (1975) and radial winds obtained directly from the Doppler measurements. The tests of the first algorithm are described in this chapter, and the tests of the second in Chapter 5.

The primary intended application of the project under which these models were developed is forecasting the first occurrence of significant convection within a specified domain. The forecast is to be aided by horizontal radial wind measurements made by a single Doppler radar which is scanning the planetary boundary layer in the domain. The most common boundary layer wind feature which would accompany the early development of strong convection is horizontal convergence with vertical divergence. We therefore concentrated on testing the assimilation of wind data into the model for cases containing a region of horizontal convergence in the wind field. The most straightforward way of defining such a wind field was to specify a convergence line parallel to one of the coordinate axes (we chose a north-south orientation) through the center of the domain. Only the u-component of motion (that perpendicular to the convergence line) was assumed to be nonzero, and this was defined to be spatially constant on either side of the line while varying linearly across the line.

One such test performed with both versions of the model developed for this project is presented here. The models were initialized with a sounding representing a relatively stable atmosphere with no wind. The model domains were each 200 km in the east-west direction and 100 km in the north-south direction with a 5 km grid spacing in both directions. The convergence line in the assimilated data was set to a width of 10 km or two grid points, with 3 m/s westerly winds to its west and 3 m/s easterly winds to its east. The nudging relaxation time was set to 1800 s in both models.

Figures 4.1 and 4.2 show the model solutions for the full and mixed-layer versions of the model one hour into the simulation. Figures 4.1a and 4.2a present a vertical/east-west cross section through the middle of the domain of the u-component of motion. Both cases show a definite region of surface convergence centered at the x = 0 location, but the width of the region is far greater than the 10 km width of the assimilated data. Note that the full model depicted in figure 4.1 contains a compensating horizontal divergence aloft while the mixed-layer model, which has no explicit return flow, shows only the convergent mixed-layer winds. Figures 4.1b and 4.2b show the v-component which has developed as a result of the coriolis force acting on the u-component, which is ageostrophic because it was not present in the initial sounding. The vertical motion fields which are consistent with the horizontal convergence fields in the two models are shown in figures 4.1c and 4.2c.

The fact that the u-component has not developed a narrow convergence feature like the assimilated data, even though the simulation has progressed for two nudging relaxation time scale periods, implies that some other forcing term in the u-component equation of motion is comparable in magnitude to the nudging term. We found this to be the pressure gradient force term. The perturbation pressure field is shown in figure 4.1d for the full model. The pressure has risen a few millibars in the domain, most strongly at the surface. The pressure rise is the direct result of adiabatic cooling of the stable air as it is forced upward in response to the nudging of the horizontal wind toward convergence. The cooling is most prominent in the center of the domain where upward motion is strongest, as seen from a plot of the potential temperature fields in figures 4.1e and 4.2d. As a result, the surface pressure is highest at that location as well. The pressure gradient force is thus directed away from the domain center on both sides which opposes the nudging force. Hence, the sharp definition of the convergence line in the assimilated data is prevented from developing.

Four hours into the simulation, the difference between the model winds and the assimilated winds is even larger. Figures 4.3 and 4.4 show the full model and mixed-layer model results, respectively, for this later time. The u-component fields of figures 4.3a and 4.4a show an even broader zone of convergence, with the u-component varying by less than 5 m/s over a 200 km distance. This is quite different from the 6 m/s change over a 10 km distance present in the assimilated u-component field. The full model perturbation pressure field plotted in figure 4.3c shows the horizontal pressure gradient force at the surface to be stronger than before. The vertical velocity fields for both models plotted in figures 4.3b and

4.4b show the region of upward motion to have expanded significantly in the x-direction. The strongest upward motion still remains in the center, however. A corresponding major lateral expansion of the cold dome in both models is likewise apparent from the potential temperature fields in figures 4.3d and 4.4c.

The problem worsens when the simulation is carried out further with the nudging turned off. Because the intended application of these models is to make a forecast, normal use of them should involve assimilating wind data for a period of time and then continuing the simulation in pure forecast mode without continuing the data assimilation. This was done for the present test cases by turning off the nudging immediately after the four hour time, and continuing the simulations for another hour. Figures 4.5a and 4.6a show the full model and mixed-layer model u-component fields after the additional hour. Instead of surface convergence, a significant region of divergence has formed in the middle of the domain. The corresponding vertical velocity fields shown in figures 4.5b and 4.6b show subsidence to pervade the middle third of the domain. The reason for this is that the cold dome built up under the influence of the nudging force is now in the process of collapsing. A comparison of the full model theta field shown for this time in figure 4.5c with the earlier one in figure 4.3d shows the central cold peak to have disappeared. That the surface winds are divergent rather than convergent at this time shows that the nudging of the model to the observed wind fields has proved a detriment rather than an improvement to the solution.

In summary, the models have failed to respond to the nudging force in such a way that a new balance of the model fields is achieved and the model velocity field agrees closely with the assimilated data. This failure is a consequence of the assimilated data containing wind data inconsistent with the models' temperature fields or mass fields. In a stable atmosphere, as used for these tests, the temperature and velocity fields are intimately coupled so that a change in one induces a change in the other. In turn, the induced change in the second induces a counter change in the first, opposing the original change to the first.

If, on the other hand, a nearly neutral atmosphere is used to initialize the models, the temperature field is loosely coupled to the velocity field so that any changes induced in the velocity field do not produce changes in the mass field which fight the velocity changes. We performed simulations with both models which demonstrate this point. These simulations are identical to the stable ones described above, except that they were initialized with nearly neutral lapse rates up to a height of 3 km. Figures 4.7 and 4.8 show the u-component fields after 4 hours of simulation (and nudging) time. In this case, both models have been able to develop and maintain fairly strong convergence lines, although they are still not as sharp as in the assimilated data. As before, the nudging is turned off at the four hour time and the simulation continued for one additional hour. The full model u-component field (figure 4.9) still maintains surface convergence, although it has weakened. The mixed layer model u-component field (figure 4.10) however is exhibiting some surface divergence. This is a consequence of the model's lack of an explicit return flow above the mixed-layer convergence field. The mixed-layer model makes more approximations than the full model and hence introduces more adjustable parameters. Appropriate tuning of these parameters is required for the model response to more closely follow the behavior of the full model. In this case, using a larger value of the horizontal diffusion coefficient for the boundary layer height would have prevented it from growing so rapidly in the presence of the sustained vertical motion in the center of the domain. Because the model implicitly requires the mixed layer to be capped by a stable layer, the higher diffusion would allow the upward motion to continue without a continued elevating of the mixed layer top and a consequent building of a cold dome.

The main finding of these generic data assimilation tests is that as long as the temperature and velocity fields are coupled due to atmospheric stability, it is not sufficient to assimilate only velocity data into a numerical prediction model; appropriate temperature data are also required. Although a negative result, it is an important one in view of the fact that there are widespread plans to assimilate the velocity fields derived from the upcoming national network of NEXRAD radars and wind profilers into operational forecast models without temperature information of the same detail and coverage. This fact and the negative results we obtained in the nudging tests for this study prompted us to submit a paper to the Radar Conference which is to be held in March 1989. In the paper, we describe a physical scenario in which a single Doppler radar might detect a convergence line in the wind field but not be able to ascertain the thermal structure of the line. A simulation to demonstrate the points made above was performed using the nonhydrostatic version of RAMS which executes more slowly than the models described here but provides full detail and directly interpretable results. The paper is included as Appendix B of this report. We conclude that to effectively assimilate into a numerical simulation observed wind data which implies vertical motion, it is necessary to simultaneously assimilate temperature data which is consistent with that vertical motion field.

5 Testing of radial nudging algorithm

We developed and tested for this project a new algorithm for assimilating single Doppler wind data based on a concept proposed by J. Goerss, formerly of the Cooperative Institute for Mesoscale Meteorological Studies, and R. Doviak and R. Rabin of the National Severe Storms Laboratory in Norman, Oklahoma. Their concept was to directly input to the model the observed single Doppler radial wind component, rather than first processing the observed radial wind through another technique (e.g., Easterbrook, 1975) to extract the two horizontal cartesian wind components.

Obviously, any technique for computing the total horizontal wind field from a radial component only is adding information on the flow. Some of this information is accurate because it is derived from constraints imposed on the flow by the basic laws of fluid mechanics such as mass continuity. However, these laws are not sufficient to close the set of equations used in obtaining the cartesian components, and additional arbitrary assumptions are required. As a consequence, significant uncertainty exists in the final product. By eliminating this step in the transfer of Doppler information to the model and directly inputing the radial component, the introduction of extraneous information to the winds is also eliminated.

Because the model employs the equations of fluid dynamics, it is hypothesized that it will place appropriate physical constraints on the assimilated radial winds and effectively extract from them both cartesian components. This technique has a chance of being superior to the standard method above in that the missing information needed in obtaining the full horizontal wind field from the radial component is in effect supplied by the model wind itself, and is thus not arbitrary but is instead related to the physical situation being observed.

We designed a numerical algorithm which nudges the model winds directly to the input radial component. The method consists of the following steps.

1. At each grid point in the model domain, the current model cartesian components are decomposed into a radial and azimuthal component based on a polar coordinate system centered at the location of the Doppler radar.
2. The difference between the observed radial wind and the model radial wind is computed, and the model radial wind is nudged toward the observed radial wind with a strength proportional to that difference. The model azimuthal component is not altered.
3. After the forcing of the model radial component, the radial and azimuthal components are transformed back into the cartesian components.

We tested this radial nudging algorithm for several wind fields in which both cartesian components were specified according to some idealized flow pattern. The radial wind component which a Doppler radar would measure from each of these fields was computed and used as the observed wind for assimilation into the model. The model winds were then examined throughout their evolution to determine how closely the radial nudging algorithm forced them to the initial cartesian wind components.

The first tests we conducted of this algorithm involved wind fields containing horizontal convergence somewhere in the domain. These produced quite unacceptable results and led us to suspect that the method was deficient and would not work. We later discovered that even straightforward cartesian nudging of both wind components will fail when it tries to produce significant vertical motion in stable air and thermodynamic data which would conform to this vertical motion is not available for simultaneous assimilation (see Section 4 and Appendix B of this report). We thus re-tested the radial nudging algorithm on a horizontal wind field containing translation, rotation, and deformation, but no divergence. Moreover, we input a stable atmosphere for the test to effectively constrain the horizontal wind field to remain nondivergent. This constraint increases the probability of success of the algorithm for this case because the correct solution is itself nondivergent. The radial wind component is divergent, even though the cartesian field from which it is obtained is not, and nudging to the radial component tries to force the model winds to become divergent. The large atmospheric stability specified for this case prevents the vertical motion and hence the horizontal divergence from ever becoming large for a sustained period of time.

The radial nudging test simulation was run using the mixed-layer version of RAMS on a physical domain spanning 200 km in the x-direction and 100 km in the y-direction with 5 km resolution in both directions. The assumed location of the Doppler radar is very near the center of the domain. The prescribed nondivergent wind field whose radial component will be assimilated into the model consists of a uniform flow from the south of 3 m/s (v = 3 m/s) over the eastern two-thirds of the domain and a uniform flow from the north of 3 m/s (v = -3 m/s) over the western one-third of the domain. The u-component of motion is zero throughout the prescribed wind field. The two constant v regions are separated by a 10-km-wide shear line over which the wind varies linearly. The entire shear line contains vorticity and deformation, but no mean translation and no divergence. The regions on either side of the shear line contain pure translation only. Nudging of the model to the radial wind component of this field was performed over a four-hour simulation period using a nudging relaxation time scale of 1800 s. Nudging was then ceased and the simulation carried out for an additional two hours to examine any flow evolution which might occur in the absence of the forcing.

Figures 5.1a-c show the u, v, and w components of motion 1 hour after the simulation (and nudging) startup time. Any nonzero value for the u-component is of course a deviation from the actual cartesian wind field from which the assimilated radial component is computed. It arises, however, as a consequence of the radial nudging algorithm which has the requirement that nudging will not directly force the azimuthal component. As long as the v-component is to be directly forced by the nudging at a location not due north or south of the radar, the u-component must be forced simultaneously to satisfy that requirement. Note that the u-component northwest of the radar location (which is near x=0,y=0) is negative implying flow toward the west. The v-component is positive in the same location so that the resultant flow there is radially outward from the radar. This is in direct accordance with the outward radial motion that the radar would see in the total cartesian wind field specified for this experiment.

A similar discussion applies to the other regions of the flow in figures 5.1a and 5.1b. This time in the simulation is rather early for horizontal pressure gradient forces to have exerted a significant influence on the horizontal velocity field, so the latter has thus far responded primarily to the nudging forces only. The horizontal flow does however contain substantial rates of divergence and convergence as deducible from figure 5.1c. Vertical velocities have exceeded 2 cm/s in magnitude at a height of 400 m by this time. The location of strongest convergence can be seen to be due south of the radar. This is producing surface high pressure due to the stability of the air and its ascent above the convergence which will counteract the positive u-component to its west (figure 5.1a). Similarly, a surface low pressure is forming due north of the radar because of the subsidence warming above that location, the the negative u-component seen to its west in figure 5.1a will be counteracted as a result. Farther west of these locations, just west of the shear line at x = -40 km, the north-south pattern of upward and downward motion is reversed, as is the pattern of the positive and negative u-component motion, so there the developing horizontal pressure gradient forces will again tend to force the u-component in the direction of zero. The v-component in figure 5.1b is showing a clear development of the shear zone northwest and southwest of the radar where it is directly detected in the radial wind component, but not west of the radar where the radial component contains no information on the zone at all. However, the north-south component of the pressure gradient force which is developing on each side of the shear zone (in the opposite sense on each side) will strengthen the shear west of the radar in its forcing of the v-component. This demonstrates how the constraint imposed on the flow by the large static stability which was specified for this case is helping to force the model flow to the true solution.

Figures 5.2a-c show the u, v, and w components of motion in the model at four hours after the startup time of the simulation. Following the initial transient induced by the nudging early in the simulation, the vertical velocity field has damped to weaker values, not exceeding 0.5 cm/s in most of the domain. All three components have become fairly steady, not having changed much from the 3-hour simulation time (not shown). Thus, the model has approached what will be its final solution. The u-component in this solution has a systematic tendency toward eastward motion in the north half of the domain and westward motion in the south half giving a negative mean vorticity (for that component) which is opposite to the sense of the specified shear zone vorticity. The v-component, on the other hand, exhibits a mean positive vorticity over the domain, the same sense as that specified in the shear zone. Compared with figure 5.1b, figure 5.2b shows the shear zone to be continuous from north to south without a break west of the radar. The filling in of the middle region was caused by the pressure gradient forces as discussed above. The v-component overall resembles the true solution fairly well, although the east and west extremes of the domain both contain erroneously weak wind magnitudes.

Figures 5.3a-c show the u, v, and w components of motion at the six-hour time in the simulation, which is following two hours without nudging. The u-component continues to exhibit a negative contribution to the mean vorticity in the domain while the v-component continues to do the opposite. The v-component has retained a well-defined shear zone without radial wind data assimilation, although the zone is more diffuse across its width and the shear line has begun to take on a south-southwest to north-northeast orientation in response to advection by the u-component. The w-component has undergone the largest relative change in the two-hour period, but magnitudes remain small, averaging around 2 or 3 mm/s in absolute value. The horizontal components have changed only slightly during the two hours since the fields shown in figures 5.2a-b indicating that by the four-hour time, the nudging force was no longer strong (i.e., that the model radial wind field had become close to the observed radial wind). Thus, the model attained a nearly steady state solution different from the specified true solution.

We give the radial nudging simulation a fair rating for this case, but we reiterate that the physical scenario was deliberately chosen to increase the likelihood of success. We have seen that the technique does not perform as well in the general case, primarily because of the problems encountered when nudging attempts to force vertical motion in a stable atmosphere. That is a separate problem which is encountered in the assimilation of both cartesian wind components as well. We are still of the opinion that some of the reasoning behind the radial nudging technique is sound. In particular, the introduction of erroneous information to the wind field which occurs in standard single Doppler analysis techniques is an ongoing problem to which a solution should be found. We have shown that direct assimilation of the observed radial component, which bypasses the Doppler analysis step, is not a viable alternative. During this experimentation, we have identified a new method which has the potential of solving both problems. Both techniques discussed above (prior recovery of cartesian components before assimilation and direct radial wind assimilation) involve only a one-way communication of information; Doppler data is input to the model but model information is not fed back to the Doppler data external to the model. A possible new method would be to use the current model winds as input to a standard single Doppler analysis technique in place of making any arbitrary assumptions on the wind field. We plan to test this idea in future research. A solution still needs to be found to the more serious problem that assimilation of wind data without thermodynamic information is generally unsuccessful.

6 Simulations of actual atmospheric cases

Although it was entirely expected that the results shown by the "generic" nudging simulations described in chapter 4 of this report would be applicable to a simulations run with actual observations, the two versions of the model were run for three case studies from the CINDE field program. The following section will describe the radar analysis technique and the results of those simulations.

A. Methodology for Analysis of Doppler Radar Data for Model Input

For the real data case studies, the single Doppler radial velocity data from NCAR's 5-cm CP-3 radar during 1987 CINDE experiment was used. Three separate days were considered, 17 July, 27 June, and 31 July. For the first case, four elevations (0.4, 0.9, 1.7 and 2.6 deg) were used, while only the 0.4 deg elevation was used in the latter two cases. Editing consisted of thresholding out low signal-to-noise returns and those velocities with excessive spectral width, unfolding velocities, removing ground clutter and second trip echoes, and applying a liberal spatial filter to the data. All this was done in 'radar space' using NCAR's RDSS software.

The edited radial velocity data were then interpolated to a cartesian grid using NCAR's REORDER interpolation software. Since CP-3's western view was severely limited by the Front Range at about 30 km to the west, the 100 by 100 km grid was configured off-center from the radar in the E-W direction, from 30 km to the west, to 70 km to the east (about the limiting range of boundary-layer detectability). The grid extended 50 km from the radar in both the north and south directions. The horizontal grid spacing of the Doppler data grid was 2.5 km to account for the numerical model grid stagger. The winds were interpolated to vertical grid levels at 0.5, 1.0, 1.5 and 2.0 km above the radar elevation. The radar sampling capabilities and interpolation method yielded quite detailed and significant radial velocity gradients in the horizontal, with vertical shear much less resolved. (Since only one elevation was used in the latter two cases, the radial wind fields were identical at all levels.) These gridded radial velocities were filtered further, and echo-free patches in the domain were filled by horizontal interpolation and extrapolation to the domain bounds.

From the radial velocity field, a divergence field could be diagnosed by the method of Koscielny et al. (1982). However, the models were not designed to be nudged to accordance to the observed radial wind and/or divergence fields, but instead required the Cartesian wind component fields. While we developed and initially tested a method for deriving the tangential wind field as a residual of the radial wind and divergence fields (which would have provided the u and v wind fields), it could not be applied to these cases because of the off-centered position of the radar in the 100 by 100 km computational domain. Thus, for simplification, the tangential wind field was derived from the NCAR PAM mesonet, which had a station spacing of about 10 km. While the radial wind field varied with height (for the first case only), the tangential wind field was constant with height. We did not explore methods by which the tangential wind could have varied with height according to Eckman turning. From these radar-derived radial winds and PAM-derived tangential winds, the u and v components were obtained for input to the model.

Figures 6.1a-f illustrate the processing methodology. The PAM observations for the first case at 1500 local time (LT) are shown in Figure 6.1a, along with the 100 by 100 km computational domain and the off-centered CP-3 radar position. The dominant feature is the north-south convergence line about 30 km east of the radar, denoted by dashed line A-B. Figure 6.1b shows the PAM wind-field as objectively analyzed onto the full grid-point domain, and the corresponding PAM-derived divergence field shows the strong convergence line. Figure 6.1c shows the radar-derived radial wind field (for the lowest vertical level), and Figure 6.1d shows the contoured tangential component of the PAM wind field. These radial and tangential components are combined to yield the final wind-vector field in Figure 6.1e, which represents the input for the model. The corresponding divergence field in that figure is seen to retain the basic north-south convergence line in the proper location, but with some significant fine-scale differences from the PAM-derived divergence field in Figure 6.1b.

The divergence field computed from the radar-derived radial winds alone, using the method of Koscielny et al. (1982), is shown in Figure 6.1f. Overlapping sectors for this derivation were centered on every other grid point in both directions, with each Cartesian "sector" consisting of 9 by 9 grid points representing a 22.5 by 22.5 km area. This single-doppler derived divergence field shows general agreement with those obtained from the PAM winds (Figure 6.1b) and the combined radar-radial and PAM-tangential winds (Figure 6.1e), but with less detail and with lesser extremes, as expected. In particular, the full north-south extent of the convergence line is diagnosed. The largest differences are in the southeast portion of the domain, where the PAM observations are sparse and the Cartesian "sectors" are significantly smaller than recommended by Koscielny et al. (1982).

B. Case Study Simulations

The simulations using the analyzed Doppler winds were initialized with special soundings taken as part of the CINDE program. These soundings were of very high resolution in the vertical (about every 40-50 m). At several levels, especially in the boundary layer, the winds were of questionable reliability. Therefore, a 9 point vertical running average was used to filter the winds before the models were initialized. The model fields were interpolated from these soundings to obtain a horizontally homogeneous initial state for the simulations.

Starting at the start of the simulation, the low level model winds were nudged toward the Doppler winds for one hour with a nudging timescale of one-half hour. After one hour, the nudging was turned off to simulate an actual forecast where there would be no information available on the wind field. The model was then run from one to two hours.

The first case was the afternoon of 17 July 1987. A north to south low level convergence line was observed to develop at about noon and remained relatively stationary until convection developed several hours later. This line can be seen in the PAM and radar observations as illustrated in Figure 6.1. The model was nudged to the u and v wind components of 1315 LT and initialized with the 1430 LT Denver sounding. The vertical motion field from the full model version at 1 hour of simulation time at a level about 1 km above the topography is shown in Figure 6.2a. The solid contours are upward vertical motion and the dashed contours are downward vertical motion. A region of upward motion, showing the convergence line, is seen just east of the center of the domain. Consistent with the generic nudging simulations, the line is evident in the nudged model fields but not quite as well defined. Comparing the full model field with the same field from the mixed layer model (Figure 6.2b) shows that the main upward motion areas are similarly located and about the same magnitude although there are many differences in the fields.

After the nudging had been discontinued for 1/2 hour (at 1.5 hours into the simulation), the vertical motion fields again look consistent with the expectations based on the generic nudging experiments. The upward motion is replaced by subsidence as the "cold dome" forced by the thermally imbalanced upward motion collapsed. Figures 6.3a and 6.3b show very similar behaviors for the full model and the mixed layer model, respectively. The areas which were previously rising are now subsident with new areas of rising motion forced on the edges of this numerical cold pool. By the end of the simulation (Figures 6.4a and 6.4b), both models again look similar as the fields settle down after the shock from the imbalanced forcing.

The second case was 27 June 1987. The model was initialized with the 1300 LT Denver sounding and nudged toward the radar/PAM observations at 1500 LT. In this case, convection to the north of the domain produced a strong outflow boundary which entered the domain, producing an east to west convergence line, as shown by the PAM observations in Figure 6.5a. Figure 6.5b shows contours of the east-west wind component and velocity vectors at 1 km above the ground at 1 hour of simulation time from the full model version. The corresponding vertical motion field is shown in Figure 6.6a where a region of upward motion is evident at the convergence line. As in the first case, the mixed layer version was very similar (Figure 6.6b). After the nudging has been turned off (Figures 6.7 and 6.8), again similar to the first case, the upward motion decreases by 1.5 hours and becomes subsident by 2 hours.

The third case was 31 July 1987 and was substantially more complicated than the first two. On this day, an outflow boundary from convection in the foothills entered the domain and collided with the pseudo-Denver convergence line and other gust fronts that were already in the domain (Figure 6.9a). Although it is more difficult to see than the first two cases, the models behaved similarly. The vertical motion fields from the mixed layer model from 1, 1.5, and 2 hours are shown in Figure 6.9b-d.

To summarize these real data cases, the behavior of the models in these cases is similar to the nudging experiments to generic flow fields. The thermally unbalanced flow forces vertical motions and pressure fields which attempt to oppose the flow. As soon as the nudging force is discontinued, as would have to be done for a real time forecast, the flow quickly responds to the pressure fields and becomes very different from the observed circulation.

7 Summary and suggestions for future research

We have shown in preceding sections that in general the assimilation of just wind data into a dynamic model is not feasible since the model will quickly adjust the mass field in such a way that the imposed divergence is destroyed by perturbation pressure fields that oppose the derived divergence fields. The situation is no better if we had a system of measuring simply the mass fields on the mesoscale as the model will develop divergence fields that oppose the input mass fields. What is clearly needed is a technique for observing both the wind field and the mass field with resolution such as obtained with a single Doppler radar. Unfortunately this is not possible. It would be interesting to investigate using a mix of single Doppler radar data and satellite retrieval of the mass fields. Current satellites can retrieve soundings with a horizontal resolution of approximately 15km. Vertical resolution, however, is quite crude. It is possible to use radar data to enhance the vertical resolution of the sounding data. The radar radial velocity data, for example, can define the top of a cold pool by the vertical divergence at its top. By assigning the depth of the cold pool the satellite retrieval algorithms can be modified to infer the average temperature of the cold pool. Likewise the horizontal boundary of the cold pool can be inferred from the single Doppler radar data yielding a more precise definition of the boundary between the cold and undisturbed air mass. We believe that this is a natural next step beyond the research that we have accomplished so far. Other possibilities of obtaining mass and wind fields using a combination of remote sensing systems may also exist but they can only be evaluated by using a flexible, modeling system such as RAMS. Also at this point it is pre-mature to restrict four dimensional data assimilation of multiple data systems to mini computers. Once a satisfactory technique of assimilating a mix of data sources in a mesoscale model is developed using what ever computer resources are available, then the technique can be scaled down and optimized on a mini computer system. We clearly have not reached that level of maturity of data assimilation in meso-beta-scale models.

Other aspects of this project also point to the need for a more powerful computer than a machine rated at 1 MIPS. The domain size of 100 km by 100 km is far too small for a 6 to 8 hour forecast. If an average advective speed of 10 m/s is assumed, the interior of the domain will feel the effects of the boundaries within an hour and a half. The forecast period is thus limited by this time scale. Fortunately, computers have been steadily advancing from a price/performance aspect, so now a machine with the performance about 20-40 times that of a MicroVAX II can be purchased for about 4 times the cost. With a machine of this speed, real-time forecast applications of the full model version can be realized. For example, a coarse grid of about 40 km resolution may cover an area the size of a state with a nested grid of 5-10 km resolution covering a local area of interest. The effects of the model initialization may then be removed far enough from the region of interest to allow for a longer forecast.

The utility of the model versions developed as part of this project are not limited to this nudging application. Rather, they can be used for many other applications where their particular features are desired.

References

Anthes, R.A., D. Keyser, and J.W. Deardorff, 1982: Further considerations on modelling the sea breeze with a mixed-layer model. *Mon. Wea. Rev.*, 110, 757–765.

Easterbrook, C.C., 1975: Estimating horizontal wind fields by two-dimensional curve fitting of single doppler radar measurements. *Preprints, 16th Radar Meteorology Conference*, Houston TX, Amer. Meteor. Soc., 214–219.

Keyser, D., and R.A. Anthes, 1977: The applicability of a mixed-layer model of the planetary boundary layer to real-data forecasting. *Mon. Wea. Rev.*, 105, 1351–1371.

Koscielny, A.J., R J. Doviak and R. Rabin, 1982: Statistical considerations in the estimation of divergence from single-doppler radar and application to prestorm boundary-layer observations. *J. Appl. Meteor.*, 21, 197–210.

Lavoie, R.L., 1972: A mesoscale numerical model of lake-effect storms. *J. Atmos. Sci.*, 29, 1025–1040.

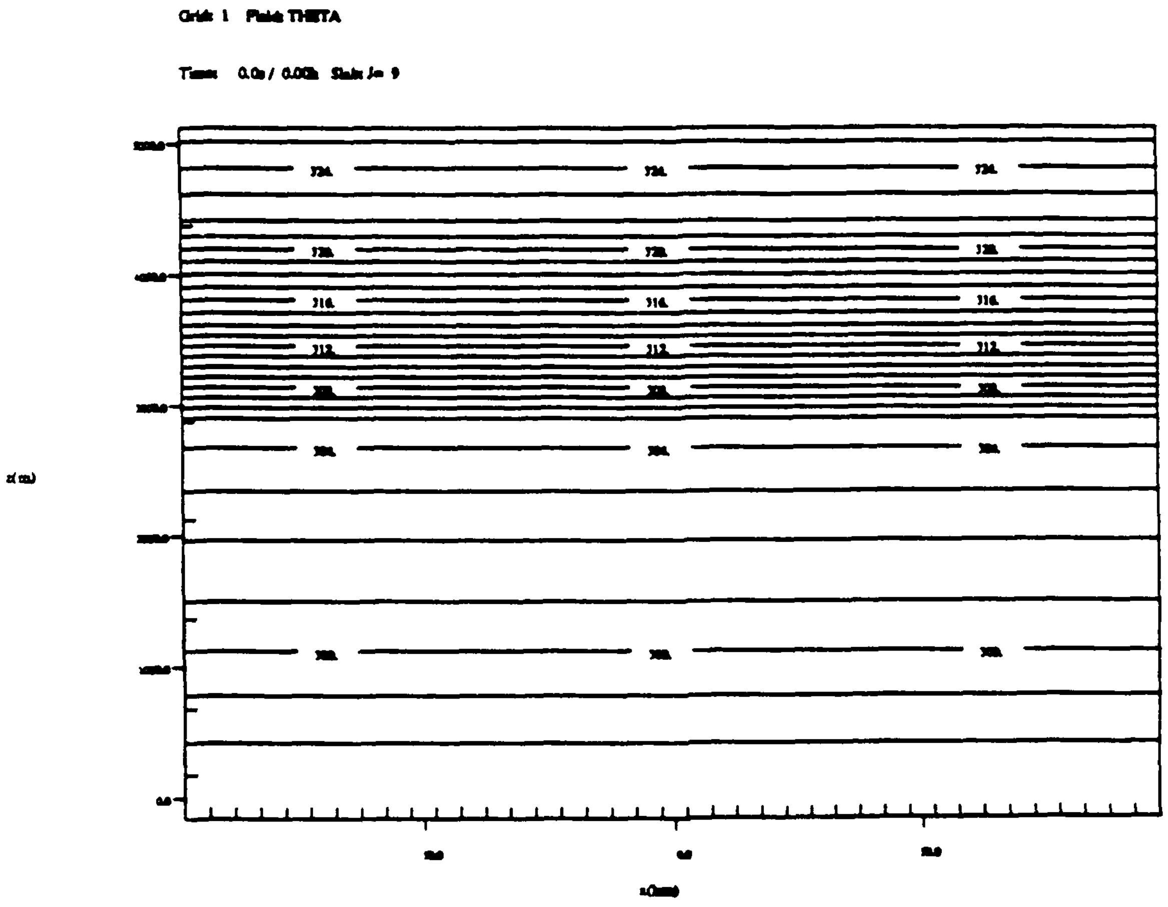

Figure 3.1. Vertical cross section of the potential temperature field used to initialize the sea breeze test simulation.

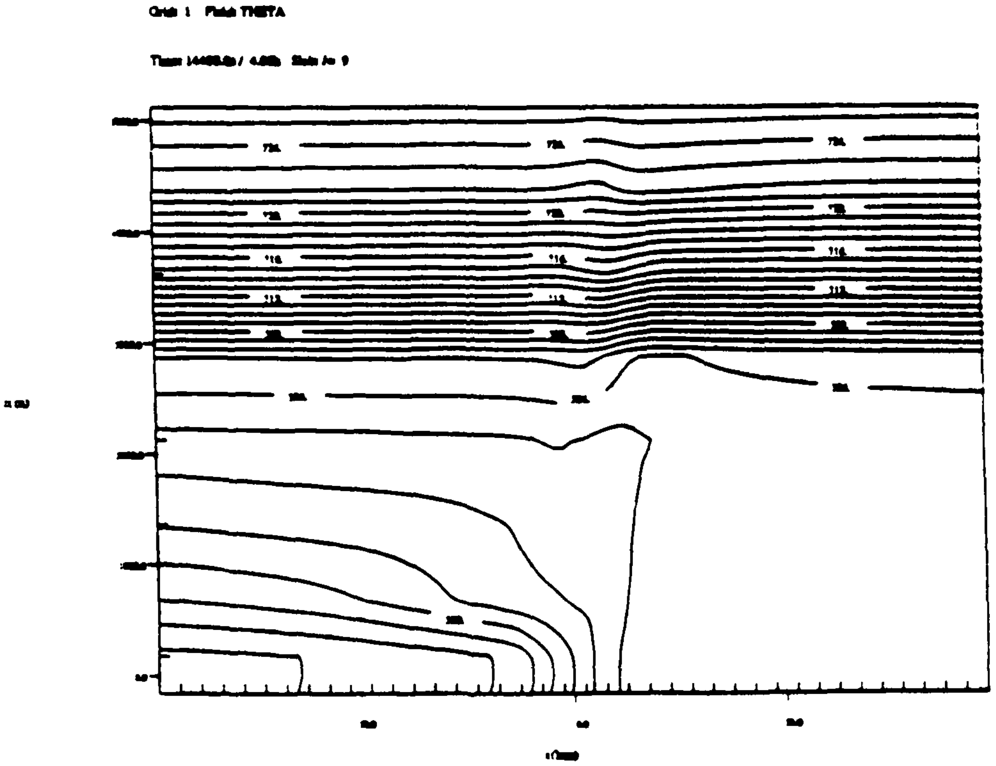

Figure 3.2a Vertical cross section of the potential temperature field in the full model version of the sea breeze test simulation 4 hours into the simulation.

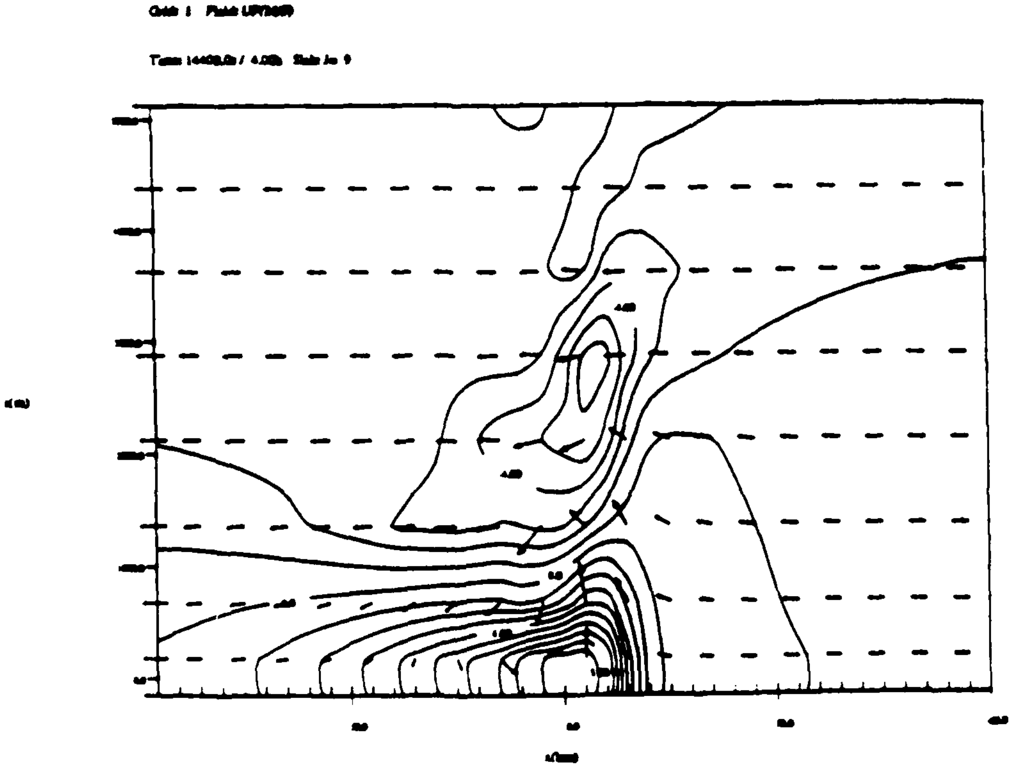

Figure 3.2b Vertical cross section of the u-component of motion in the full model version of the sea breeze test simulation 4 hours into the simulation.

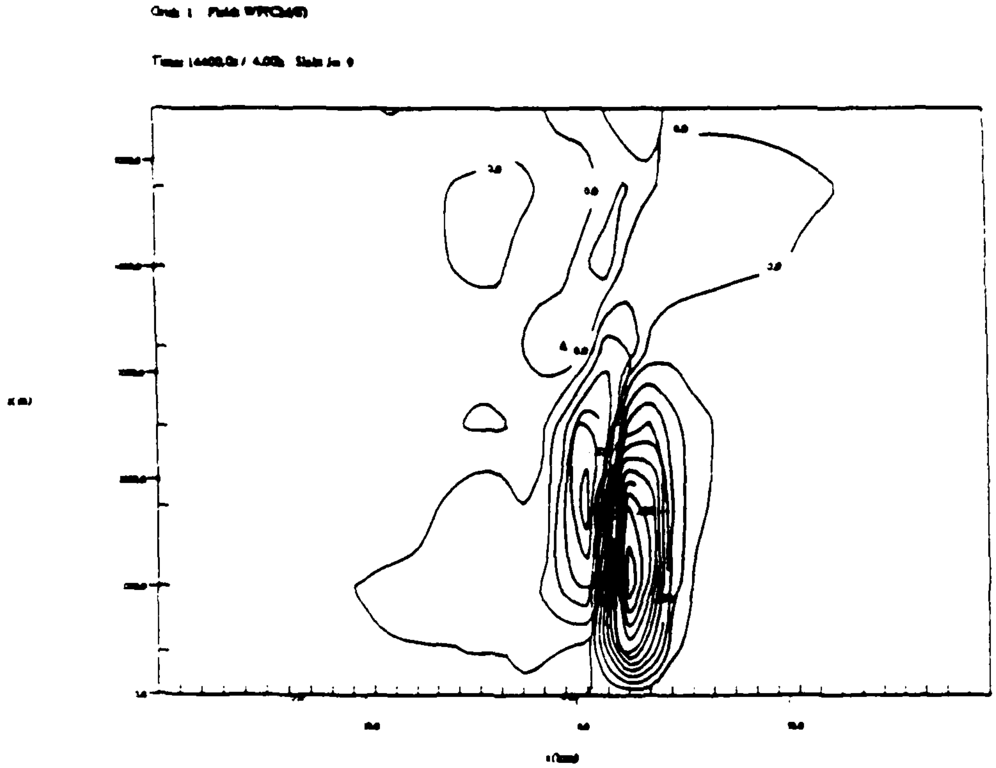

Figure 3.2c Vertical cross section of the vertical motion field in the full model version of the sea breeze test simulation 4 hours into the simulation.

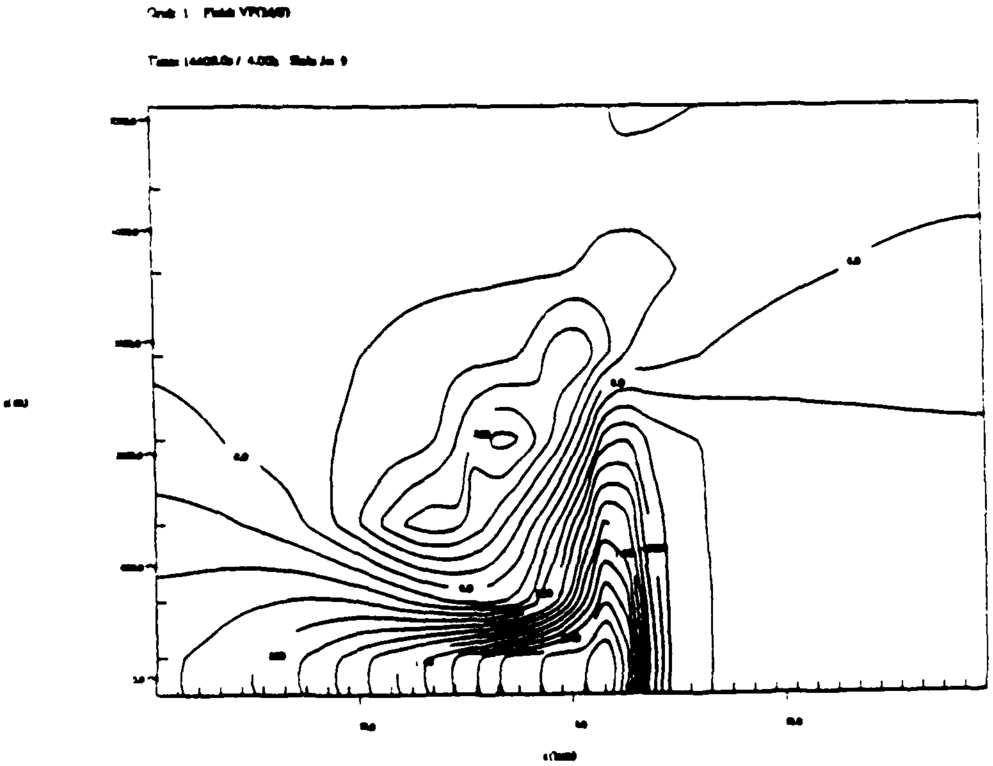

Figure 3.2d Vertical cross section of the v-component of motion in the full model version of the sea breeze test simulation 4 hours into the simulation.

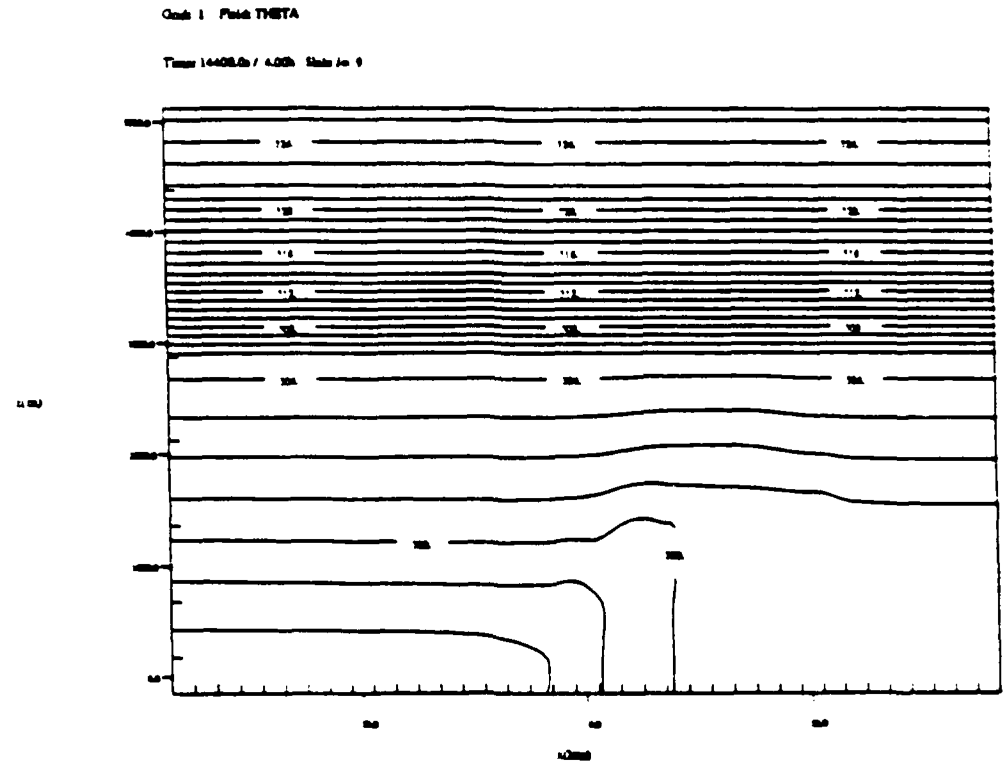

Figure 3.3a Vertical cross section of the potential temperature field in the mixed-layer model version of the sea breeze test simulation 4 hours into the simulation.

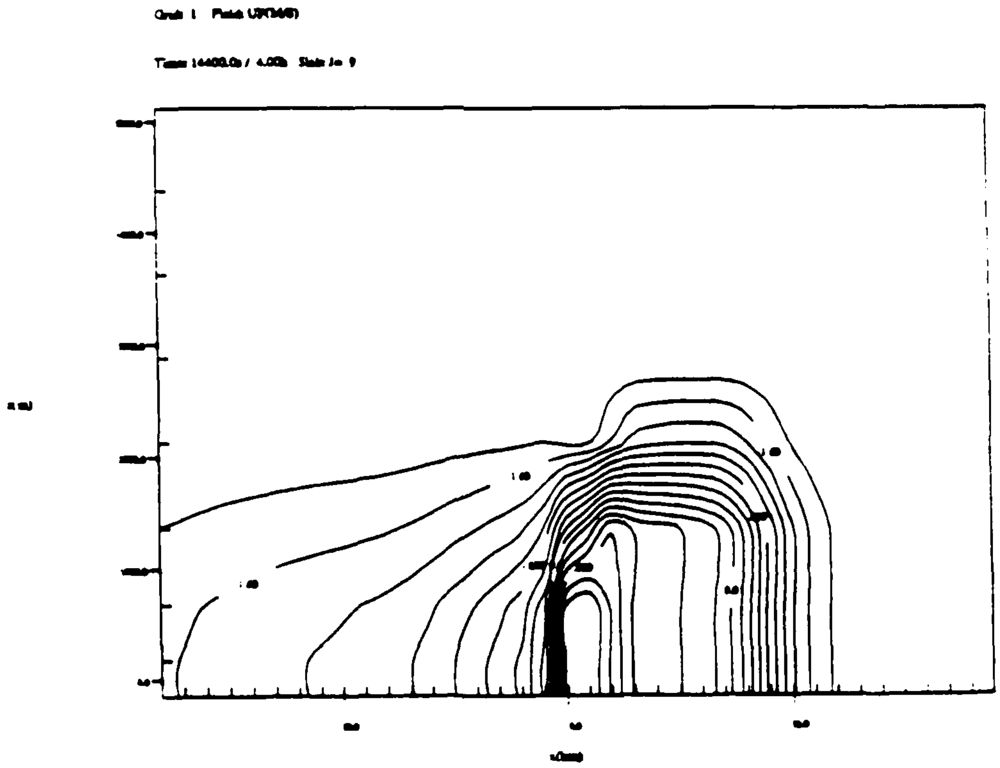

Figure 3.3b Vertical cross section of the u-component of motion in the mixed-layer model version of the sea breeze test simulation 4 hours into the simulation.

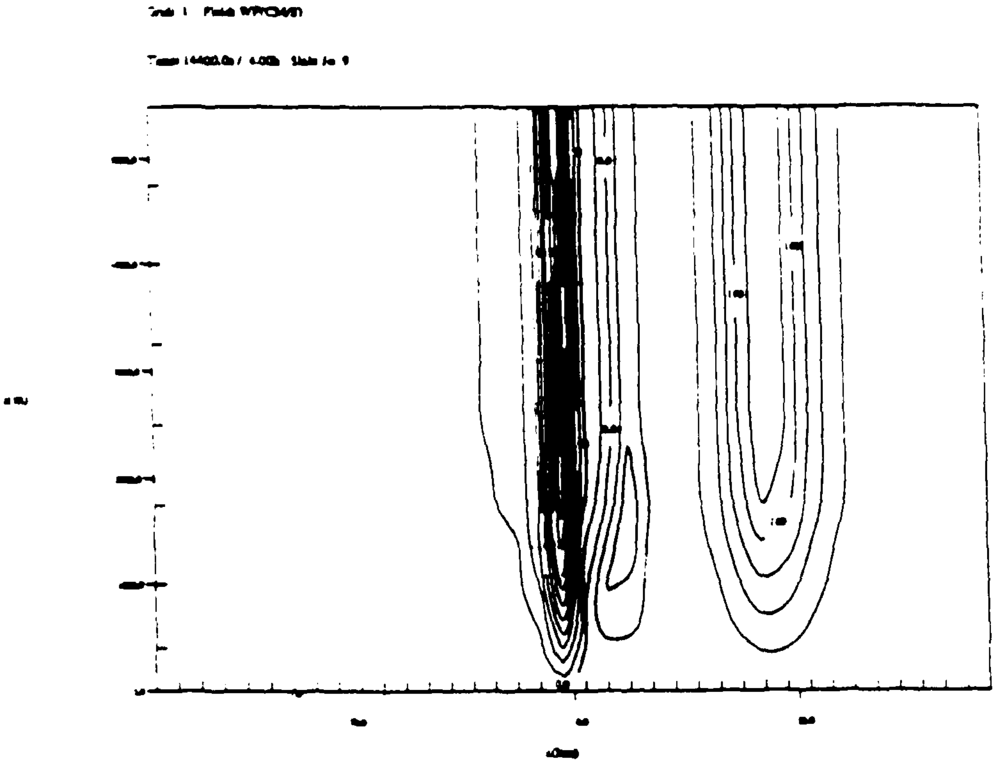

Figure 3.3c Vertical cross section of the vertical motion field in the mixed-layer model version of the sea breeze test simulation 4 hours into the simulation.

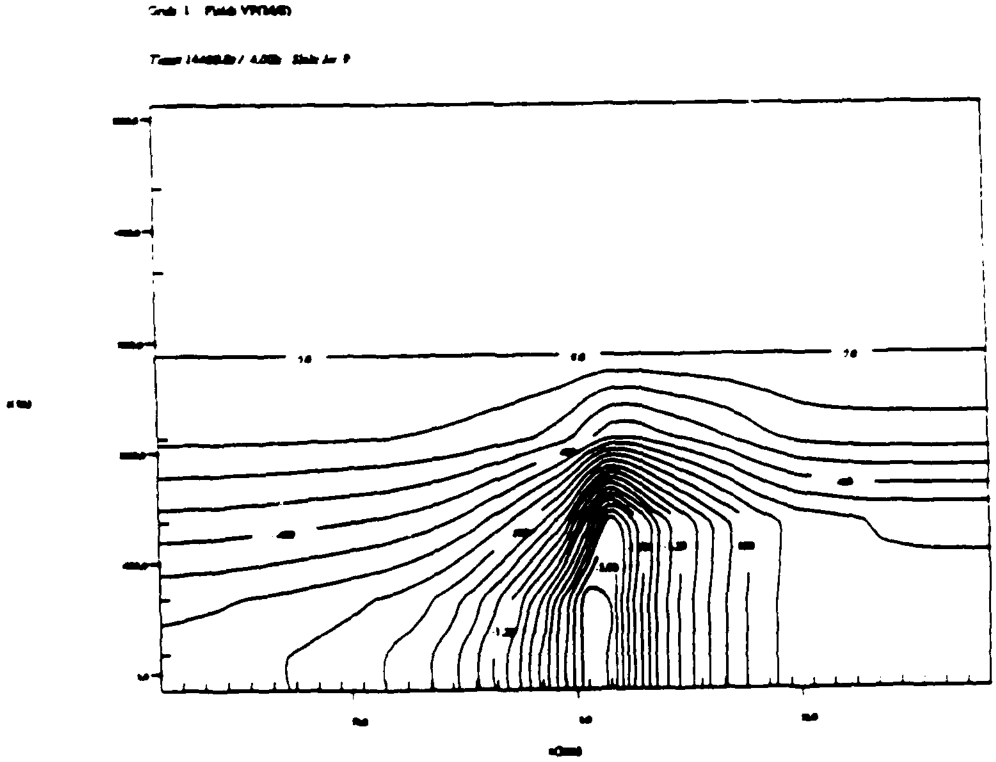

Figure 3.3d Vertical cross section of the v-component of motion in the mixed-layer model version of the sea breeze test simulation 4 hours into the simulation.

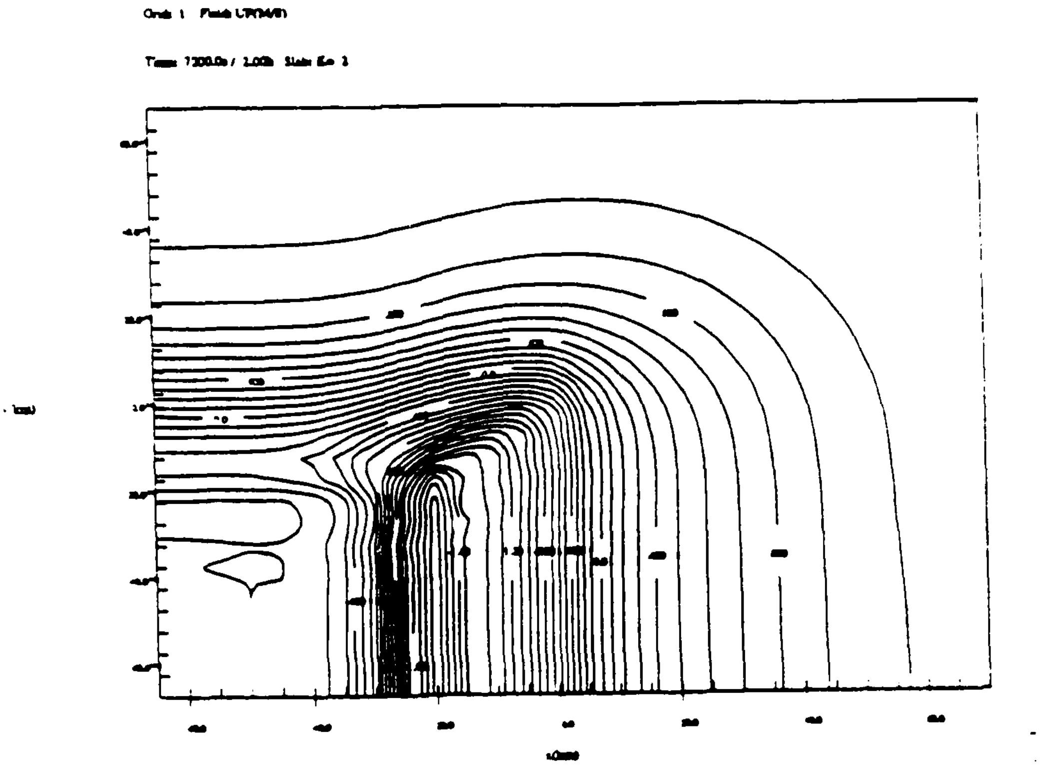

Figure 3.4a Horizontal cross section of the u-component of motion in the mixed-layer model version of the heated sloping terrain test simulation 2 hours into the simulation.

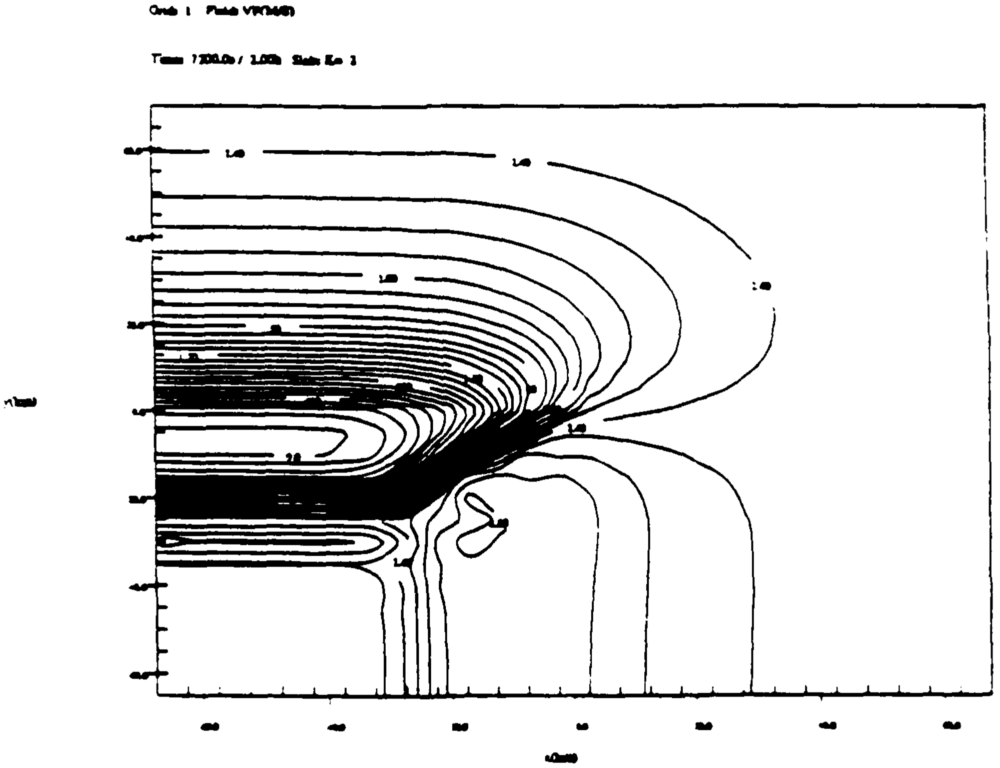

Figure 3.4b Horizontal cross section of the v-component of motion in the mixed-layer model version of the heated sloping terrain test simulation 2 hours into the simulation.

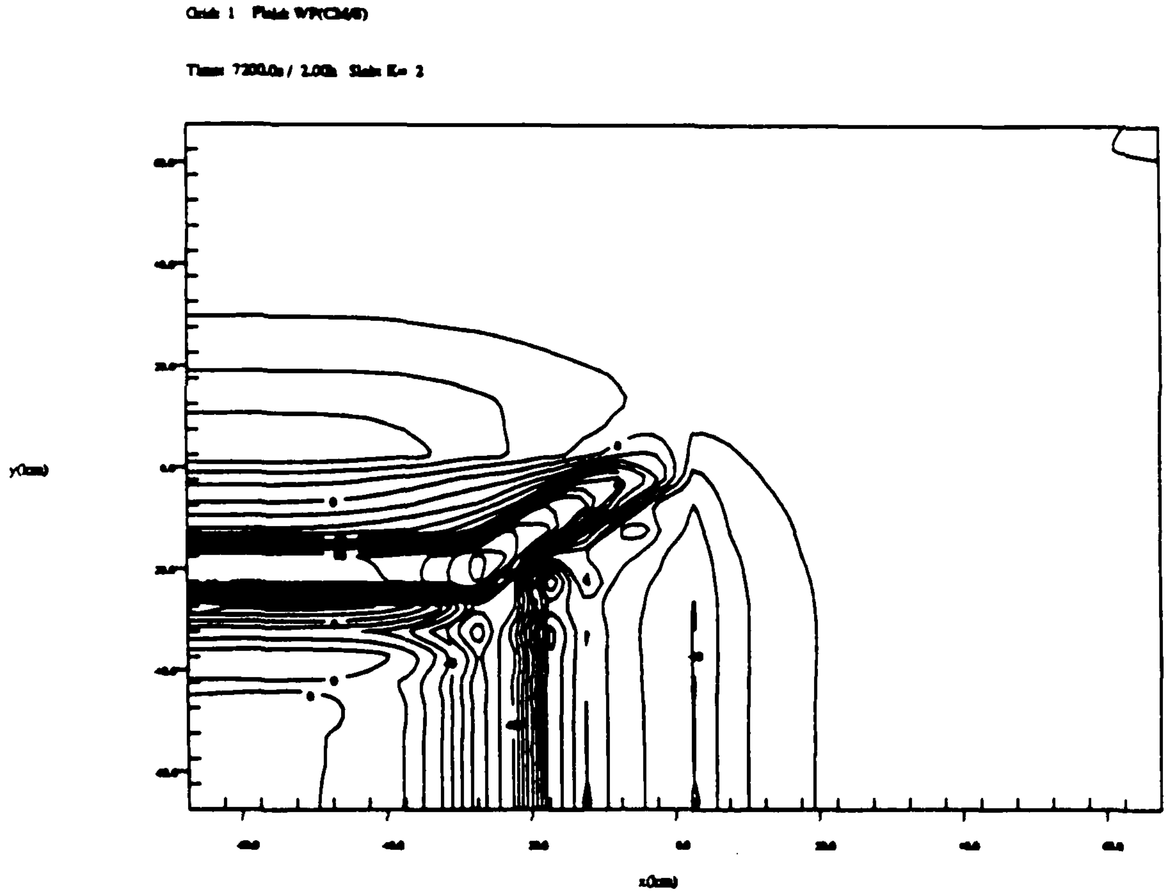

Figure 3.4c Horizontal cross section of the w-component of motion in the mixed-layer model version of the heated sloping terrain test simulation 2 hours into the simulation.

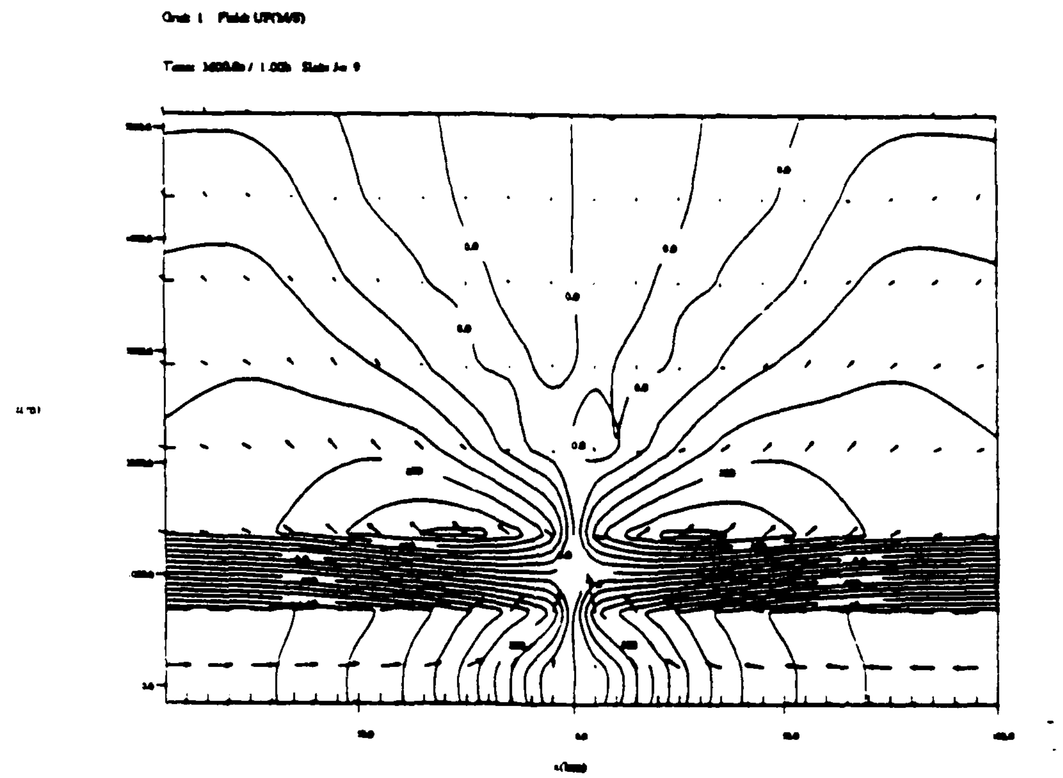

Figure 4.1a Vertical cross section of the u-component of motion in the full model version of the cartesian wind assimilation test 1 hour into the simulation.

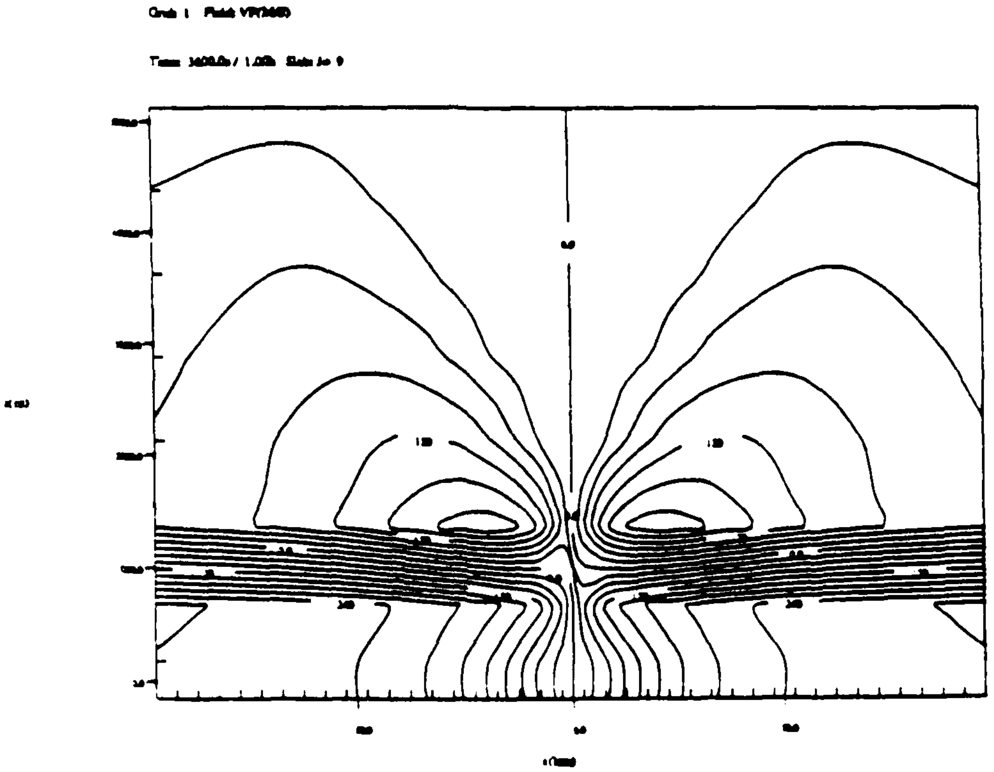

Figure 4.1b Vertical cross section of the v-component of motion in the full model version of the cartesian wind assimilation test 1 hour into the simulation.

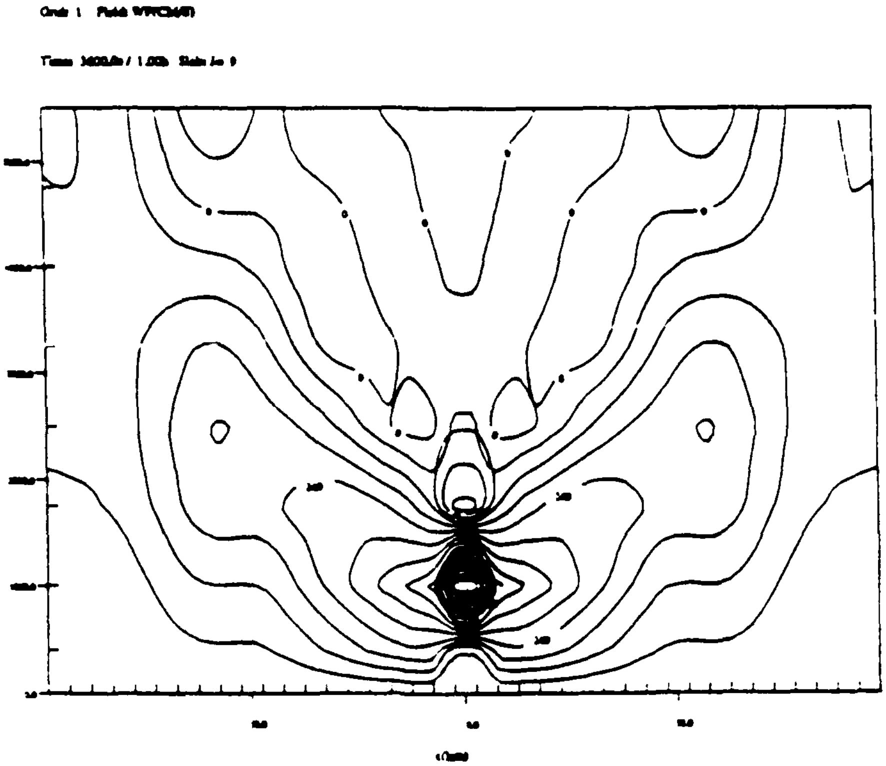

Figure 4.1c Vertical cross section of the w-component of motion in the full model version of the cartesian wind assimilation test 1 hour into the simulation.

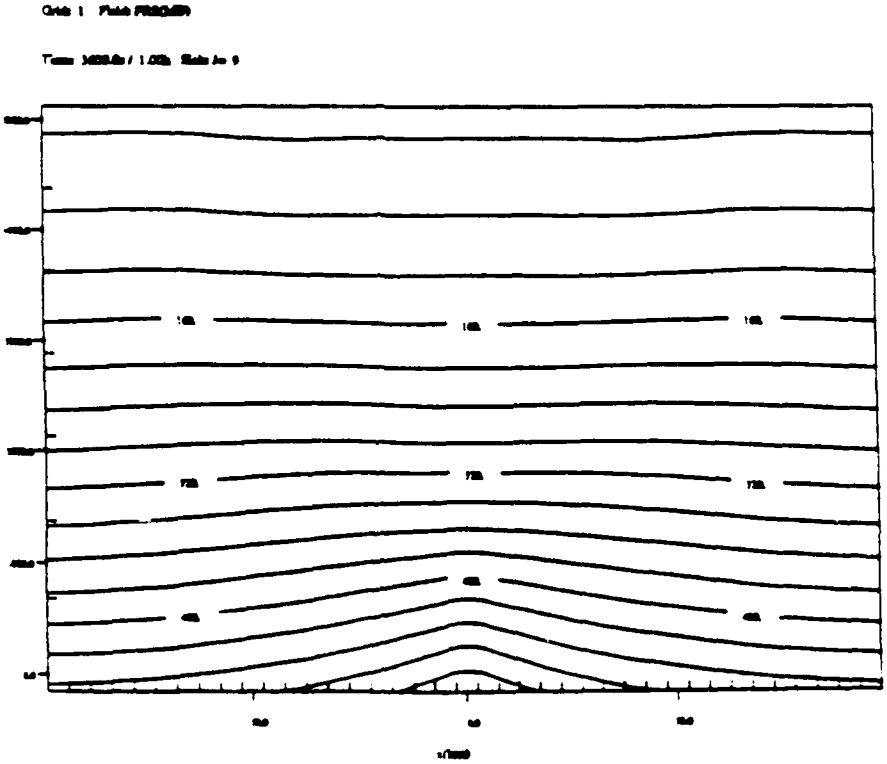

Figure 4.1d Vertical cross section of the perturbation pressure field in the full model version of the cartesian wind assimilation test 1 hour into the simulation.

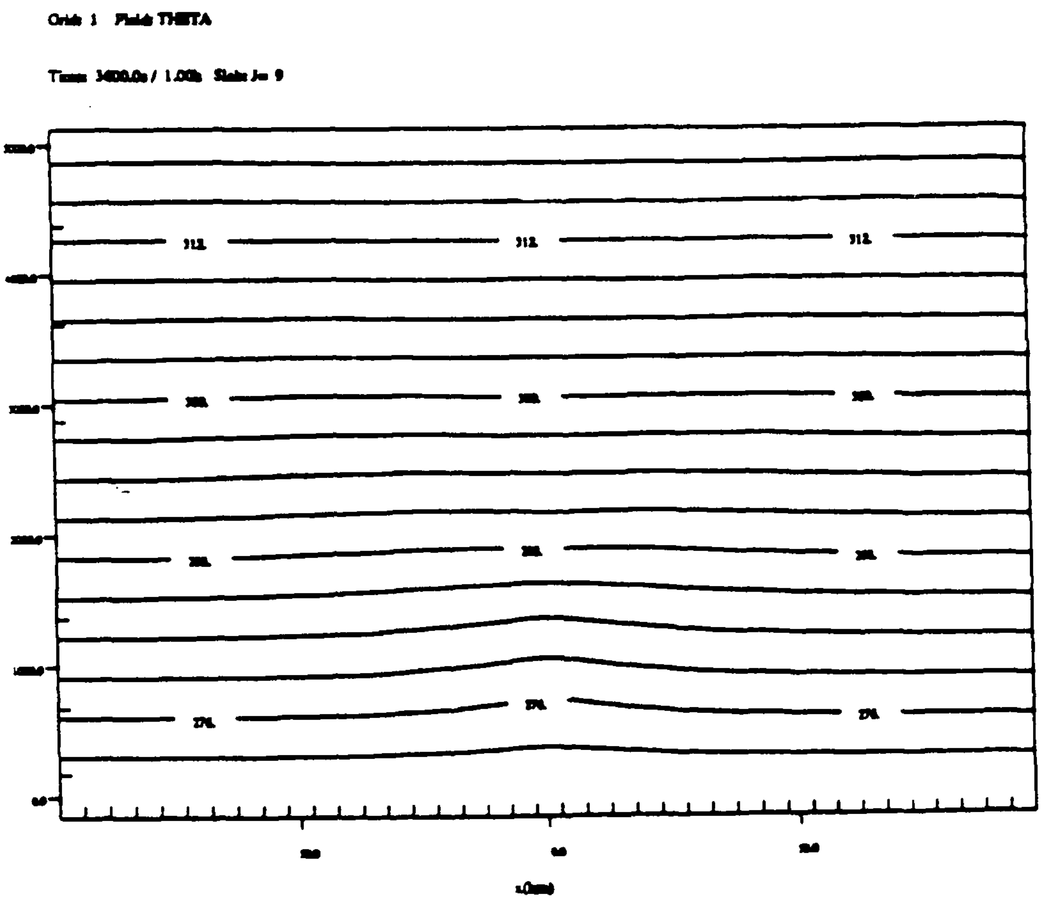

Figure 4.1e Vertical cross section of the potential temperature field in the full model version of the cartesian wind assimilation test 1 hour into the simulation.

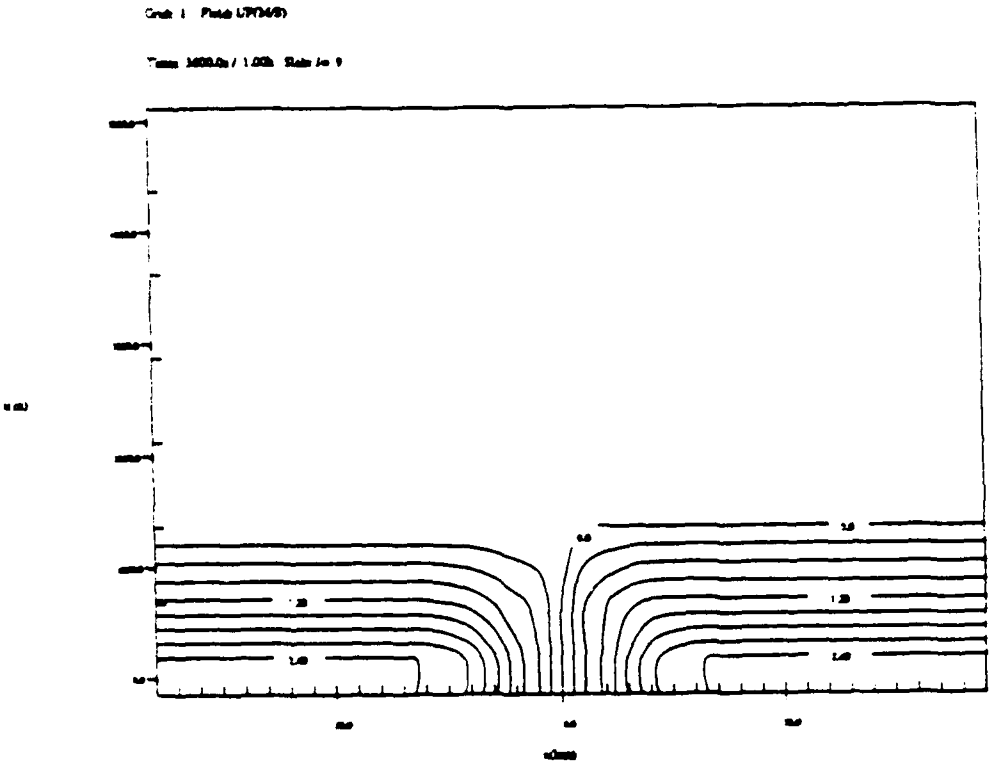

Figure 4.2a Vertical cross section of the u-component of motion in the mixed-layer model version of the cartesian wind assimilation test 1 hour into the simulation.

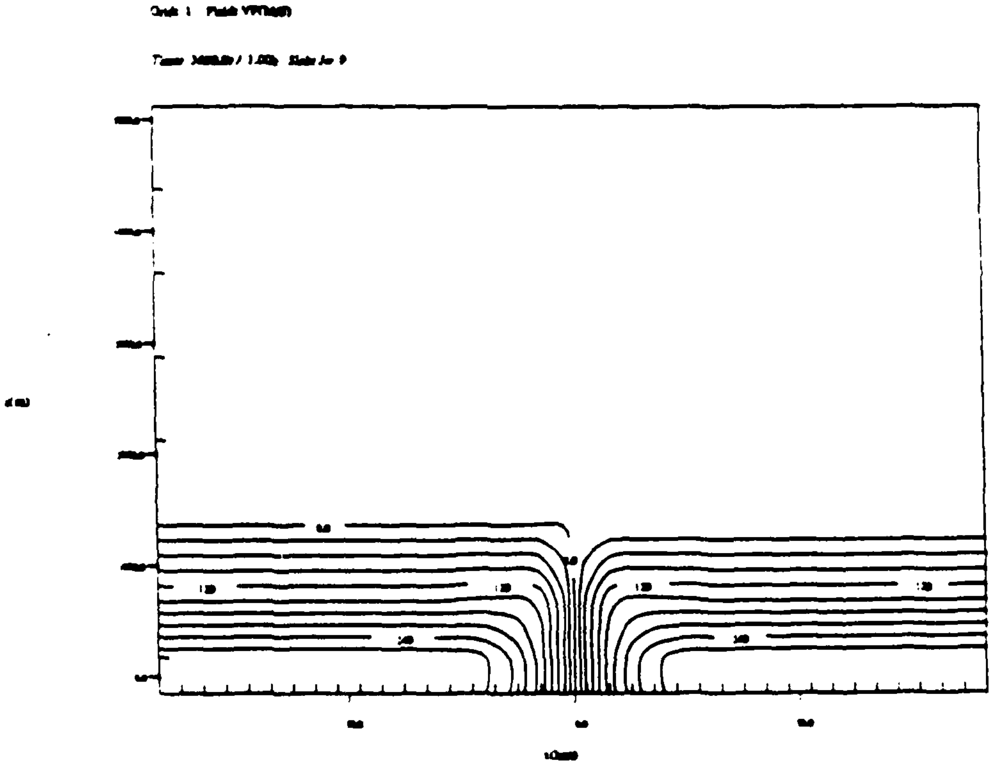

Figure 4.2b Vertical cross section of the v-component of motion in the mixed-layer model version of the cartesian wind assimilation test 1 hour into the simulation.

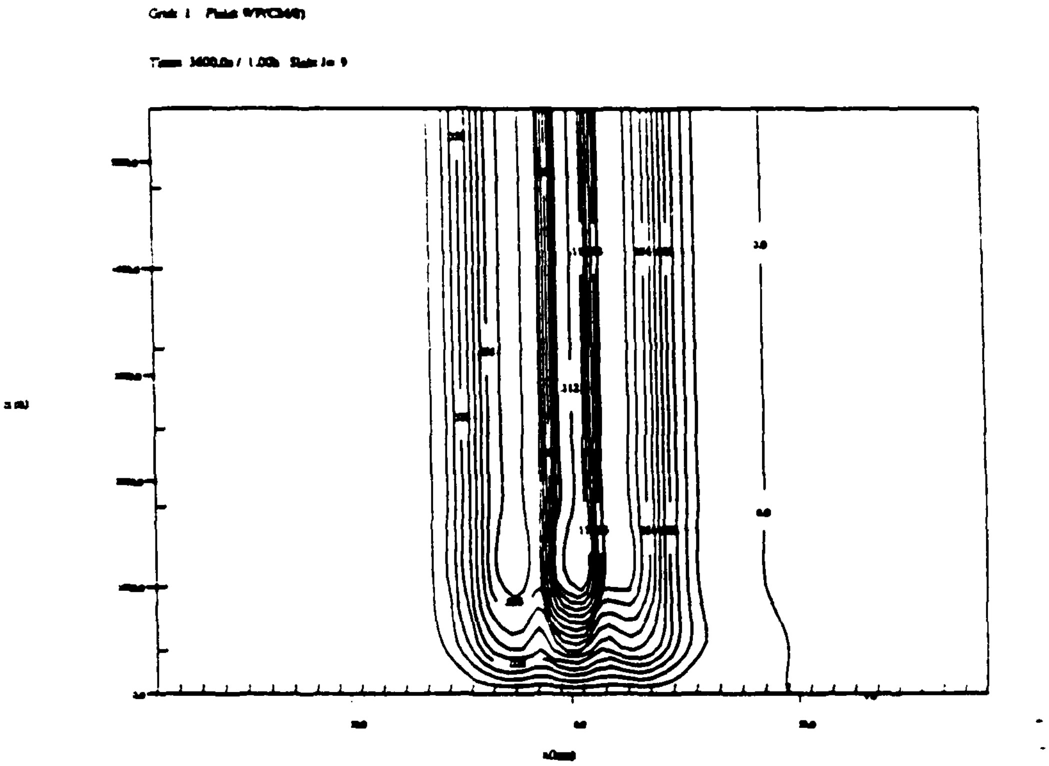

Figure 4.2c Vertical cross section of the w-component of motion in the mixed-layer model version of the cartesian wind assimilation test 1 hour into the simulation.

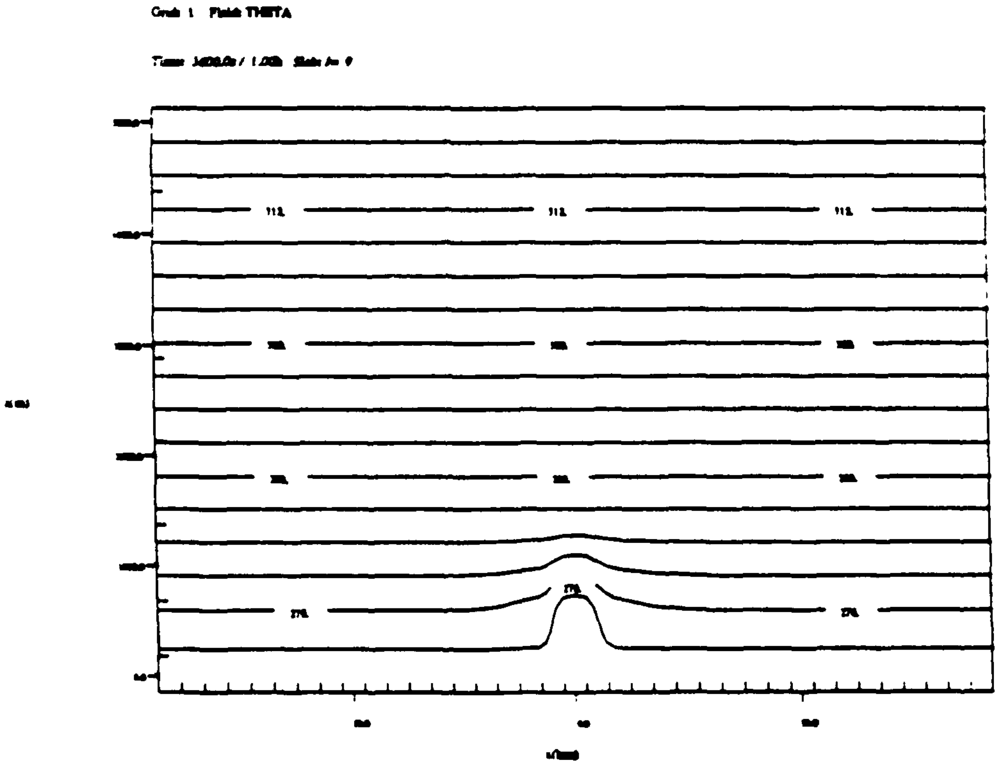

Figure 4.2d Vertical cross section of the potential temperature field in the mixed-layer model version of the cartesian wind assimilation test 1 hour into the simulation.

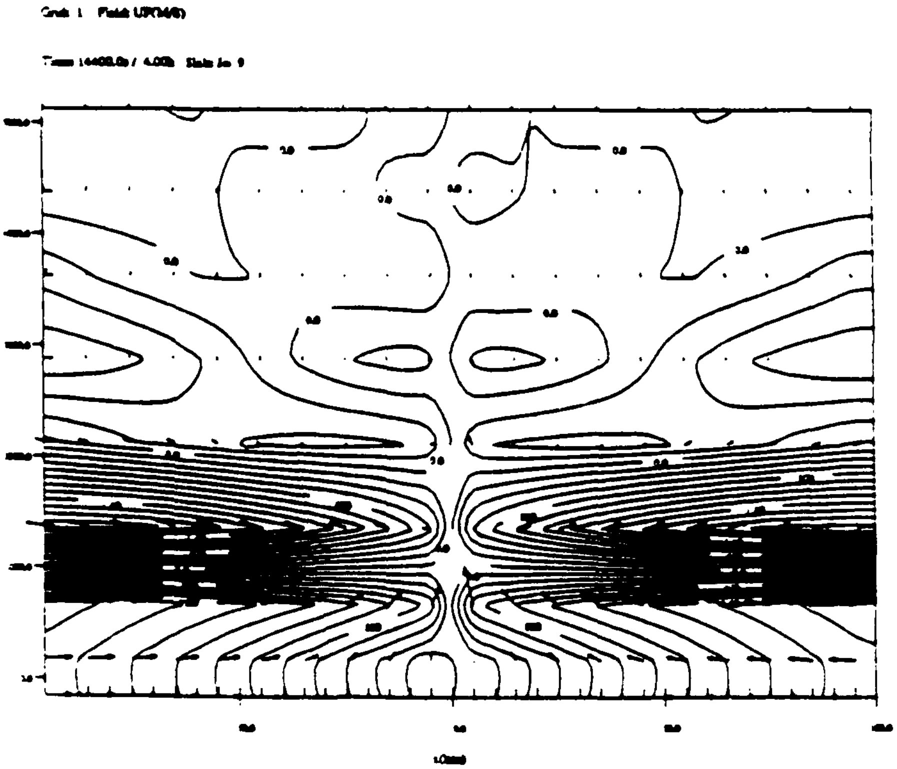

Figure 4.3a Vertical cross section of the u-component of motion in the full model version of the cartesian wind assimilation test 4 hours into the simulation.

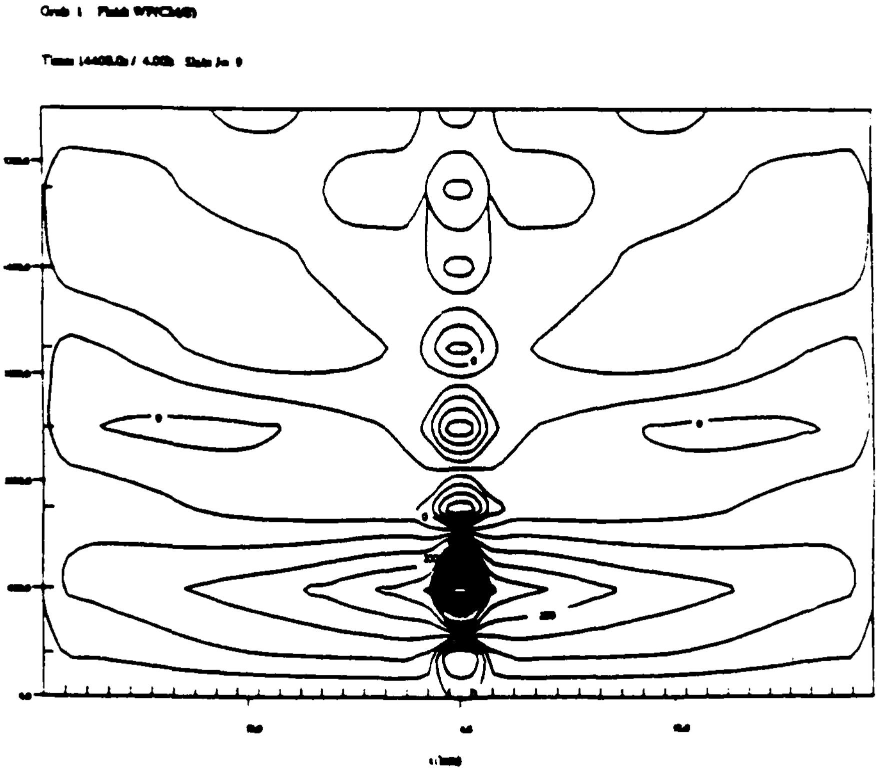

Figure 4.3b Vertical cross section of the w-component of motion in the full model version of the cartesian wind assimilation test 4 hours into the simulation.

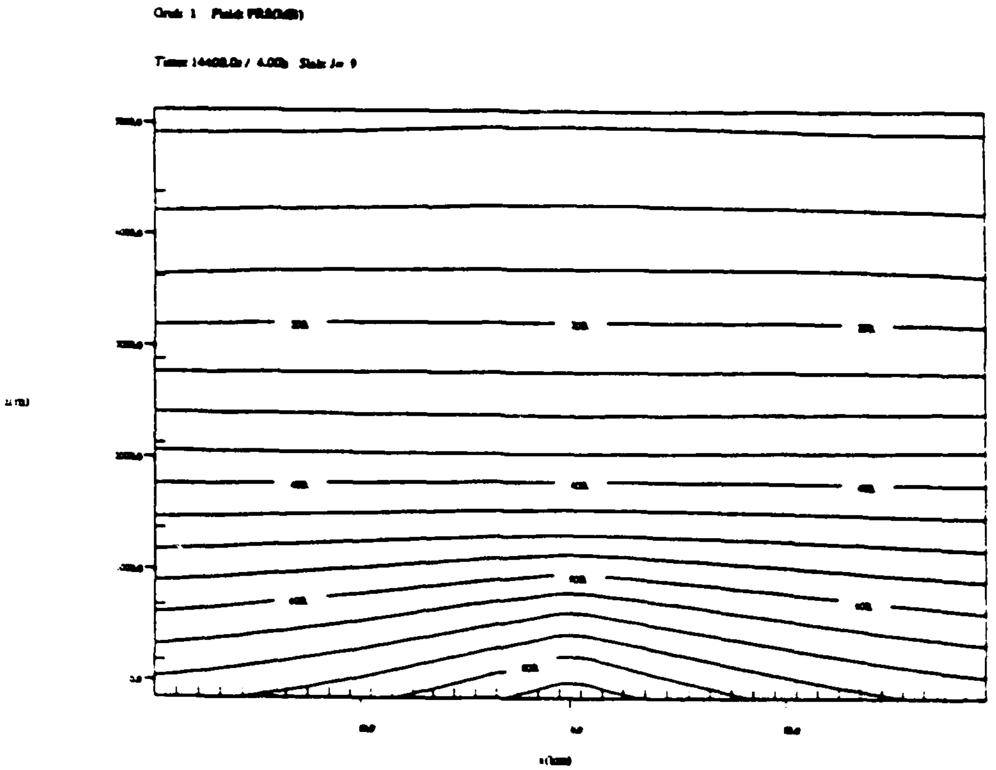

Figure 4.3c Vertical cross section of the perturbation pressure field in the full model version of the cartesian wind assimilation test 4 hours into the simulation.

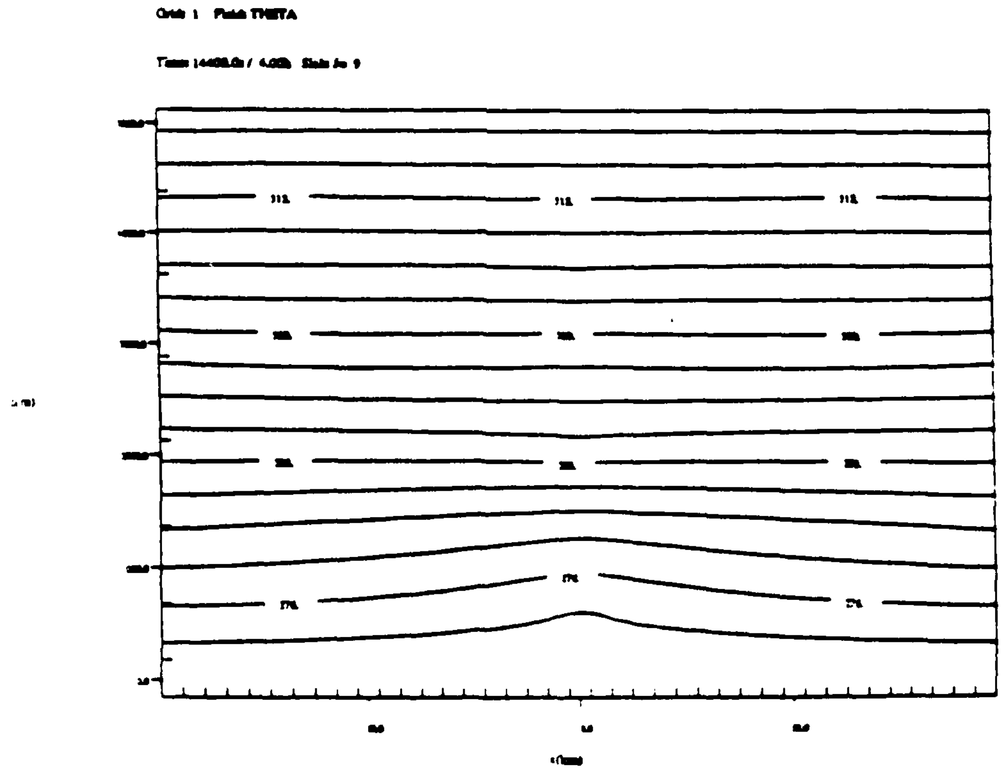

Figure 4.3d Vertical cross section of the potential temperature field in the full model version of the cartesian wind assimilation test 4 hours into the simulation.

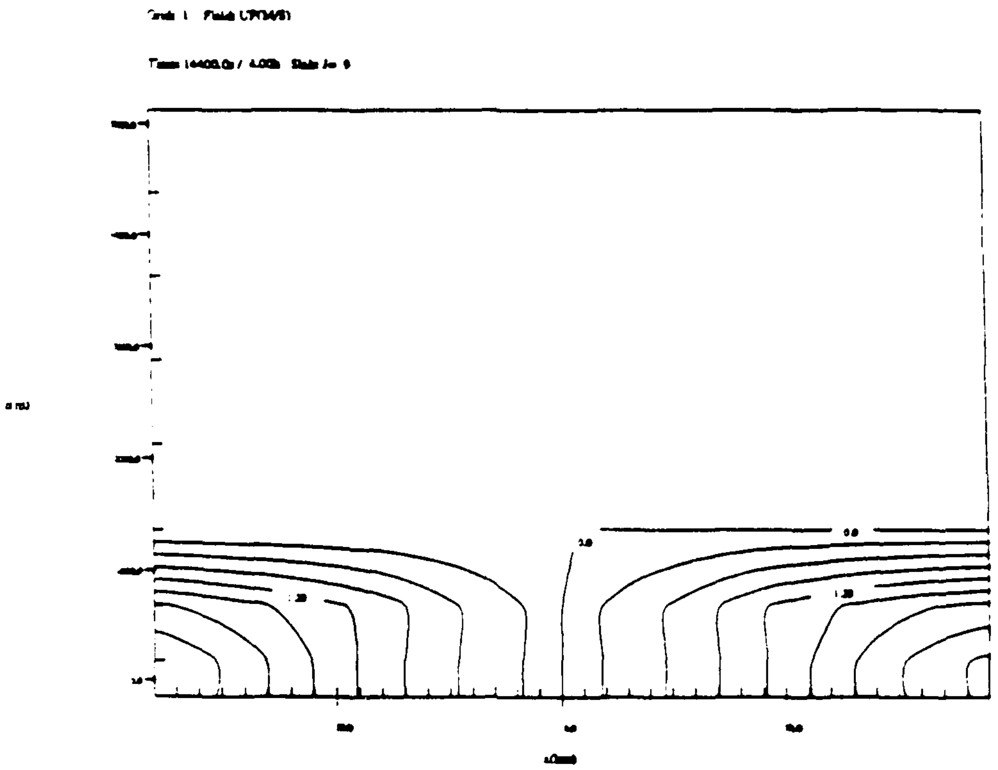

Figure 4.4a Vertical cross section of the u-component of motion in the mixed-layer model version of the cartesian wind assimilation test 4 hours into the simulation.

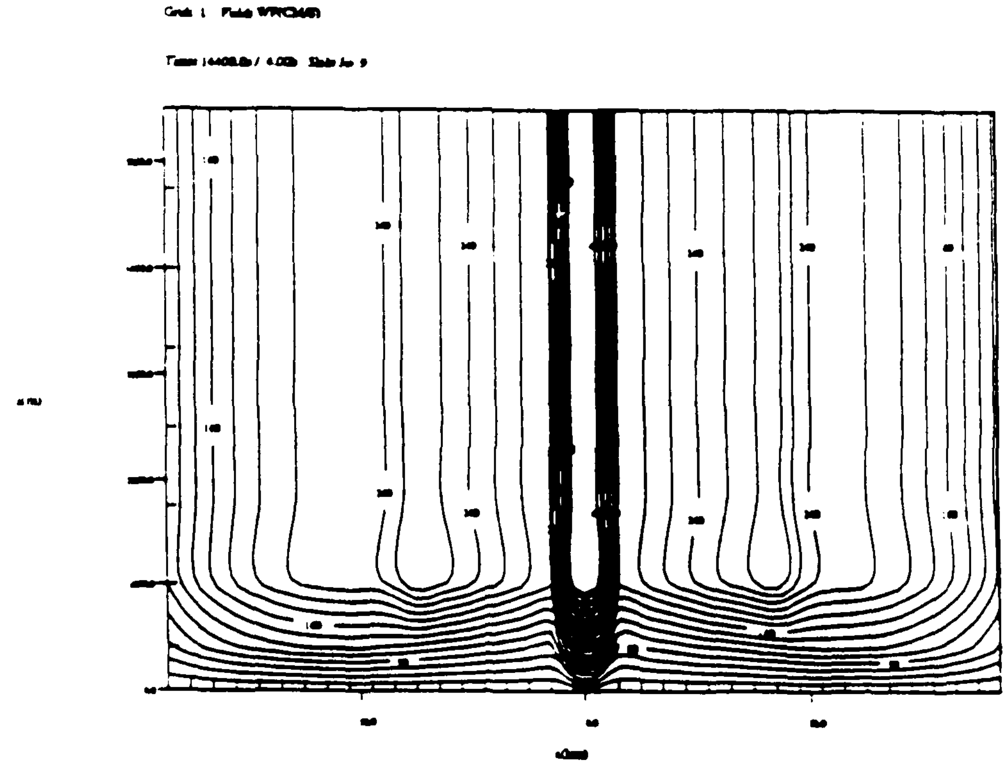

Figure 4.4b Vertical cross section of the w-component of motion in the mixed-layer model version of the cartesian wind assimilation test 4 hours into the simulation.

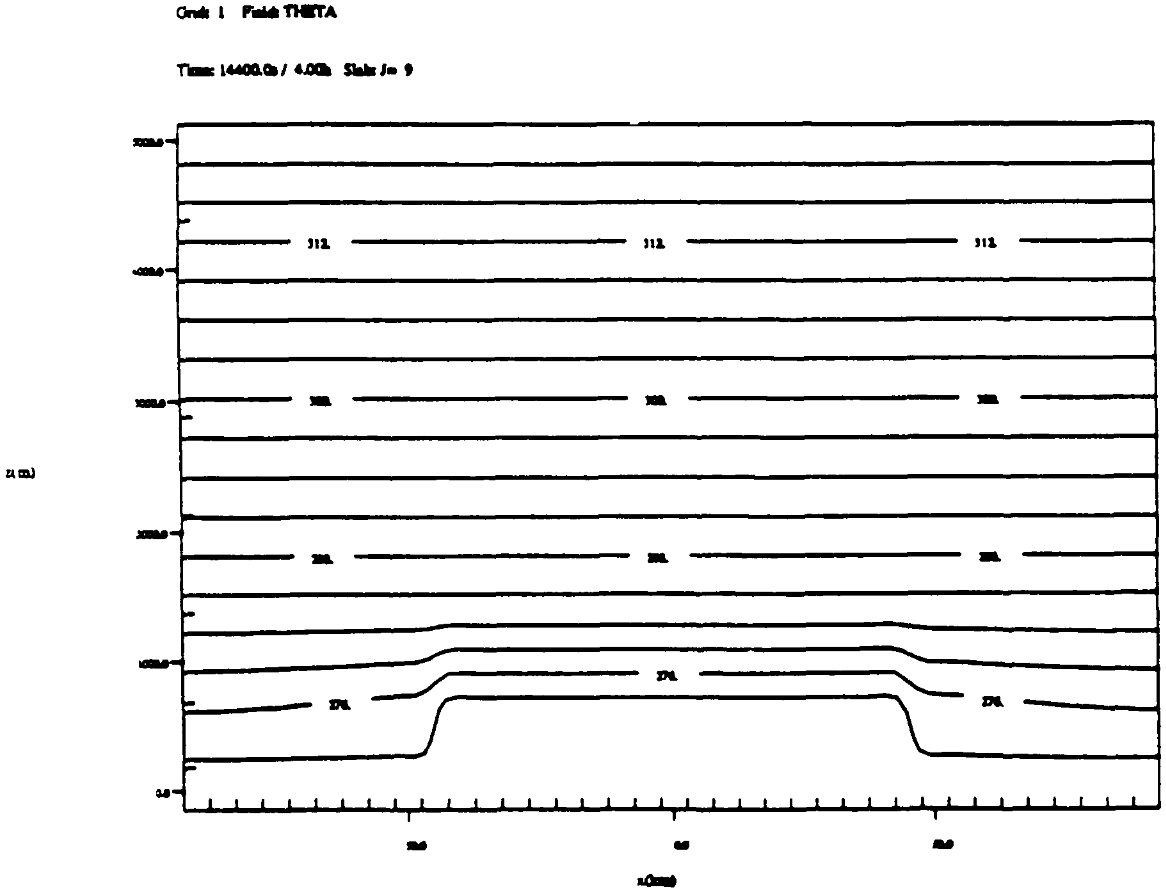

Figure 4.4c Vertical cross section of the potential temperature field in the mixed-layer model version of the cartesian wind assimilation test 4 hours into the simulation.

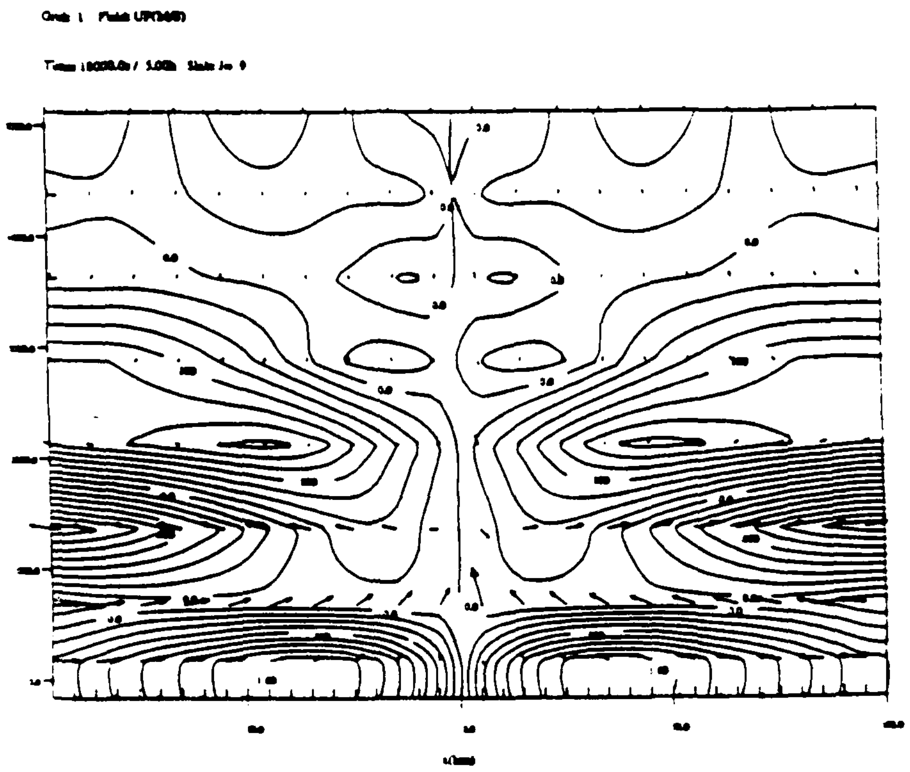

Figure 4.5a Vertical cross section of the u-component of motion in the full model version of the cartesian wind assimilation test 5 hours into the simulation.

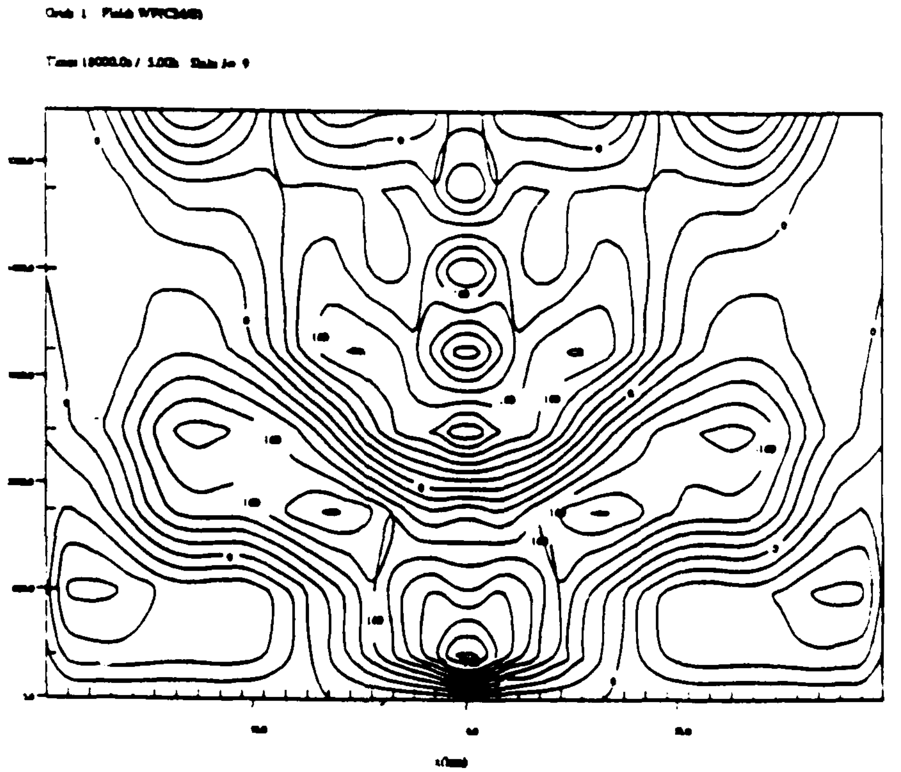

Figure 4.5b Vertical cross section of the w-component of motion in the full model version of the cartesian wind assimilation test 5 hours into the simulation.

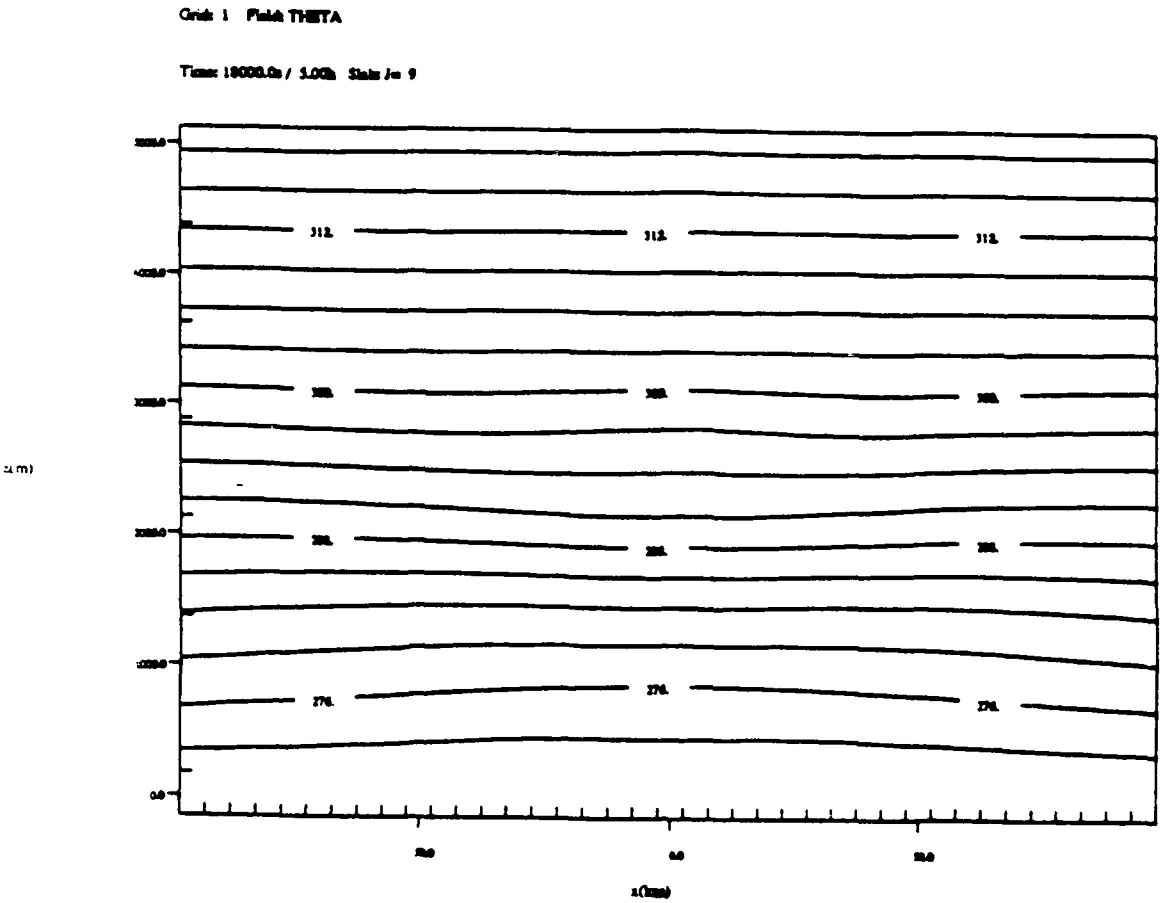

Figure 4.5c Vertical cross section of the potential temperature field in the full model version of the cartesian wind assimilation test 5 hours into the simulation.

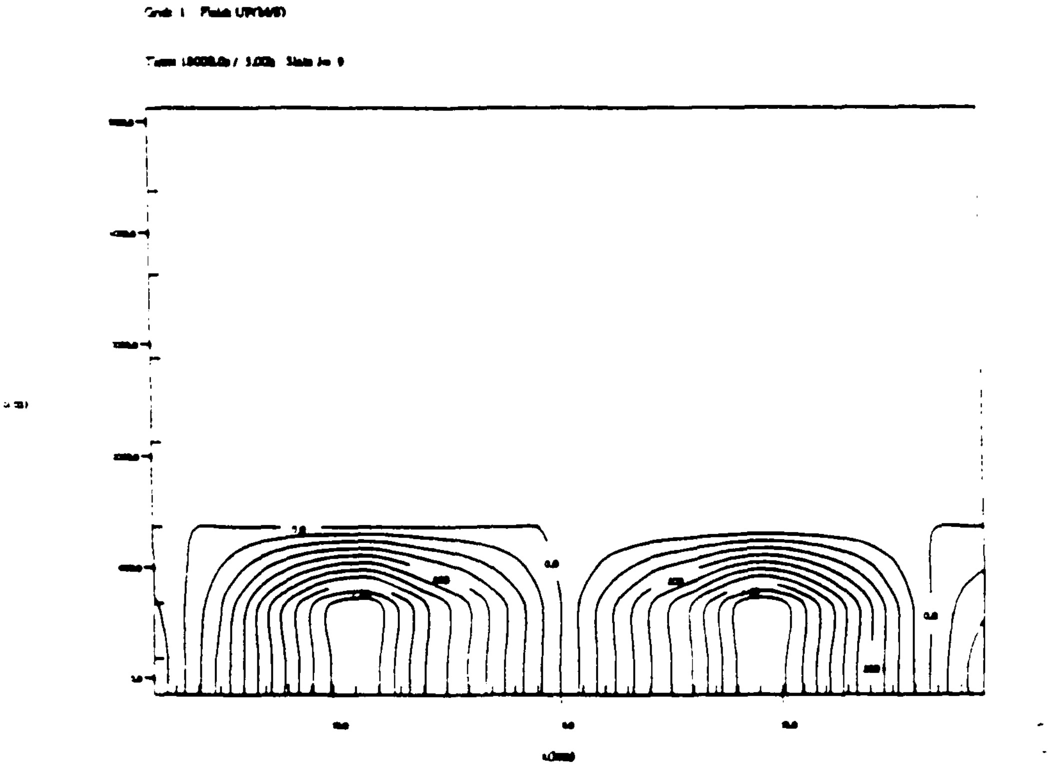

Figure 4.6a Vertical cross section of the u-component of motion in the mixed-layer model version of the cartesian wind assimilation test 5 hours into the simulation.

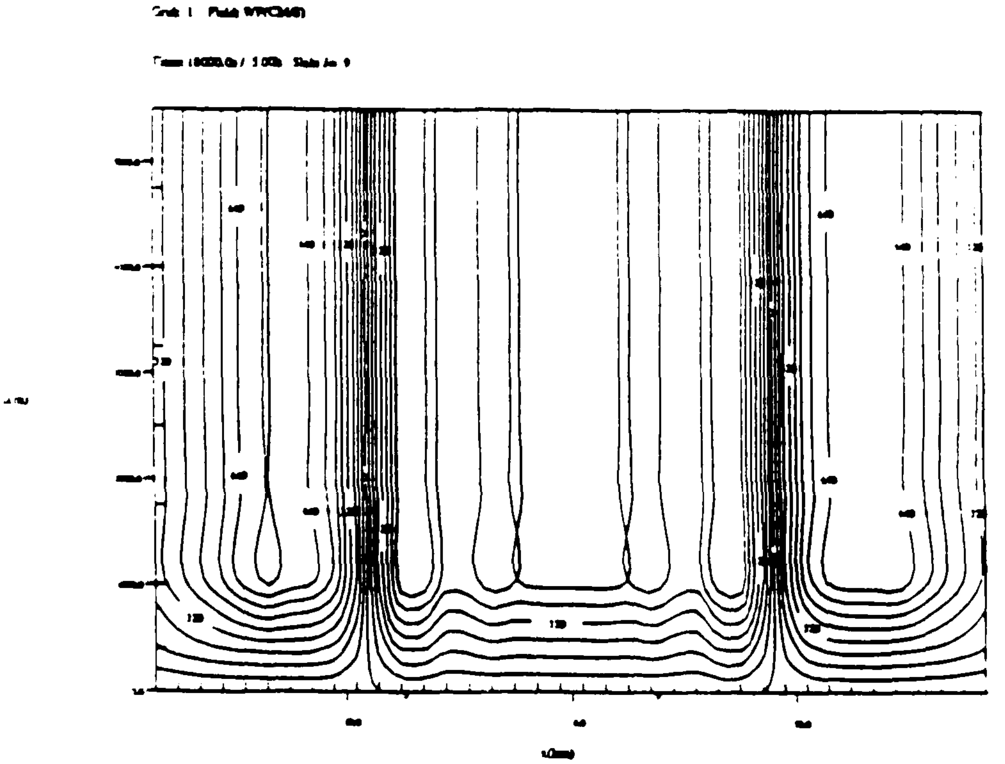

Figure 4.6b Vertical cross section of the w-component of motion in the mixed-layer model version of the cartesian wind assimilation test 5 hours into the simulation.

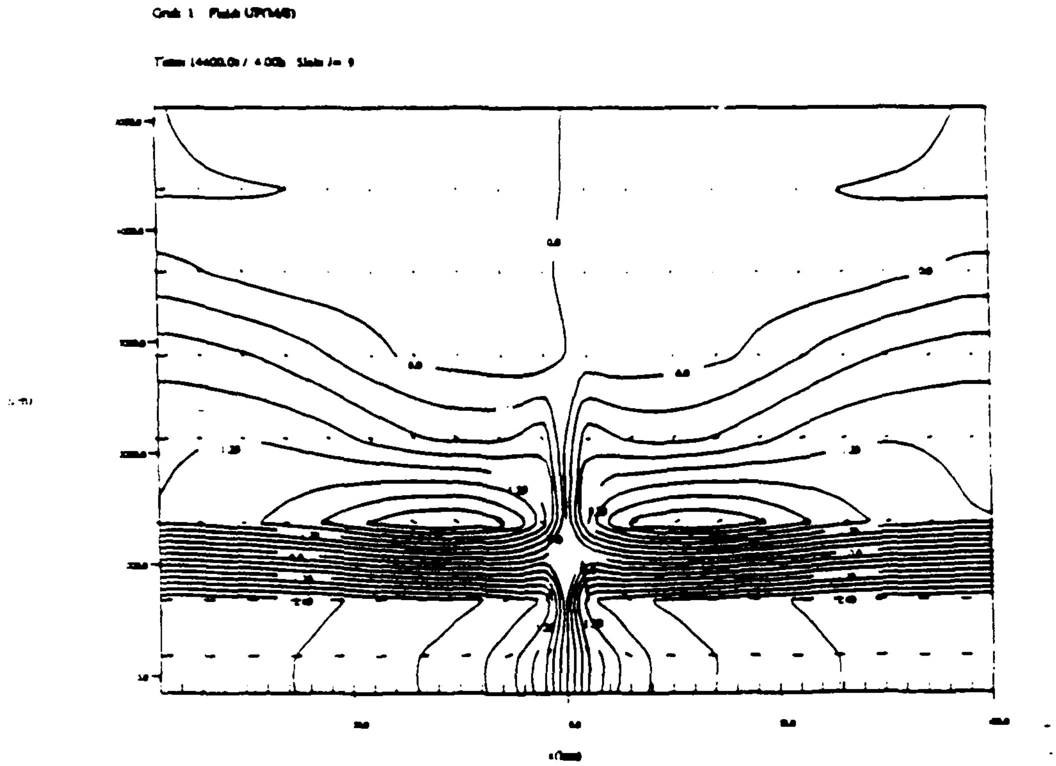

Figure 4.7 Vertical cross section of the u-component of motion in the full model version of the cartesian wind assimilation test for the neutral case 4 hours into the simulation.

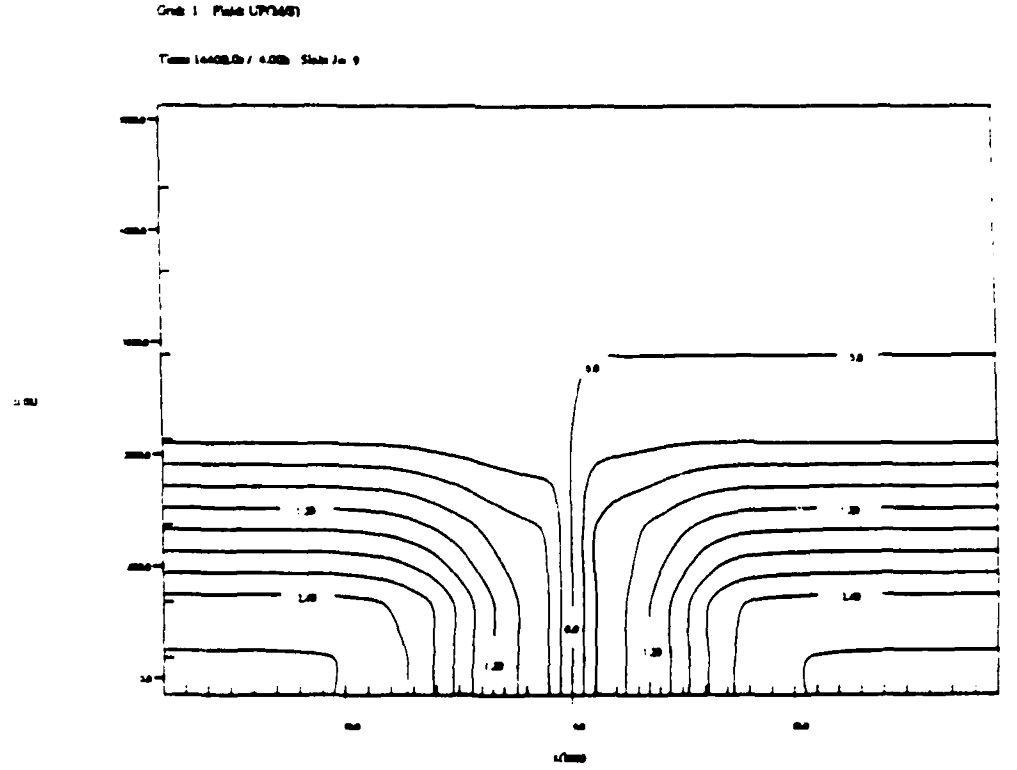

Figure 4.8 Vertical cross section of the u-component of motion in the mixed-layer model version of the cartesian wind assimilation test for the neutral case 4 hours into the simulation.

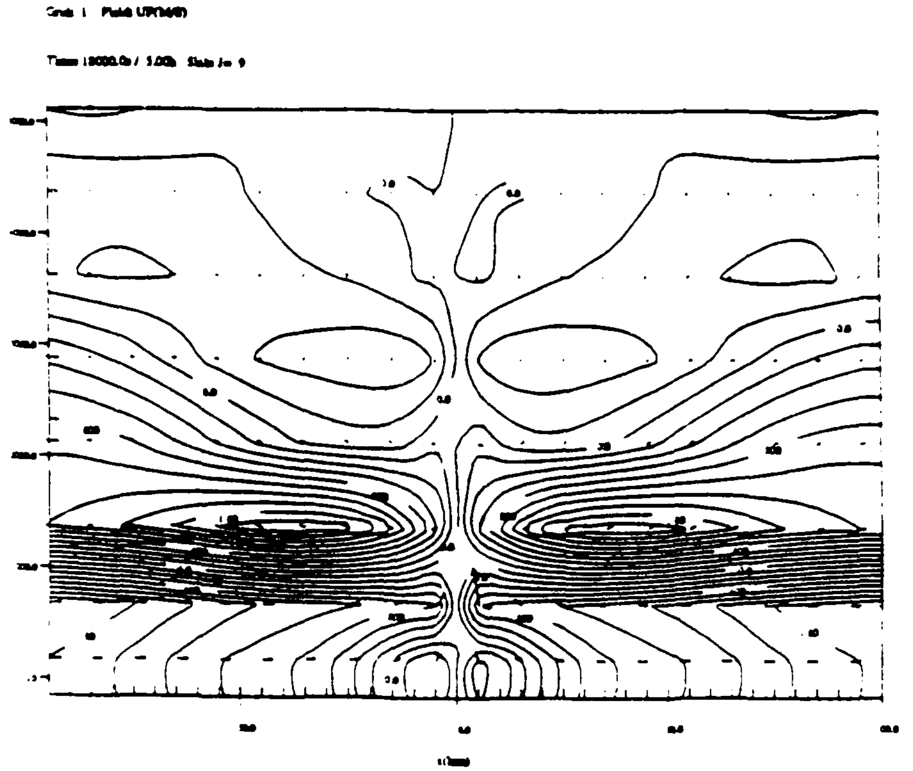

Figure 4.9 Vertical cross section of the u-component of motion in the full model version of the cartesian wind assimilation test for the neutral case 5 hours into the simulation.

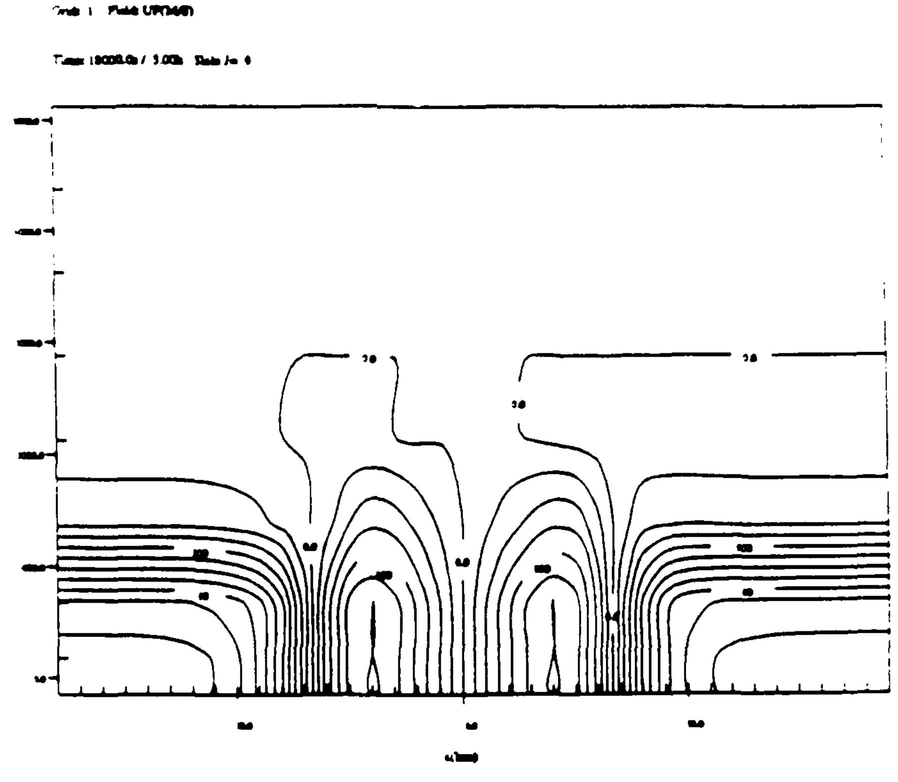

Figure 4.10 Vertical cross section of the u-component of motion in the mixed-layer model version of the cartesian wind assimilation test for the neutral case 5 hours into the simulation.

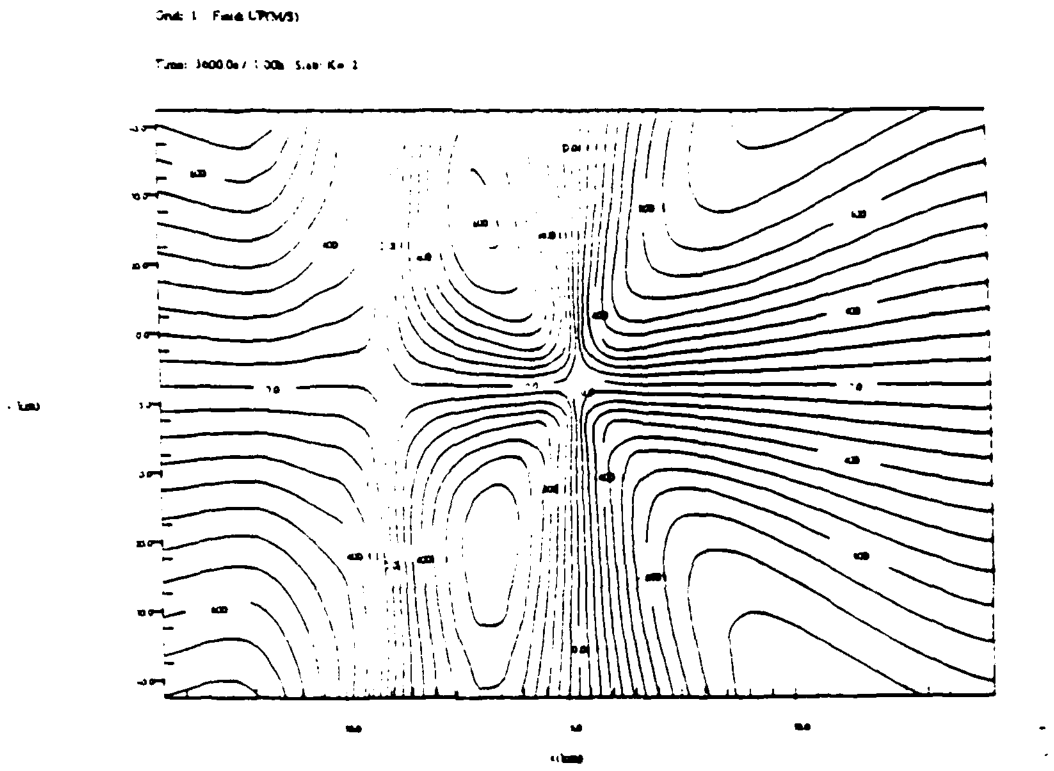

Figure 5.1a Horizontal cross section of the u-component of motion in the mixed-layer model version of the radial wind assimilation test 1 hour into the simulation.

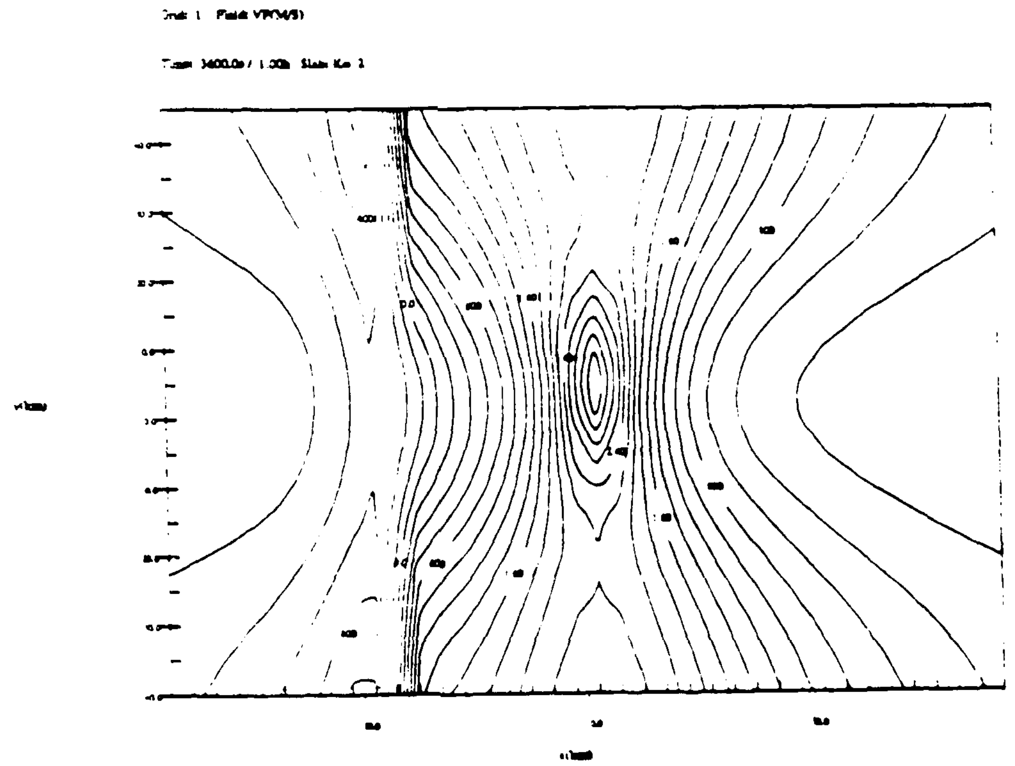

Figure 5.1b Horizontal cross section of the v-component of motion in the mixed-layer model version of the radial wind assimilation test 1 hour into the simulation.

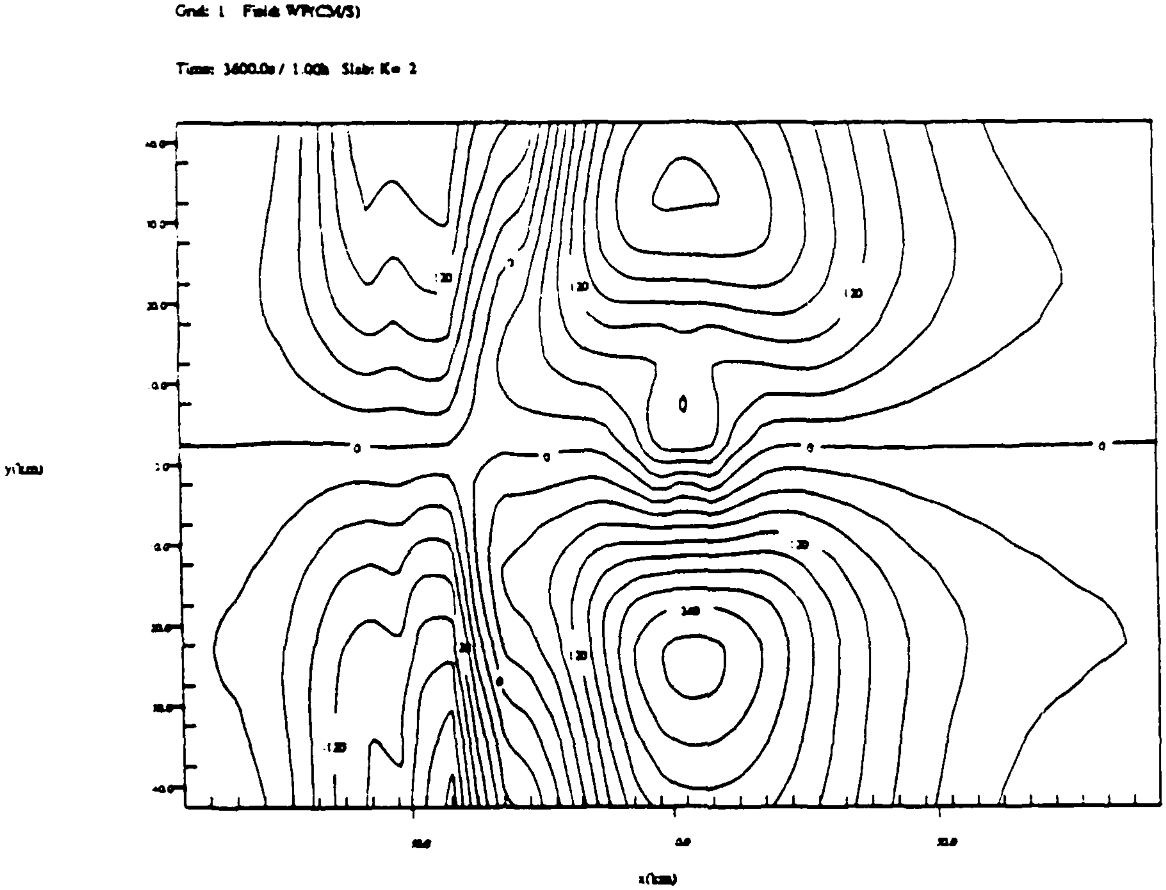

Figure 5.1c Horizontal cross section of the w-component of motion in the mixed-layer model version of the radial wind assimilation test 1 hour into the simulation.

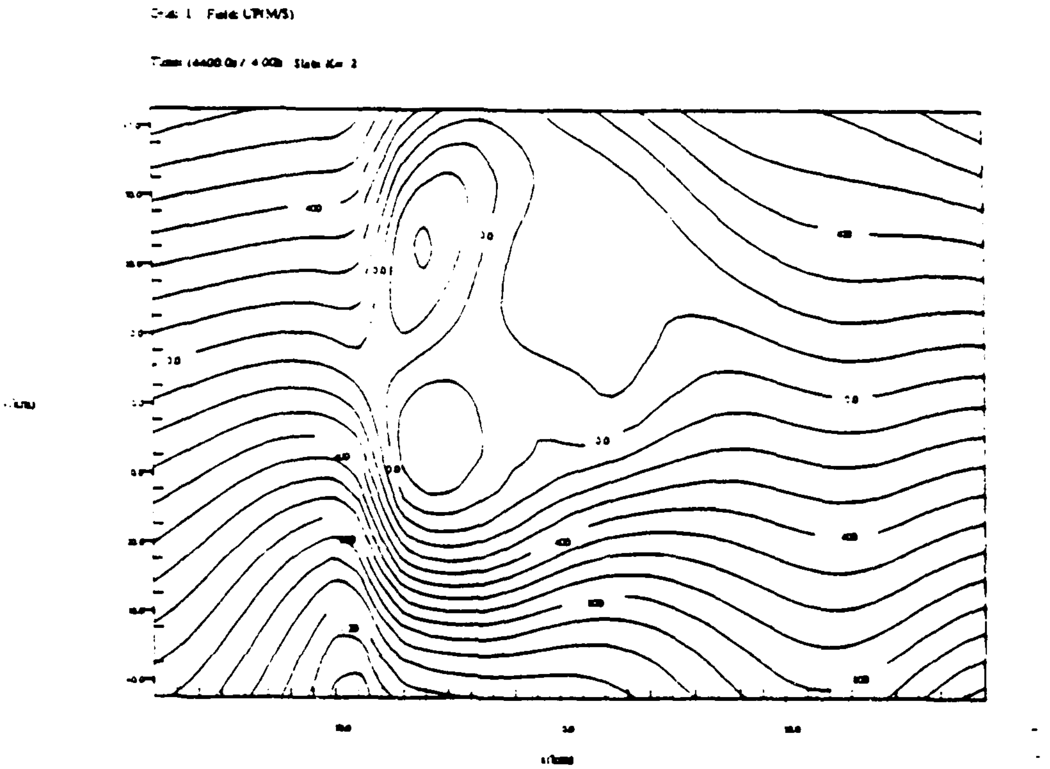

Figure 5.2a Horizontal cross section of the u-component of motion in the mixed-layer model version of the radial wind assimilation test 4 hours into the simulation.

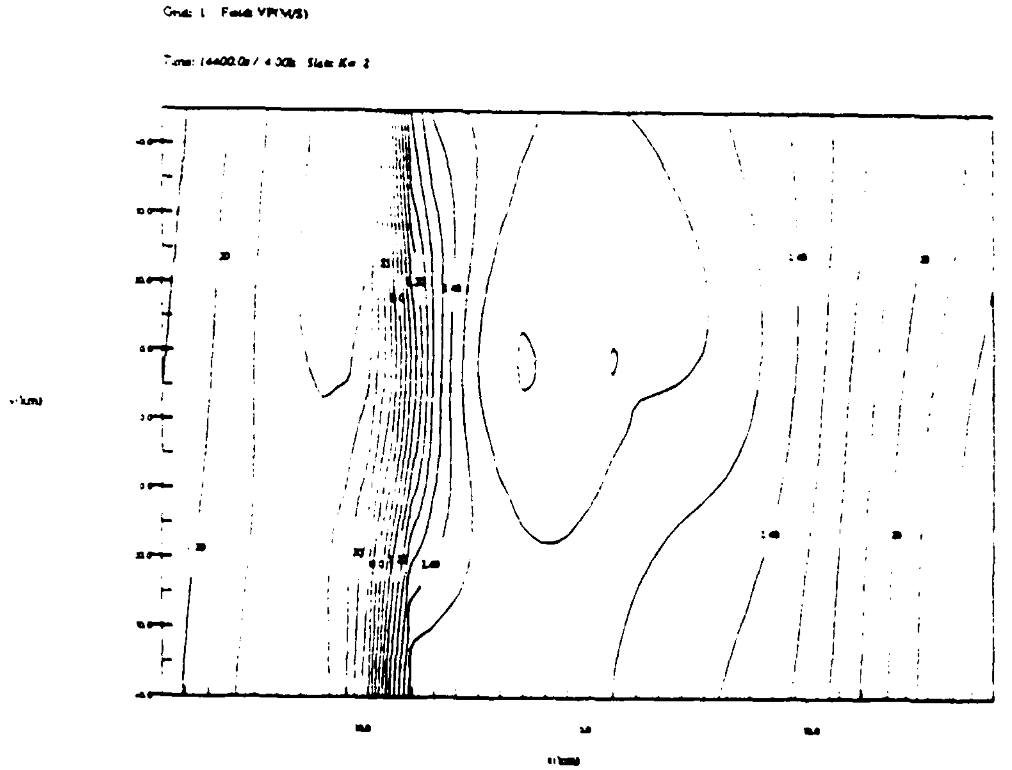

Figure 5.2b Horizontal cross section of the v-component of motion in the mixed-layer model version of the radial wind assimilation test 4 hours into the simulation.

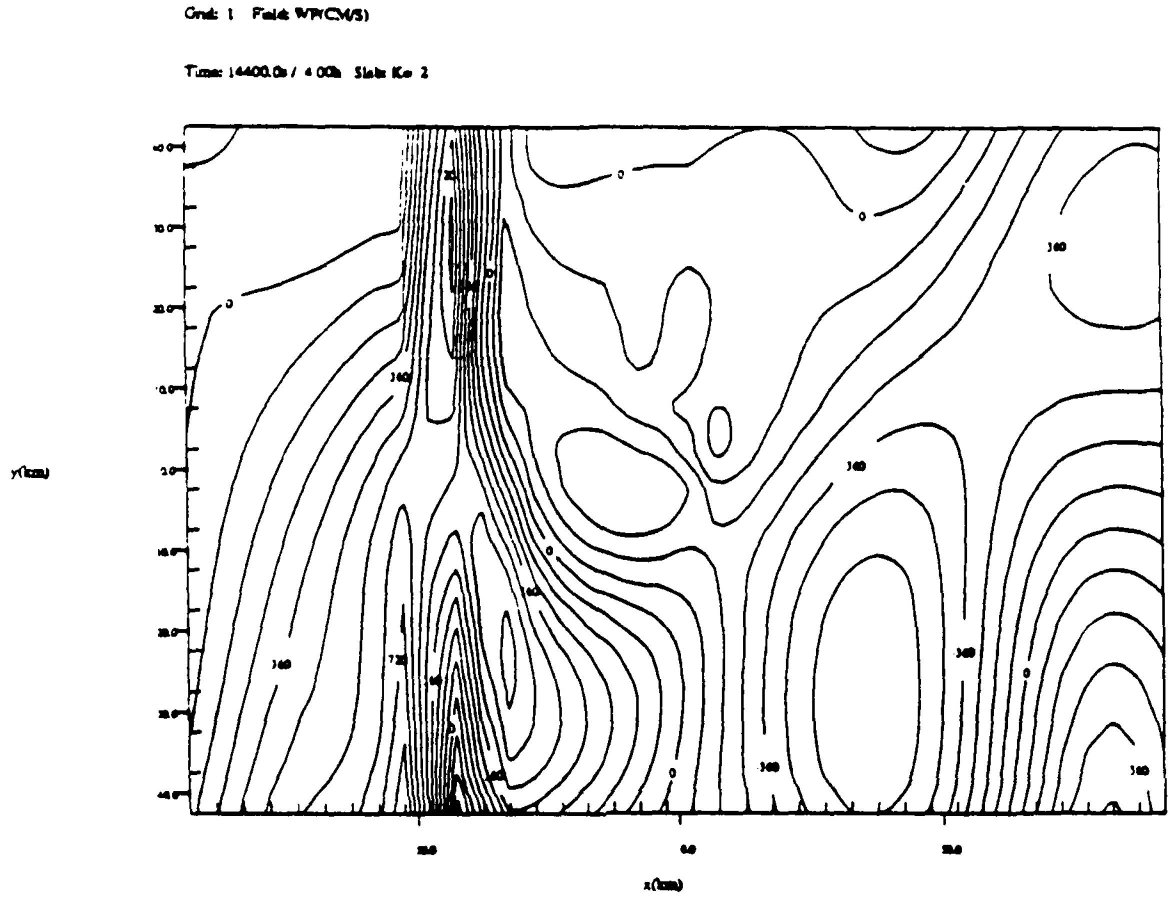

Figure 5.2c Horizontal cross section of the w-component of motion in the mixed-layer model version of the radial wind assimilation test 4 hours into the simulation.

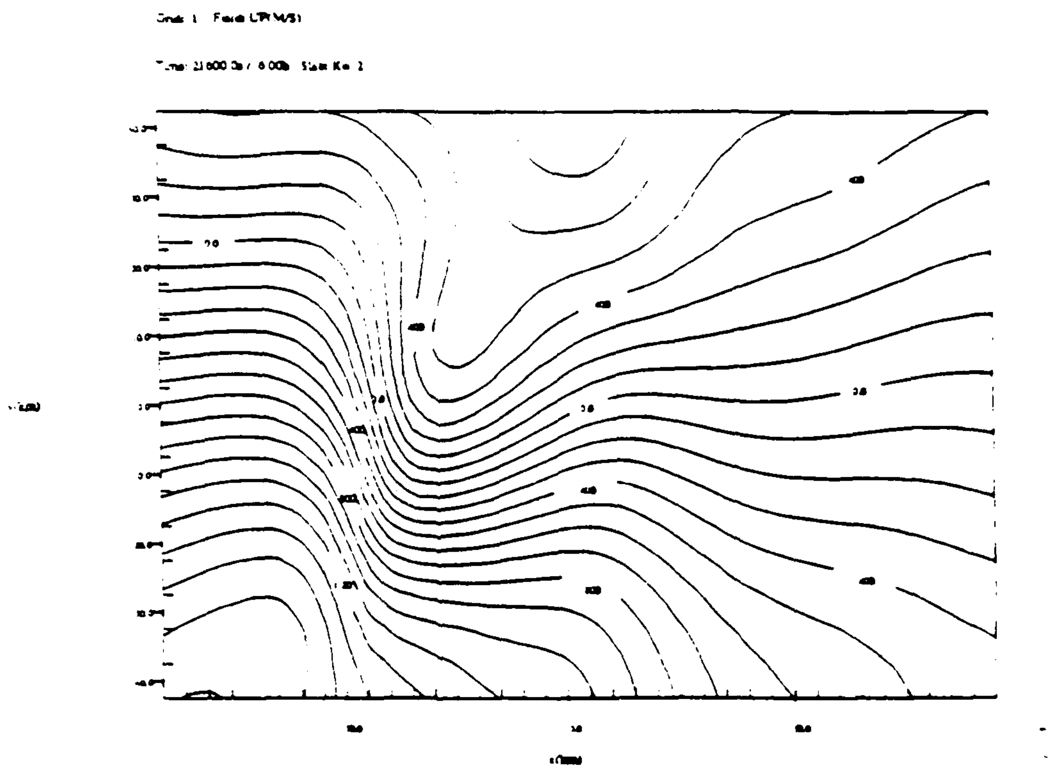

Figure 5.3a Horizontal cross section of the u-component of motion in the mixed-layer model version of the radial wind assimilation test 6 hours into the simulation.

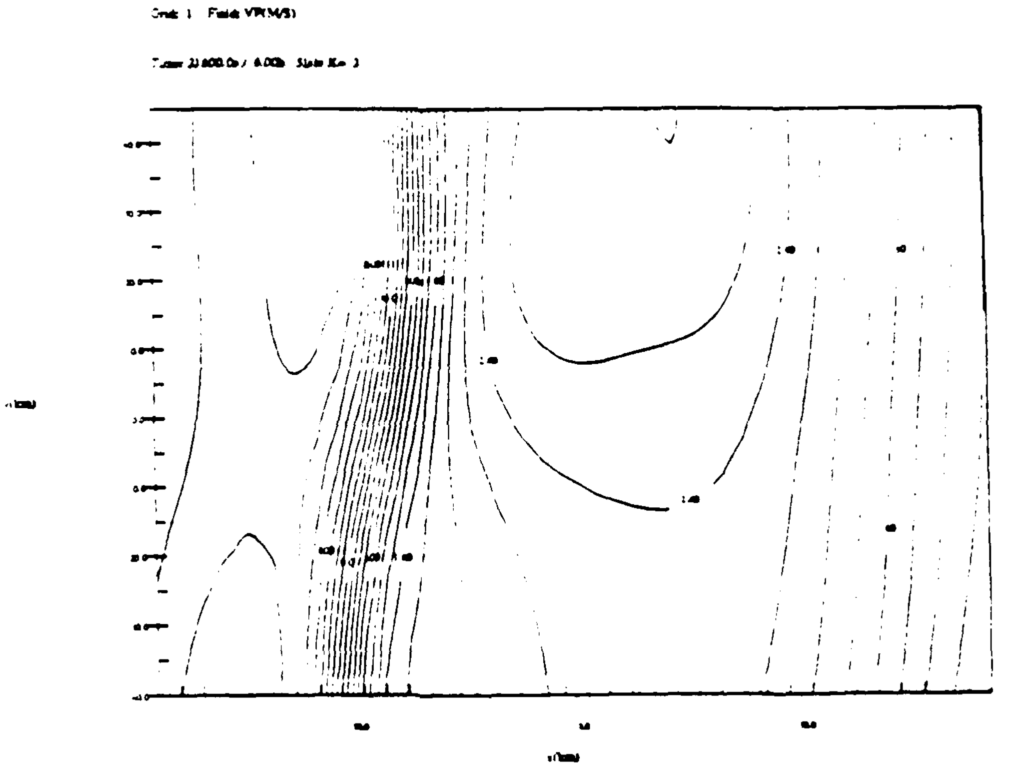

Figure 5.3b Horizontal cross section of the v-component of motion in the mixed-layer model version of the radial wind assimilation test 6 hours into the simulation.

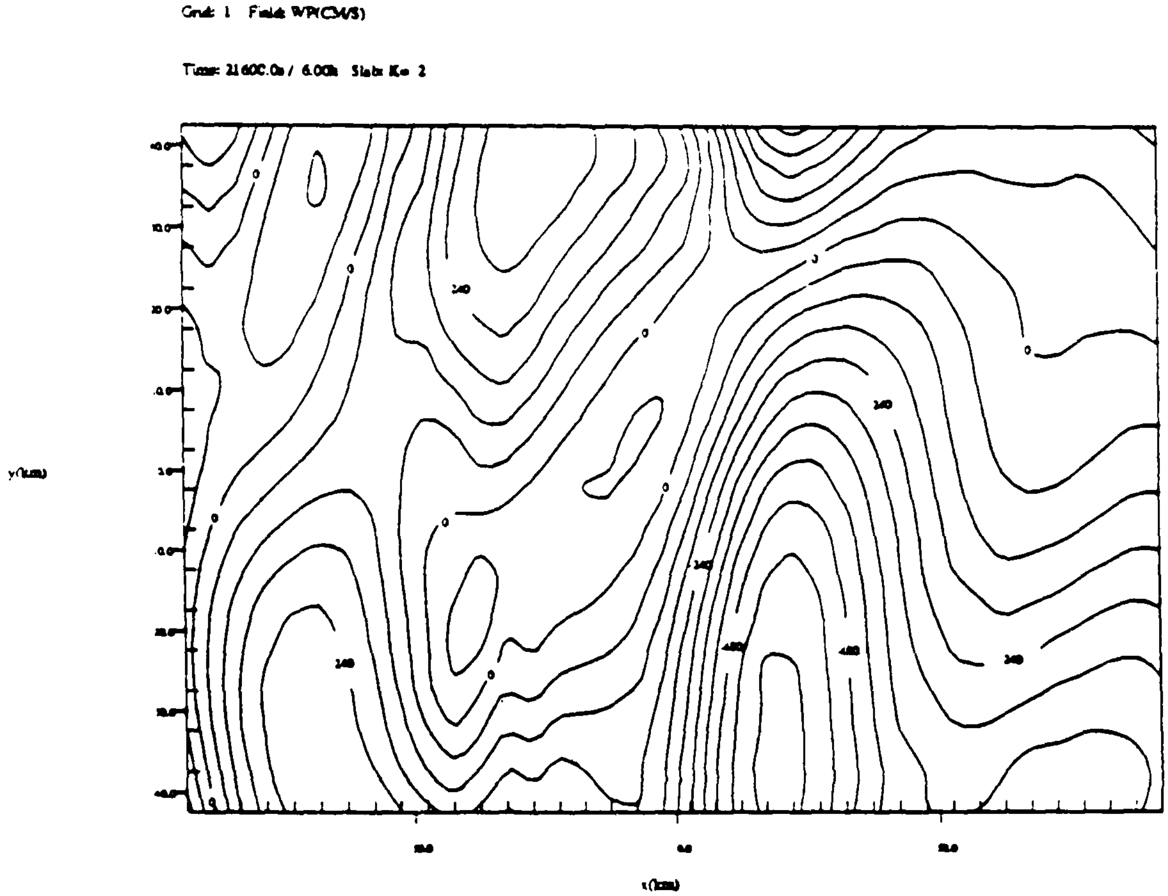

Figure 5.3c Horizontal cross section of the w-component of motion in the mixed-layer model version of the radial wind assimilation test 6 hours into the simulation.

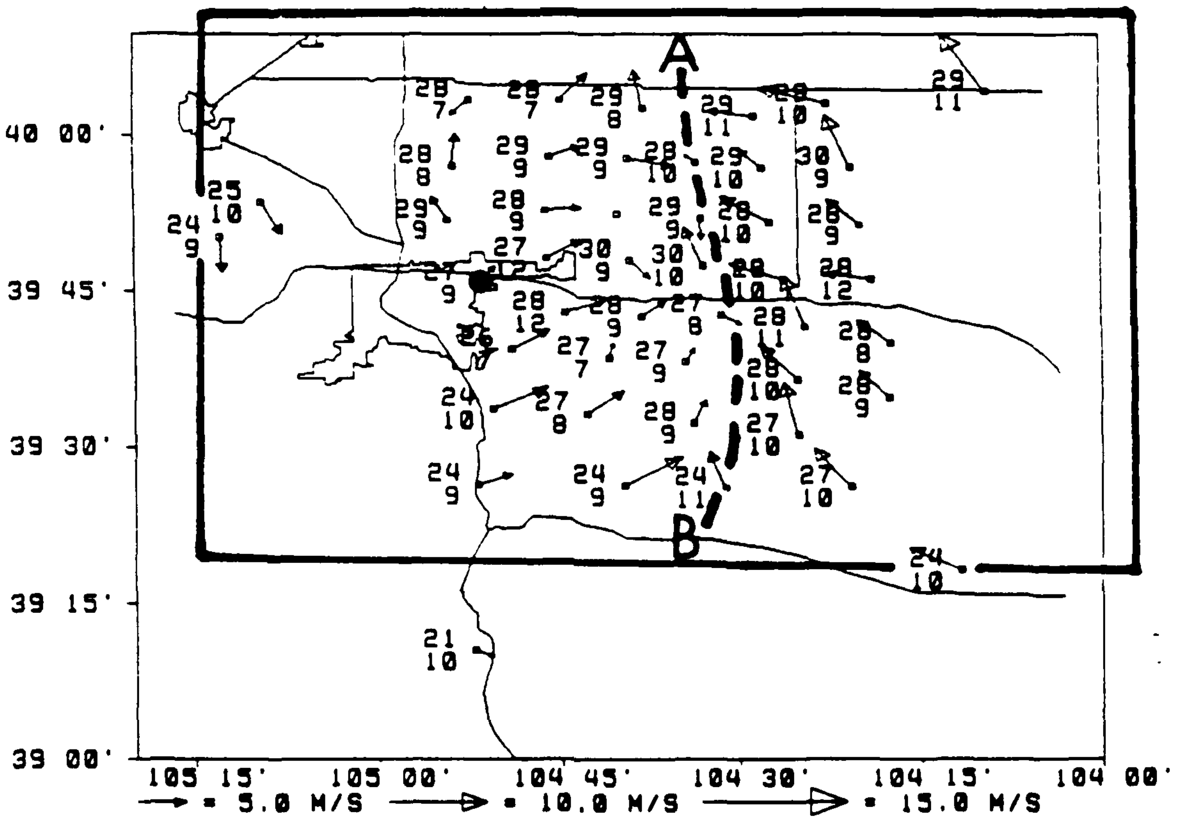

Figure 6.1a PAM mesonet observations of wind, temperature and dewpoint at 1500 local time (LT) 17 July 1987 (case 1). Bold box is boundary of 100 by 100 km computational domain (the x and y scales differ), large dot denotes the off-centered CP-3 radar position in this domain, and the dashed line A-B denotes the dominant north-south convergence line on this afternoon.

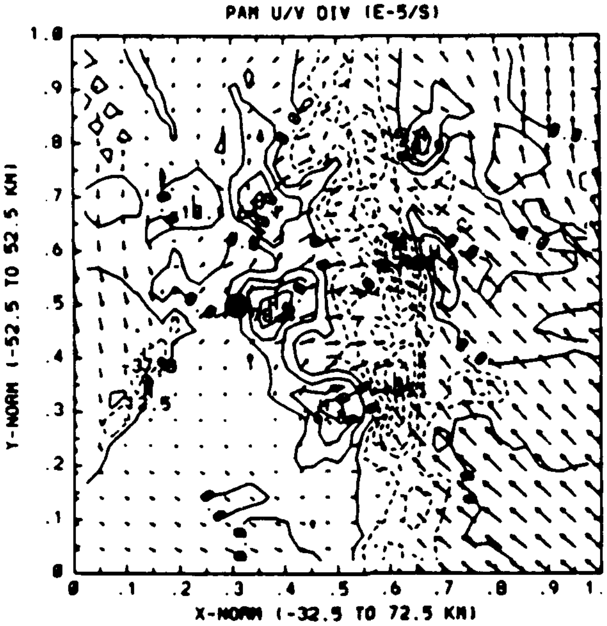

Figure 6.1b PAM winds from Figure 6.1a, objectively analyzed onto the 100 by 100 computational grid (with an extra grid point in each direction to accomodate the grid staggering used in the model). Wind vectors are shown at 5 km intervals (every other grid point). The divergence field computed from this wind field is contoured. CP-3 radar is located at the dot near the normalized (x,y) coordinate of (0.3,0.5).

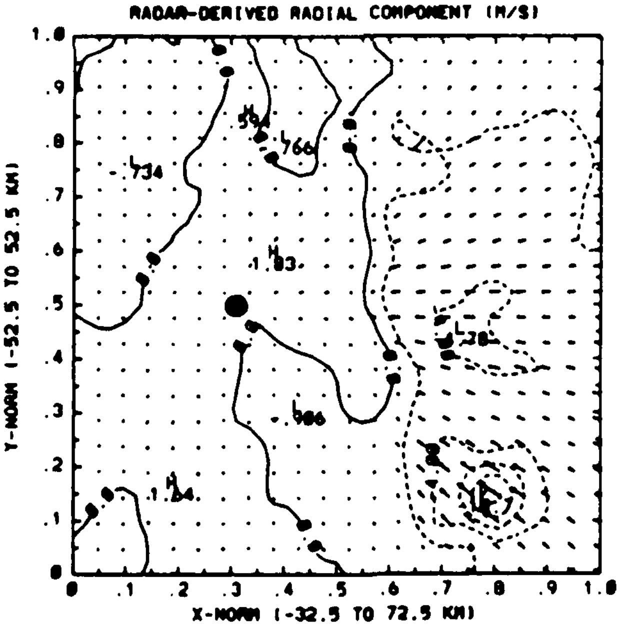

Figure 6.1c Radar-derived radial velocity field over the computational domain. Contoured field is radial wind speed (away from radar is positive). Dot denotes the radar position.

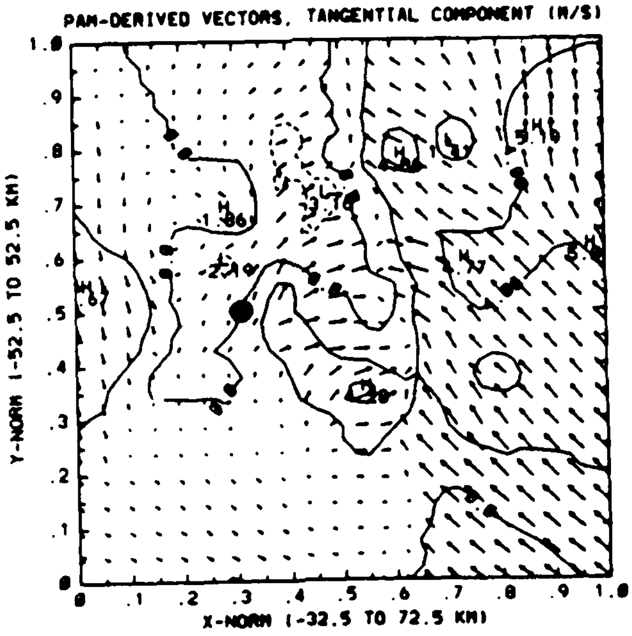

Figure 6.1d Contoured tangential wind component of the PAM-derived wind field (cyclonic motion around radar is positive). Dot denotes radar position.

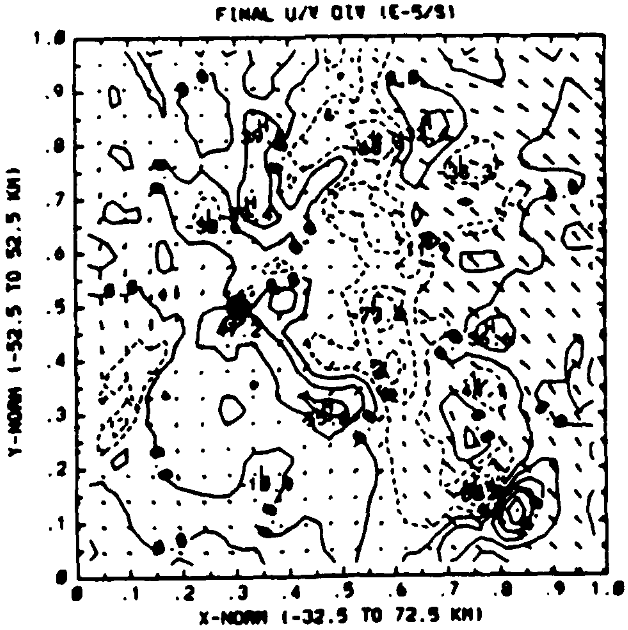

Figure 6.1e Final vector wind field for model input, derived by combining the radial and tangential components from Figures 6.1c,d. The divergence field computed from this wind field is contoured. Dot denotes radar location.

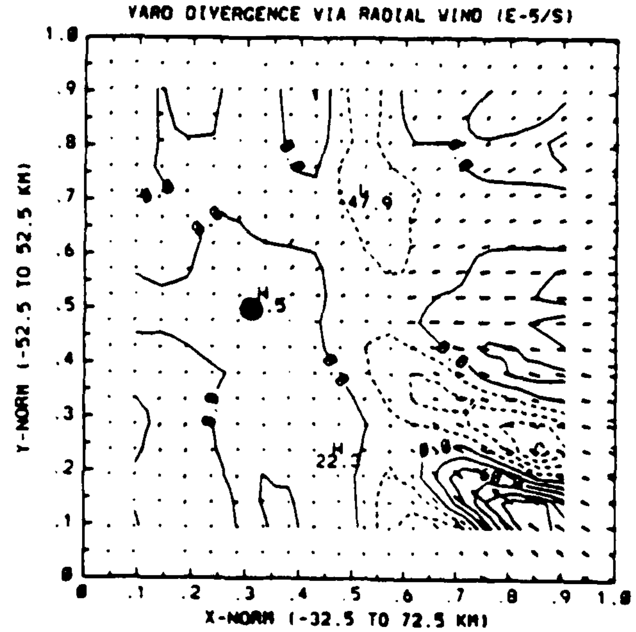

Figure 6.1f Divergence field as derived from radial wind vector field by method of Koscielny et al. (1982). Dot denotes radar location.

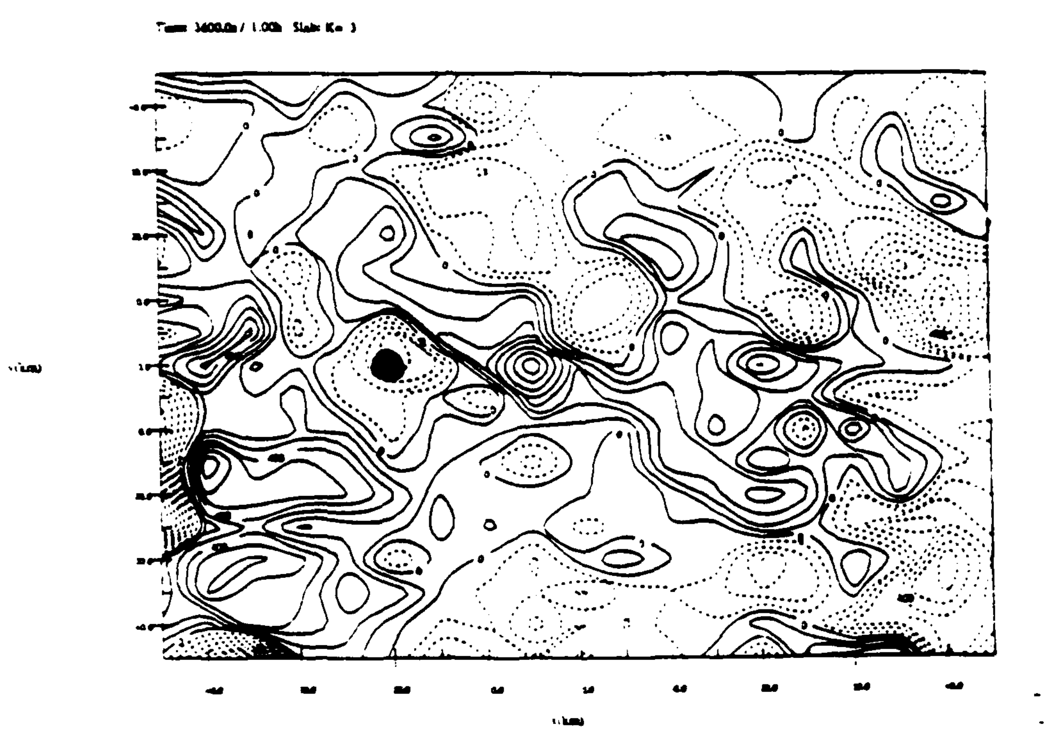

Figure 6.2a Vertical motion contours at 1 hour simulation time from CINDE case 1 at 1 km above the topography from the full model. The radar position in the computational domain in this and all subsequent figures is at (x,y) coordinate (-20.,0.), denoted by the large dot in this figure.

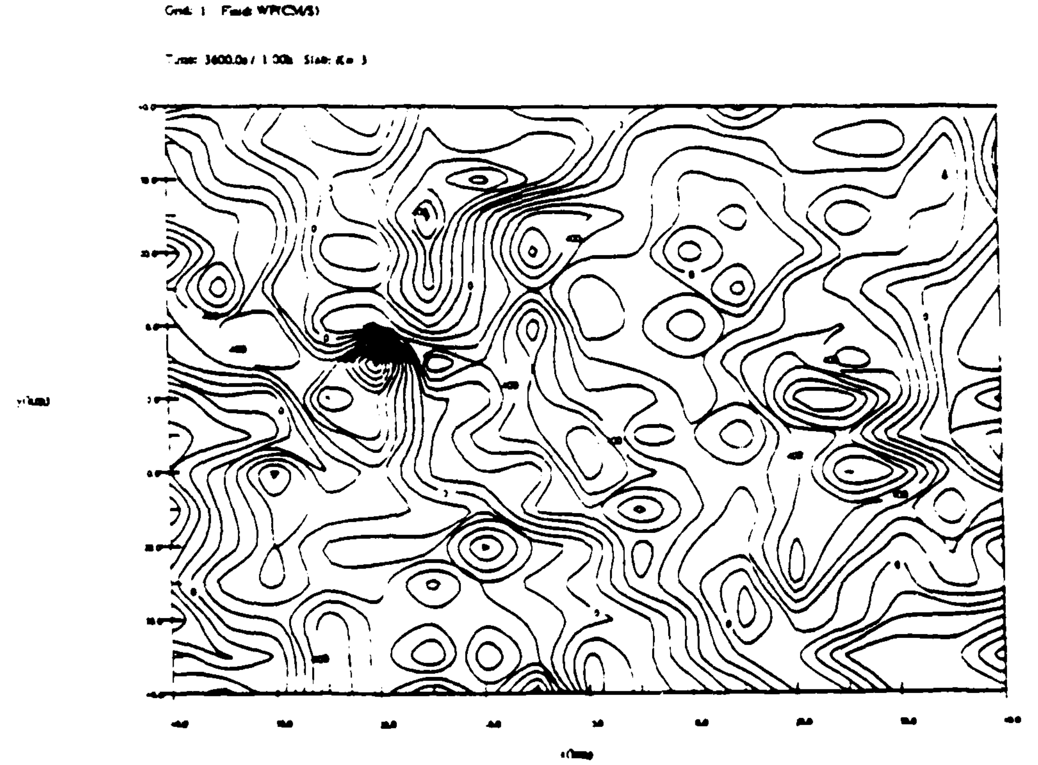

Figure 6.2b Vertical motion contours at 1 hour simulation time from CINDE case 1 at 1 km above the topography from the mixed layer model.

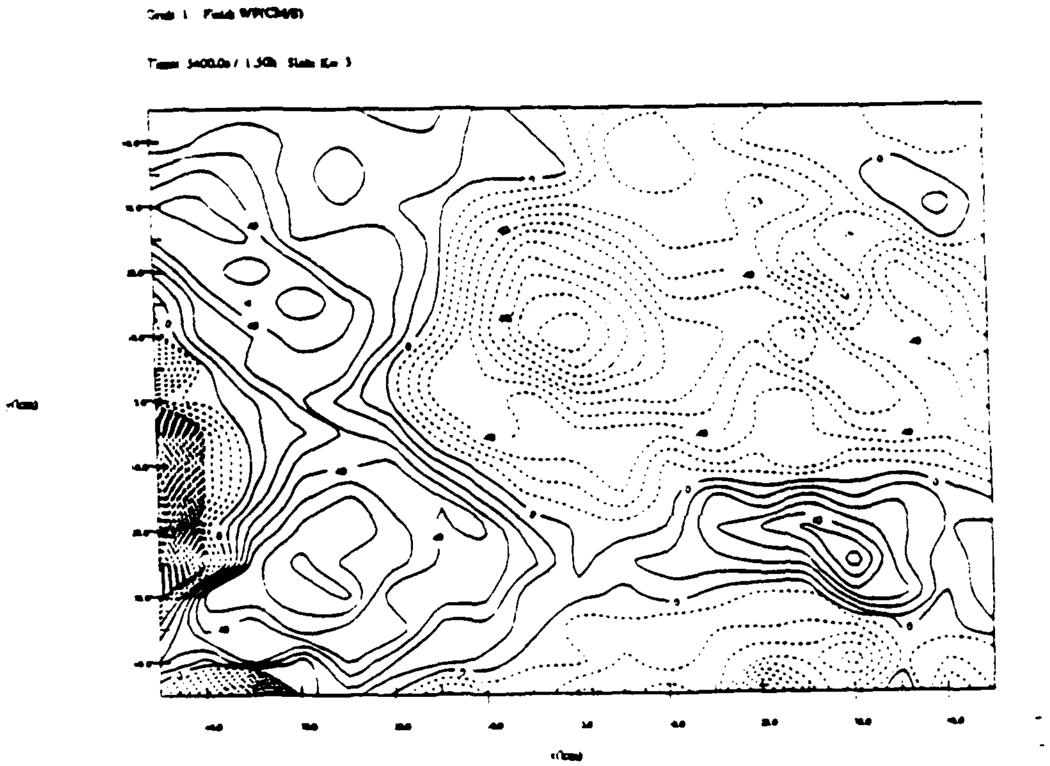

Figure 6.3a Same as figure 6.2a at 1.5 hours.

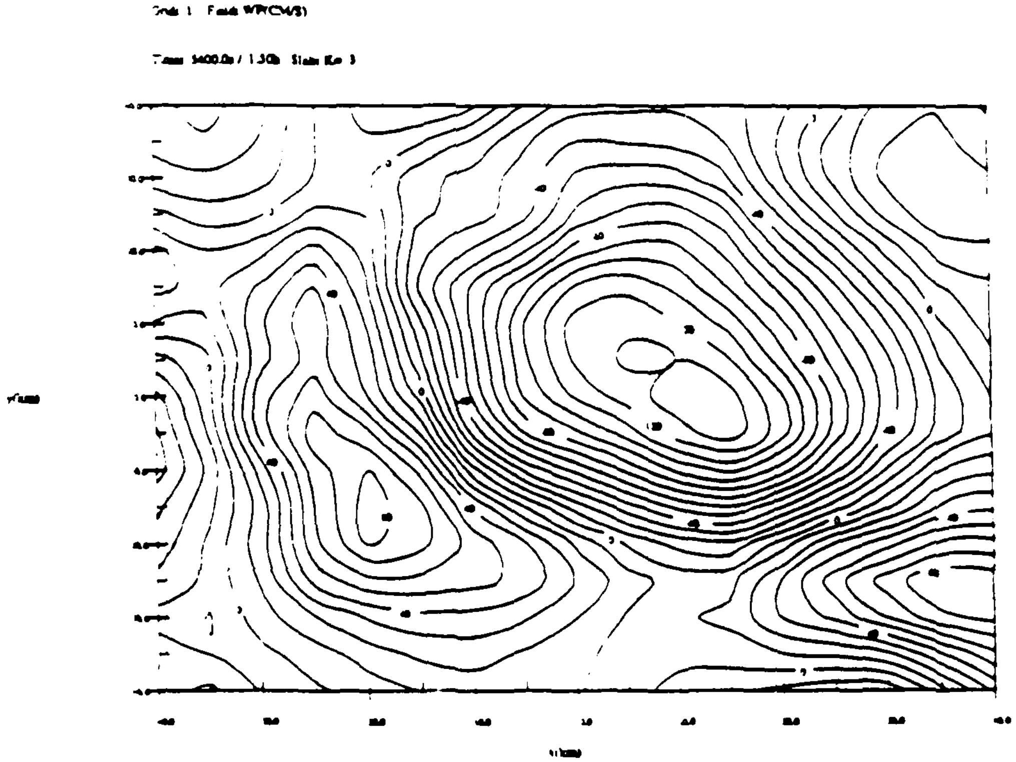

Figure 6.3b Same as figure 6.2b at 1.5 hours.

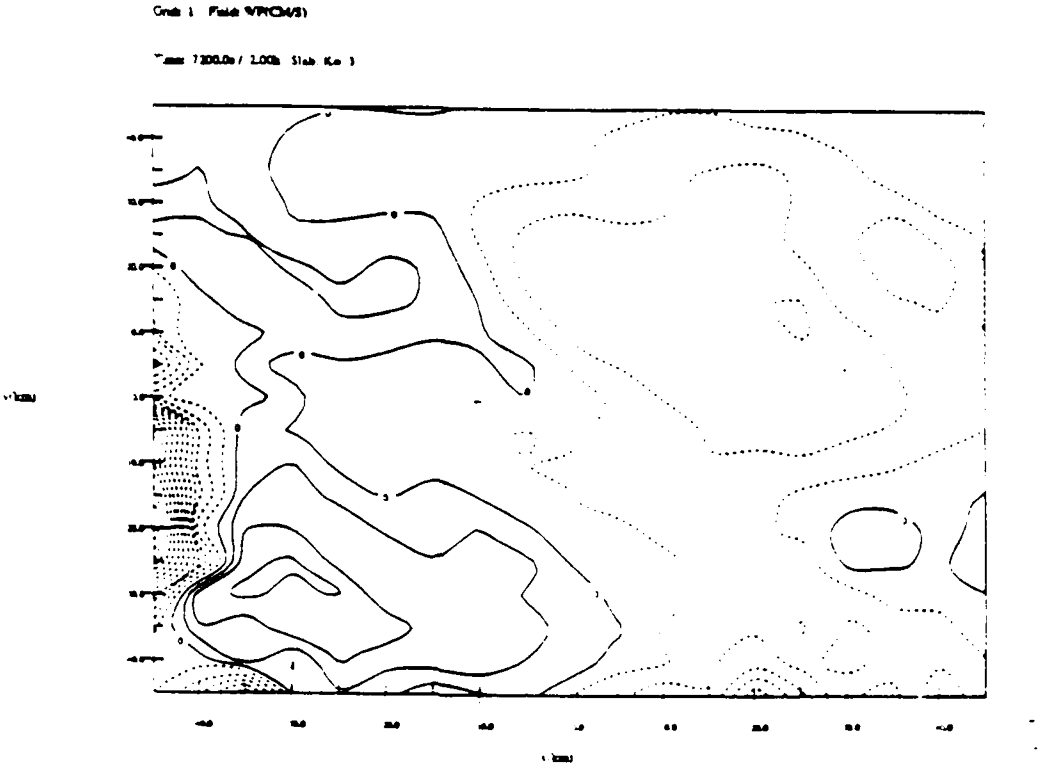

Figure 6.4a Same as figure 6.2a at 2.0 hours.

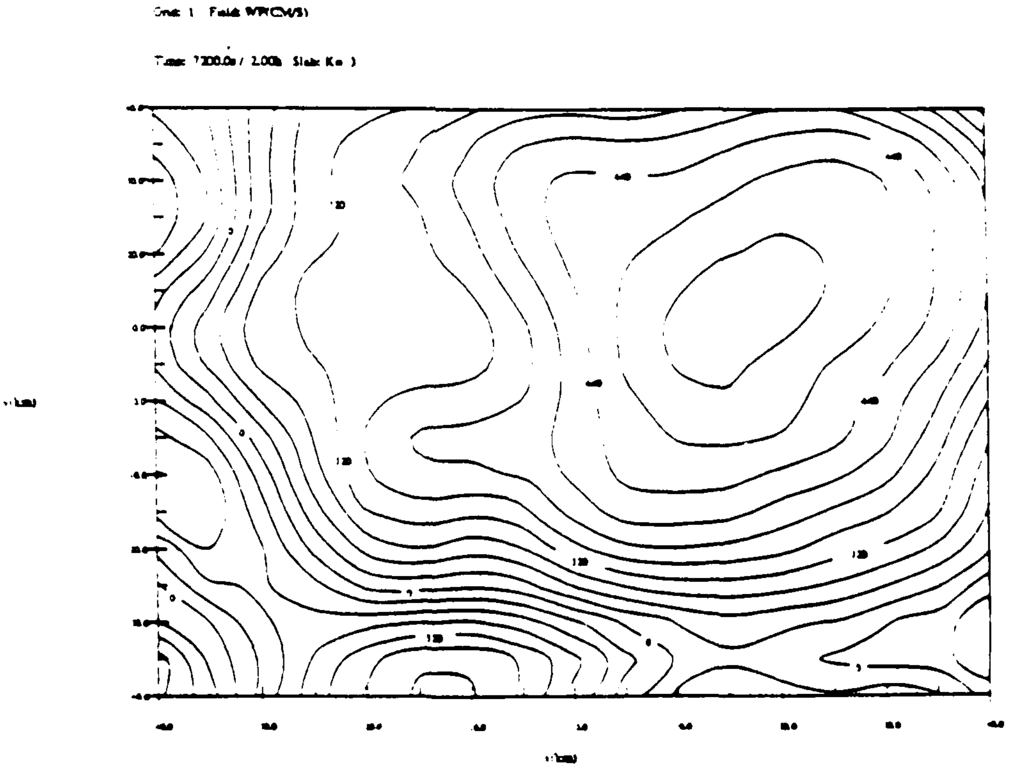

Figure 6.4b Same as figure 6.2b at 2.0 hours.

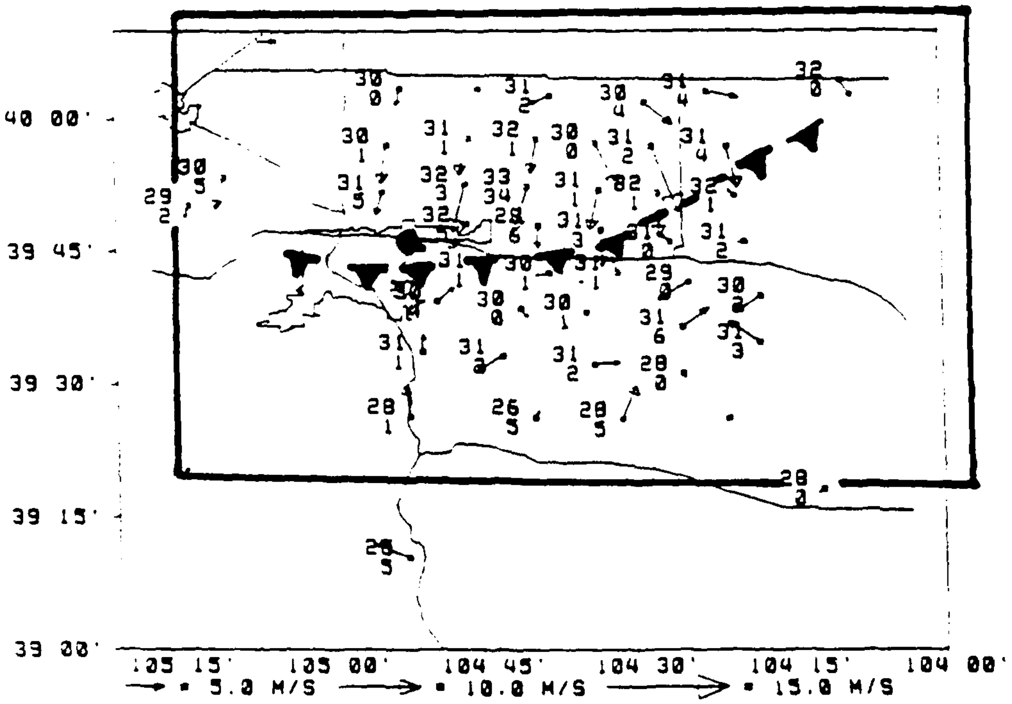

Figure 6.5a As in Figure 6.1a for case 2, at 1500 LT 27 June 1987. Outflow boundary from shower activity north of the domain is indicated.

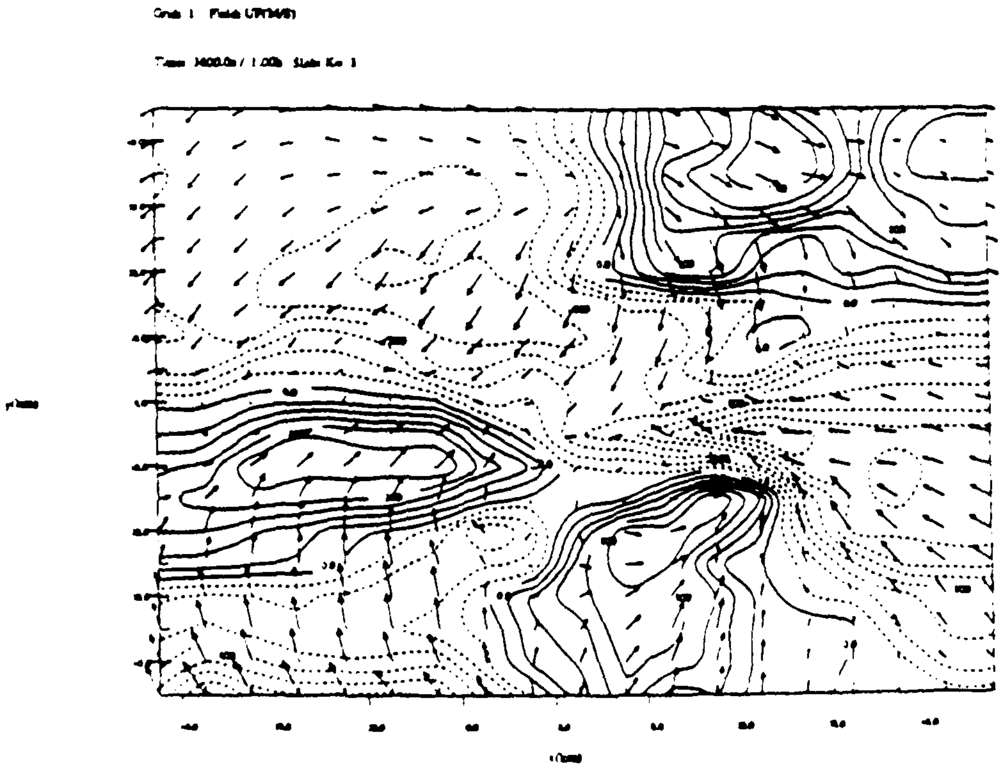

Figure 6.5b U component contours and velocity vectors at 1 hour simulation time from CINDE case 2 at 1 km above the topography from the full model.

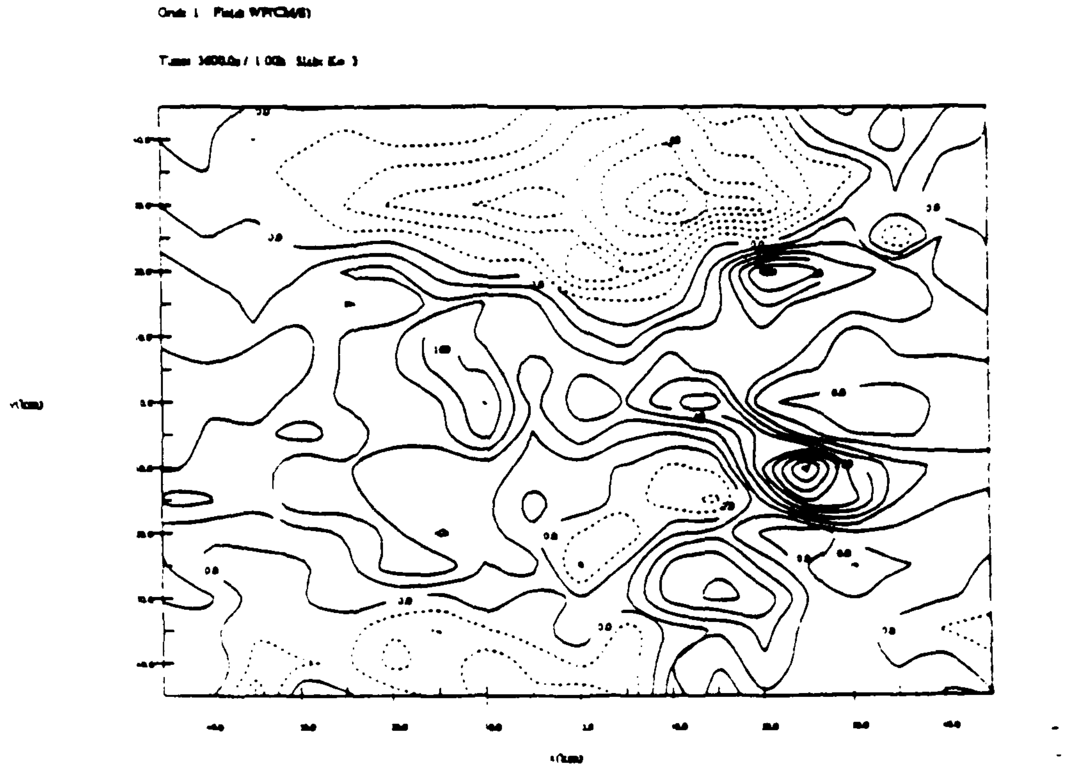

Figure 6.6a Vertical motion contours at 1 hour simulation time from CINDE case 2 at 1 km above the topography from the full model.

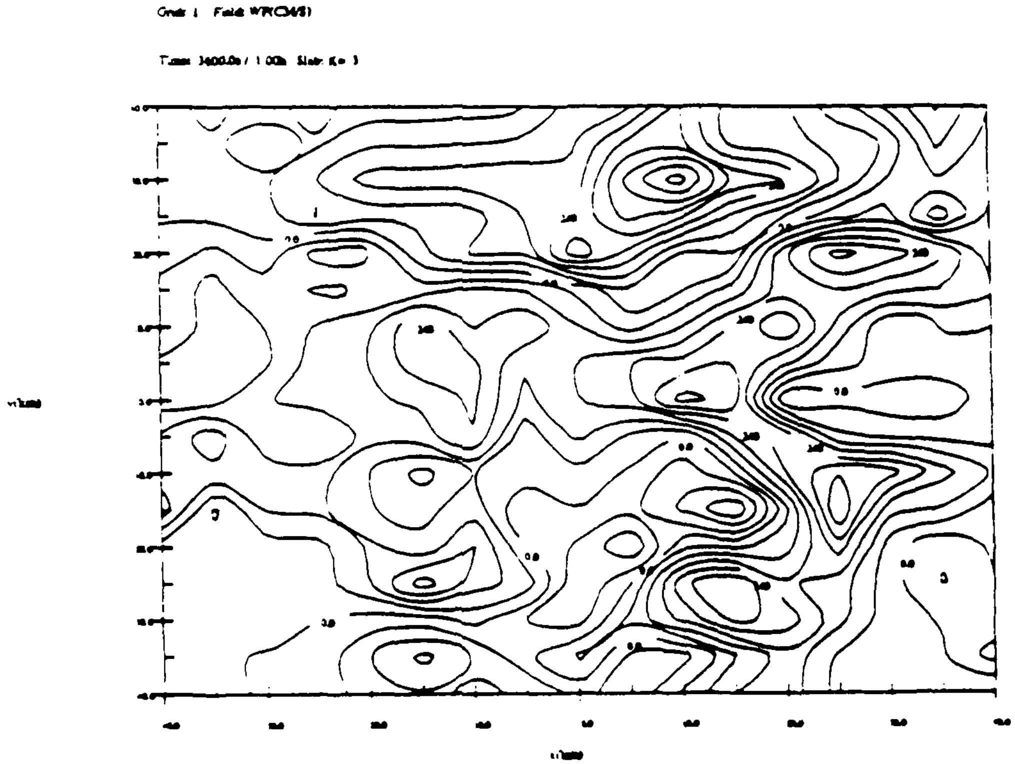

Figure 6.6b Vertical motion contours at 1 hour simulation time from CINDE case 2 at 1 km above the topography from the mixed layer model.

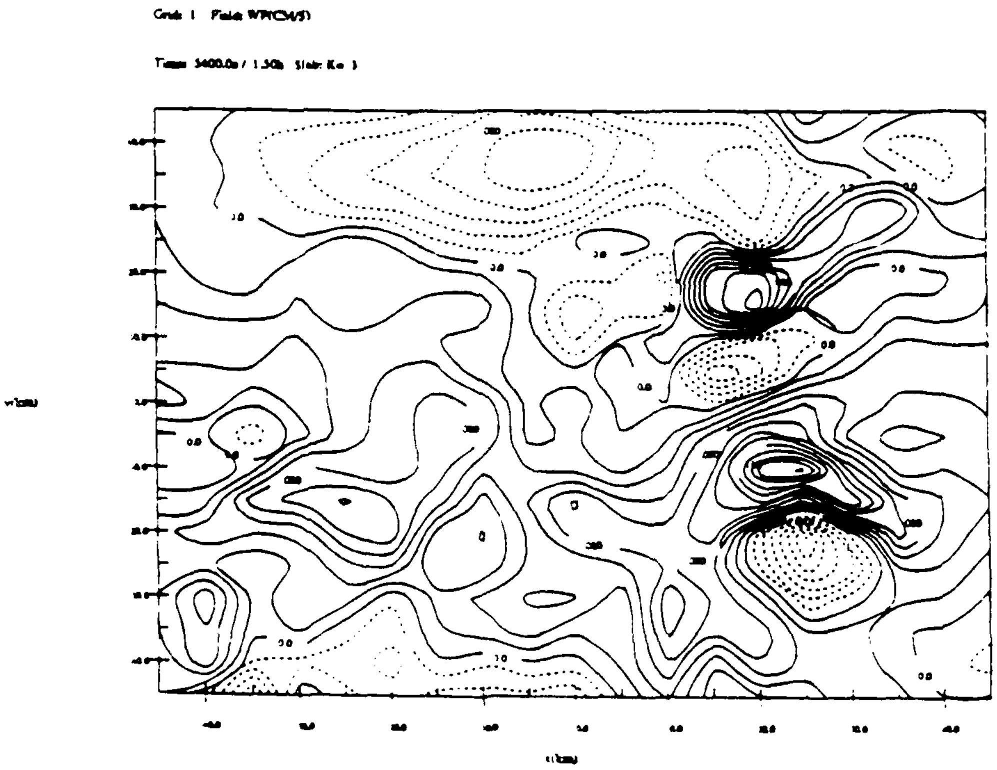

Figure 6.7a Same as figure 6.6a at 1.5 hours.

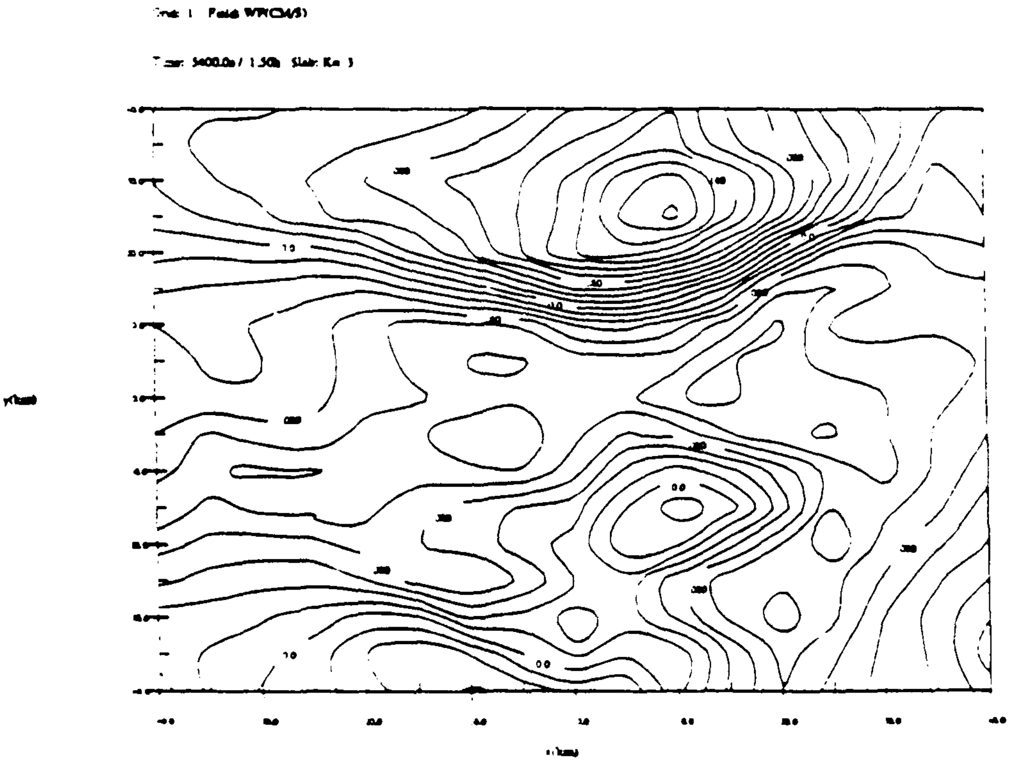

Figure 6.7b Same as figure 6.6b at 1.5 hours.

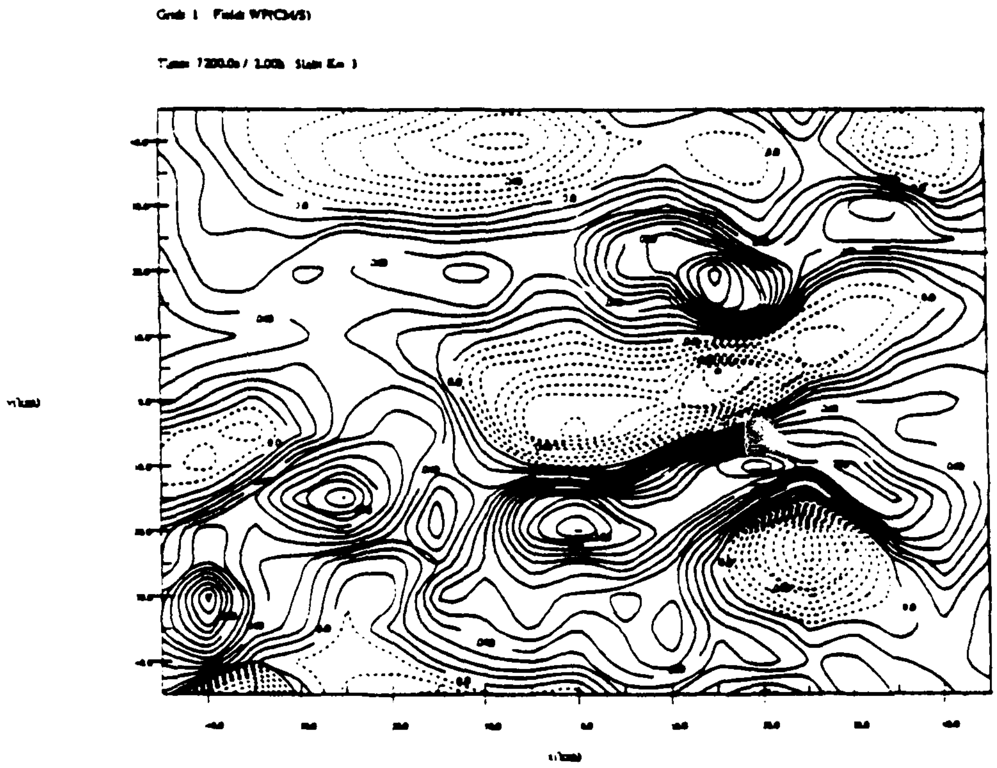

Figure 6.8a Same as figure 6.6a at 2.0 hours.

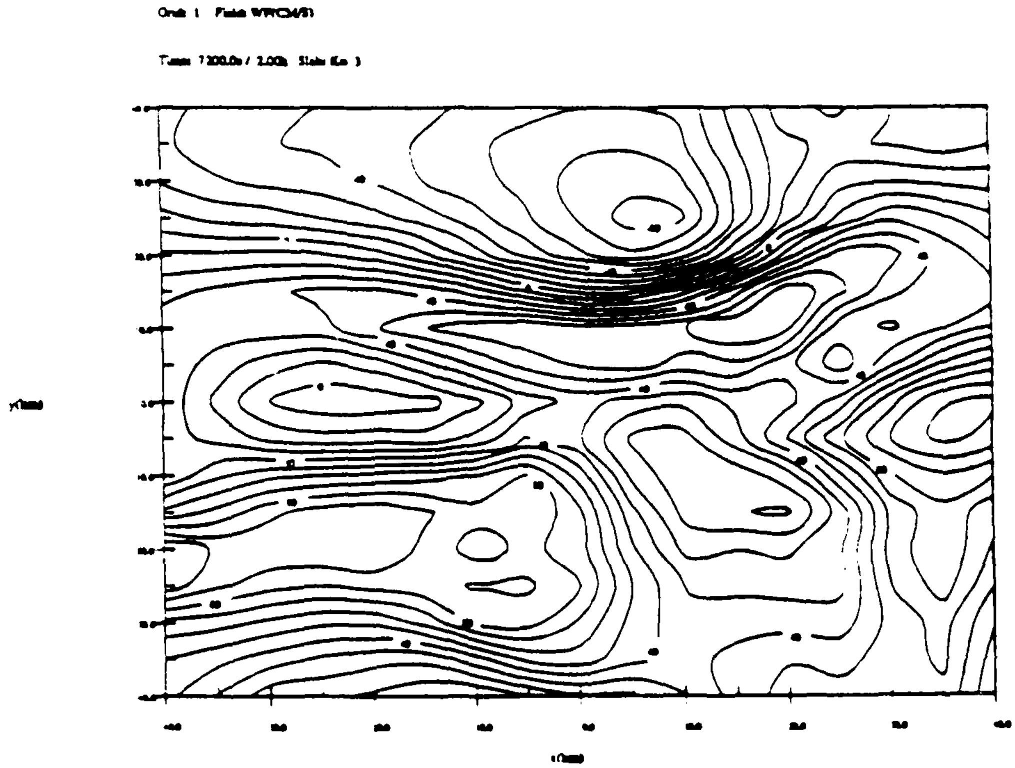

Figure 6.8b Same as figure 6.6b at 2.0 hours.

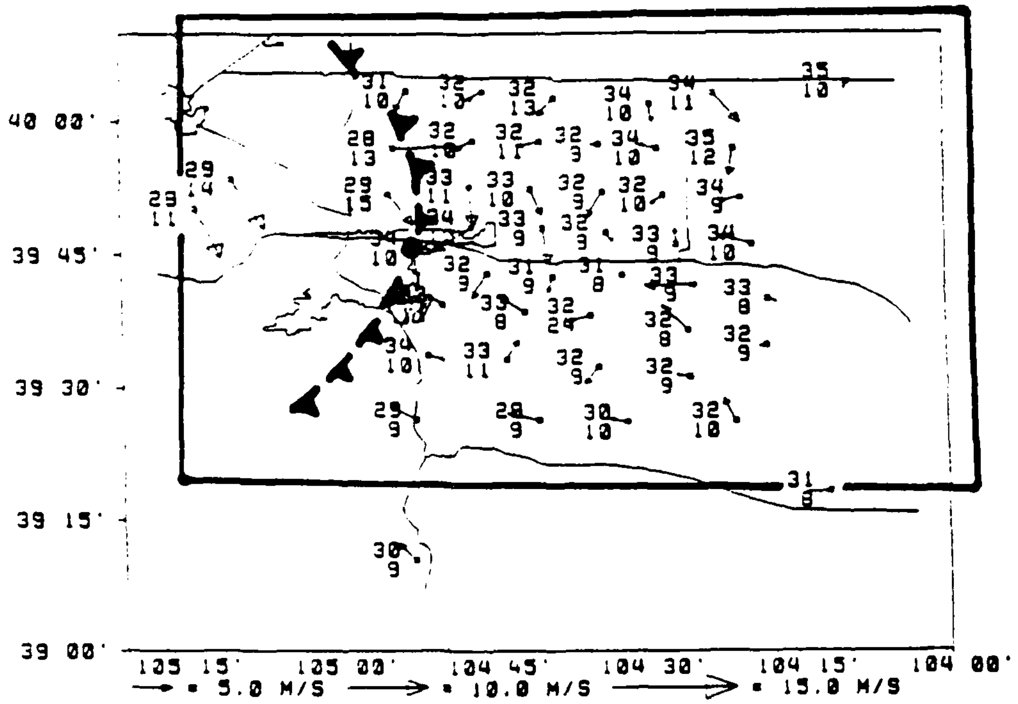

Figure 6.9a As in Figure 6.1a for case 3, at 1430 LT 31 July 1987. Outflow boundary from mountain shower activity west of the domain is indicated.

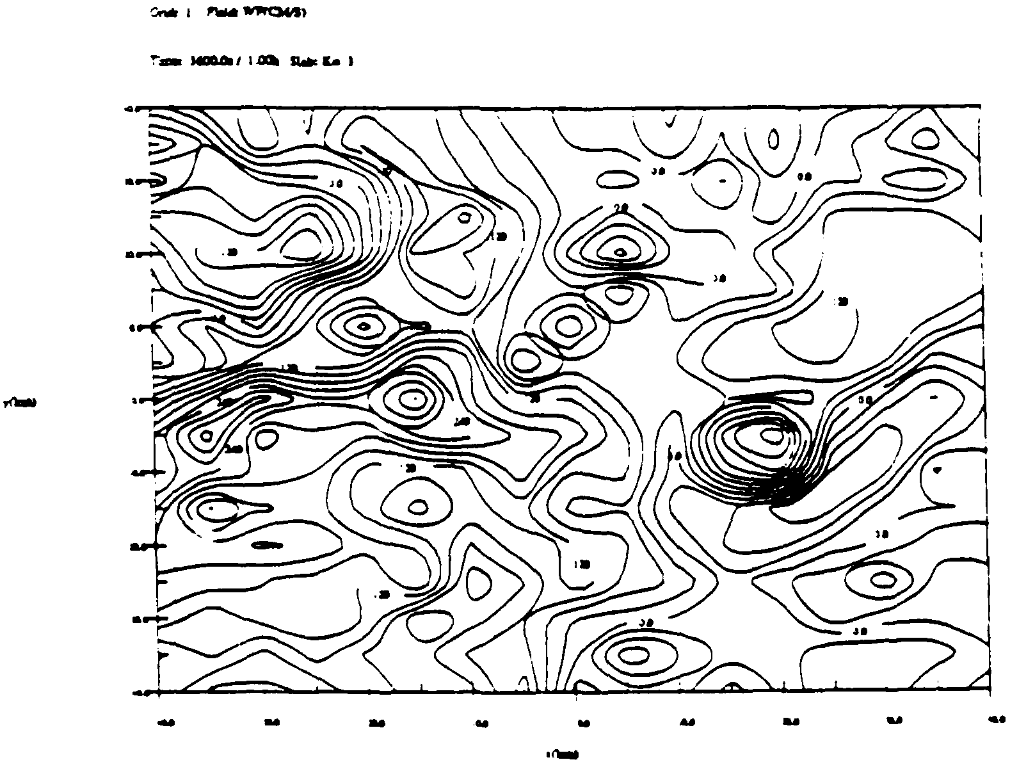

Figure 6.9b Vertical motion contours at 1 hour simulation time from CINDE case 3 at 1 km above the topography from the mixed layer model.

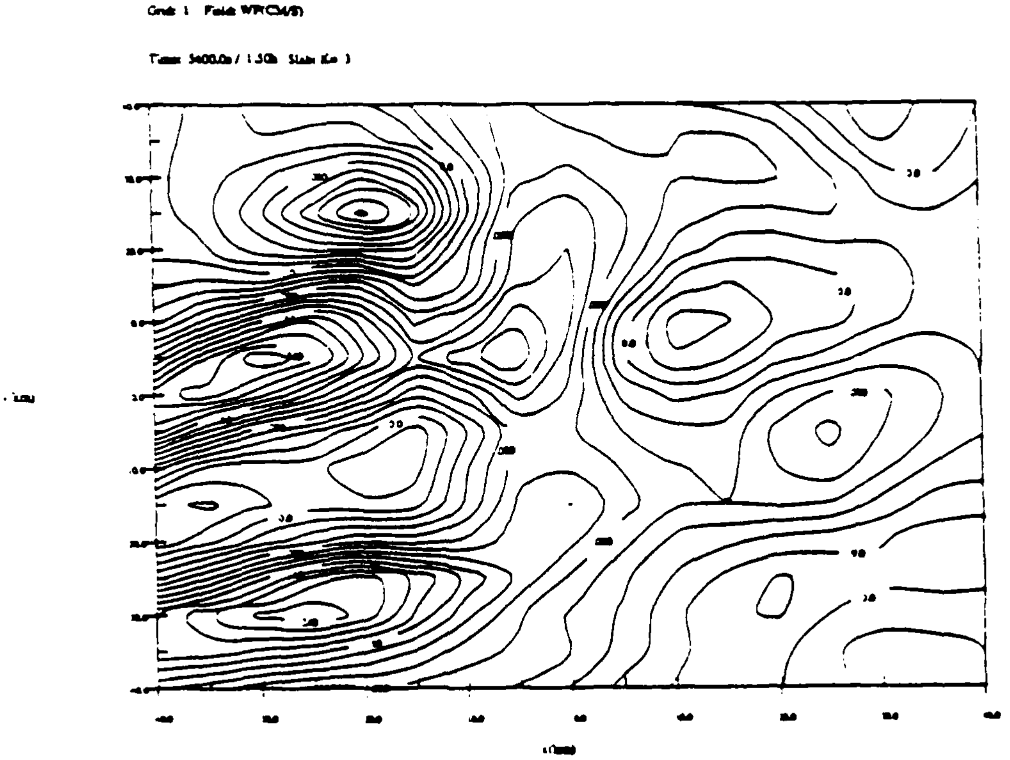

Figure 6.9c Same as Figure 6.9b at 1.5 hours.

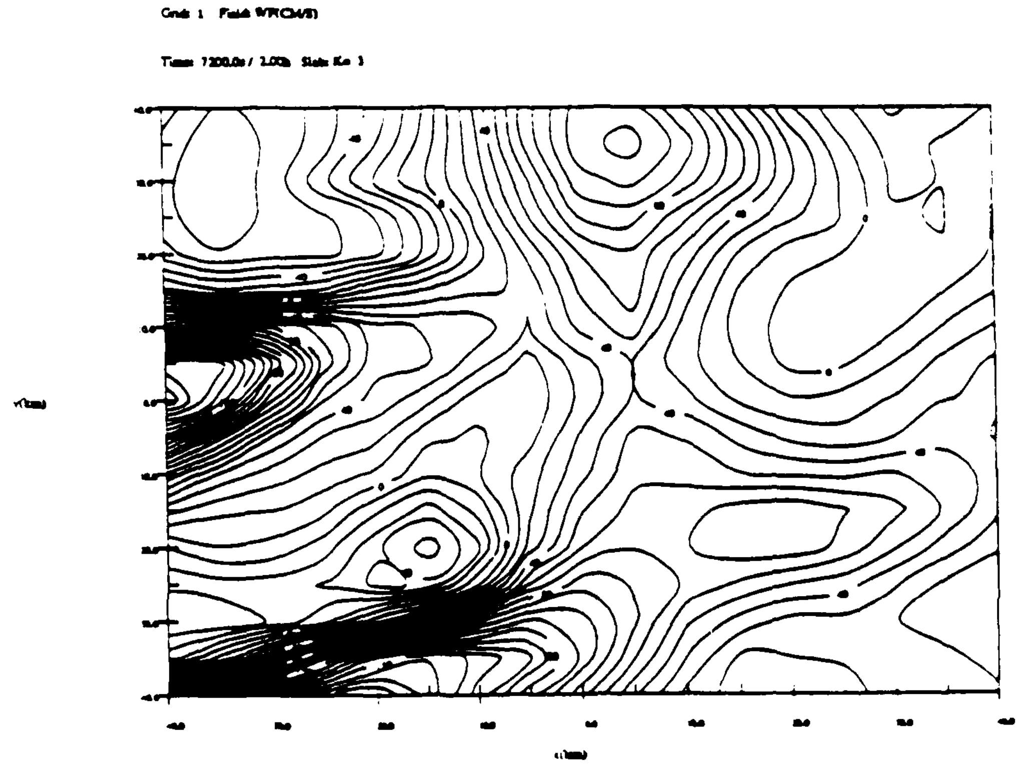

Figure 6.9d Same as Figure 6.9b at 2.0 hours.

Appendix A

THE CSU RAMS

INTRODUCTION

The numerical atmospheric models developed independently under the direction of William R. Cotton and Roger A. Pielke have recently been combined into the CSU Regional Atmospheric Modelling System (RAMS). Development of many of the physical modules has been accomplished over the past 15 years and has involved over 50 man years of effort. RAMS is a general and flexible modelling system rather than a single purpose model. For example, current research using RAMS includes atmospheric scales ranging from large eddy simulations ($\Delta \approx 100\ m$) to mesoscale simulations of convective systems ($\Delta x \approx 100 km$). This paper will discuss the options available in RAMS, the engineering aspects of the system and how the flexibility is attained.

RAMS OPTIONS

RAMS is a merging of basically three models that were designed to simulate different atmospheric circulations. These were a non-hydrostatic cloud model (Tripoli and Cotton, 1982) and two hydrostatic mesoscale models (Tremback *et al.*, 1985 and Mahrer and Pielke, 1977). The capability of RAMS was recently augmented with the implementation of 2-way interactive grid nesting. Because of this, the modelling system contains many options for various physical and numerical processes. These options are listed below.

The following options are currently available in configuring a model:

1. Basic equations:

   Option 1 Non-hydrostatic time-split compressible (Tripoli and Cotton, 1980)

   Option 2 Hydrostatic incompressible or compressible (Tremback *et al.*, 1985)

2. Dimensionality: 1, 2, or 3 spatial dimensions

3. Vertical coordinate:

   Option 1 Standard cartesian

   Option 2 Sigma-z

4. Horizontal coordinate:

   Option 1 Standard cartesian

   Option 2 Latitude/longitude

5. Grid Structure:

   - Arakawa-C grid stagger
   - Unlimited number of nested grids
   - Unlimited number of levels of nesting

6. Finite differencing:

Option 1 leapfrog on long timestep, forward-backward on small timestep, 2nd or 4th order flux conservative advection.

Option 2 forward-backward time split, 6th order flux conservative (Tremback *et al.*, 1987)

7. Turbulence closure:

Option 1 Smagorinsky-type eddy viscosity with R_i dependence

Option 2 Level 2.5 type closure using eddy viscosity as a function of a prognostic turbulent kinetic energy

Option 3 O'Brien profile function in a convective boundary layer (Mahrer and Pielke, 1977); local exchange coefficient in a stable boundary layer (McNider, 1981).

8. Condensation

Option 1 Grid points fully saturated or unsaturated

Option 2 No condensation

9. Cloud microphysics

Option 1 Warm rain conversion and accretion of cloud water (r_c) to raindrops (r_r), evaporation and sedimentation (Tripoli and Cotton, 1980)

Option 2 Option 1 plus specified nucleation of ice crystals (r_i), conversion nucleation and accretion of graupel (r_g), growth of ice crystals (r_i), evaporation, melting and sedimentation (see Cotton *et al.*, 1982)

Option 3 Option 1 plus option 2 plus predicted nucleation and sink of crystal concentration (N_i), conversion and growth of aggregates (r_a), melting, evaporation and sedimenation (see accompanying flow diagram, Figure 1). The nucleation model includes: sorption/deposition, contact nucleation by Brownian collision plus thermophoresis plus diffusiophoresis, secondary ice crystal production by rime-splinter mechanism.

Option 4 No precipitation processes

10. Radiation:

Option 1 Shortwave radiation model including molecular scattering, absorption of clear air (Yamamoto, 1962), ozone absorption (Lacis and Hansen, 1974) and reflectance, transmittance and absorptance of a cloud layer (Stephens, 1978), clear-cloudy mixed layer approach (Stephens, 1977)

Option 2 Shortwave radiation model described by Mahrer and Pielke (1977) which includes the effects of forward Rayleigh scattering (Atwater and Brown, 1974), absorption by water vapor (McDonald, 1960), and terrain slope (Kondrat'yev, 1969).

Option 3 Longwave radiation model including emissivity of a clear atmosphere (Rodgers, 1967), emissivity of cloud layer (Stephens, 1978). and emissivity of "clear and cloudy" mixed layer (Herman and Goody, 1976)

Option 4 Longwave radiation model described by Mahrer and Pielke (1977) including emissivities of water vapor (Jacobs *et al.*, 1974) and carbon dioxide (Kondrat'yev, 1969) and the computationally efficient technique of Sasamori (1972).

Option 5 No radiation

11. Transport and diffusion modules:

Option 1 Advection-diffusion model (Segal *et al.*, 1980) (To be implemented.)

Option 2 Semi-stochastic particle model for point and line sources of pollution (McNider, 1981) (To be implemented.)

12. Lower boundary:

Option 1 Specified surface temperature and moisture function or specified surface fluxes coupled with constant flux layer condition based on similarity theory (Manton and Cotton, 1977)

Option 2 Surface layer temperature and moisture fluxes are diagnosed as a function of the ground surface temperature derived from a surface energy balance (Mahrer and Pielke, 1977). The energy balance includes longwave and shortwave radiative fluxes, latent and sensible heat fluxes, and conduction from below the surface. To include the latter effect, a multi-level prognostic soil temperature model is computed.

Option 3 Modified form of Option 2 with prognostic surface equations (Tremback and Kessler, 1985)

Option 4 Same as Option 2, except vegetation parameterizations are included (McCumber and Pielke, 1981; 1984; McCumber, 1980) (To be implemented)

13. Upper boundary conditions:

Option 1 Rigid lid

Option 2 Rayleigh Friction layer plus Option 1-4

Option 3 Prognostic surface pressure (hydrostatic only)

Option 4 Material surface top. (hydrostatic only) (Mahrer and Pielke, 1977)

Option 5 Gravity wave radiation condition (Klemp and Durran, 1983)

14. Lateral boundary conditions:

Option 1 Klemp and Wilhelmson (1978) radiative boundary conditions

Option 2 Orlanski (1976) radiative boundary conditions

Option 3 Klemp and Lilly (1978) radiative boundary condition

Option 4 Option 1, 2 or 3 coupled with Mesoscale Compensation Region (MCR) described by Tripoli and Cotton (1982) with fixed conditions at MCR boundary (see Figure 2)

Option 5 The sponge boundary condition of Perkey and Kreitzberg (1976) when large scale data is available from objectively analyzed data fields or a larger scale model run. This condition includes a viscous region and the introduction of the large scale fields into the model computations near the lateral boundaries.

15. Initialization

    Option 1 Horizontally homogeneous.

    Option 2 Option 1 plus variations to force cloud initiation.

    Option 3 NMC data and/or soundings objectively analyzed on isentropic surface and interpolated to the model grid.

    Option 4 NMC data interpolated to the model grid.

As one can see, RAMS is quite a versatile modelling system. RAMS has been applied to the simulation of the following weather phenomena.

1. Towering cumuli and their modification
2. Mature tropical and mid-latitude cumulonimbi
3. Dry mountain slope and valley circulations
4. Orographic cloud formation
5. Marine stratocumulus clouds
6. Sea breeze circulations
7. Mountain wave flow
8. Large eddy simulation of power plant plume dispersal
9. Urban circulations
10. Lake effect storms
11. Tropical and mid-latitude convective systems

ENGINEERING ASPECTS

Because of the large number of options in RAMS, the structuring of the code needs to be carefully considered. This section will discuss various aspects of the code structure of the system.

Pre-processor The code of RAMS is written in as close to the FORTRAN 77 standard as possible. However, with a program as large as this, the FORTRAN standard is lacking in several features such as global PARAMETER and COMMON statements and conditional compilation. To remedy these insufficiencies, the RAMS code takes advantage of a pre-processor written as part of the RAMS package. This pre-processor itself is written in the 77 standard so that the package as a whole is highly portable. It takes full advantage of the character features of FORTRAN and has executed successfully on a number of machines including a VAX, CRAY-1, CRAY-X-MP, and CYBER 205 without modification. Some of the features of the pre-processor are described below:

1) By including a character in the first column of a line of code, that line can be "activated" or "eliminated" from the compile file. This allows for conditional compilation of single lines or entire sections of code.

2) A pre-processor variable can be set to a value. This variable can then be used in other expressions including a pre-processor IF or block IF to conditionally set other pre-processor variables. These variables also can be converted to FORTRAN PARAMETER statements which can be inserted anywhere in the rest of the code.

3) A group of statements can be delineated as a "global" which then can be inserted anywhere in the code. This is very useful for groups of COMMON and PARAMETER statements.

4) DO loops can be constructed in a DO/ENDDO syntax, eliminating the need for statement labels on the DO loops.

Two-way interactive grid nesting The use of grid nesting allows a wider range of motion scales to be modeled simultaneously and interactively. It can greatly ease the limitations of unnested simulations in which a compromise must be reached between covering an adequately large spatial domain and obtaining sufficient resolution of a particular local phenomenon. With nesting, RAMS can now feasibly model mesoscale circulations in a large domain where low resolution is adequate, and at the same time resolve the large eddy structure within a cumulus cloud in a subdomain of the simulation.

Nesting in RAMS is set up such that the same model code for each physical process such as advection is used for each grid. This makes it easy for any desired number of grids to be used without having to duplicate code for each one. Also, it is easy to add or remove a nested grid in time, and to change its size or location. There is still the flexibility of choosing many model options independently for different grids.

RAMS has adopted the two-way interactive nesting procedure described in Clark and Farley (1979). This algorithm is the means by which the different nested grids communicate with each other. The process of advancing coarse grid A and fine nested grid B forward in time one step begins with advancing grid A alone as if it contained no nest within. The computed fields from A are then interpolated tri-quadratically to the boundary points of B. The interior of B is then updated under the influence of its interpolated boundary values. Finally, the field values of A in the region where B exists are replaced by local averages from the fields of B. An increase in efficiency over the Clark and Farley method was implemented by allowing a coarse grid to be run at a longer timestep than a fine grid.

The following options are available with nesting in RAMS:

1) There is no imposed limit (only a practical one) to the number of nested grids which can be used.

2) When two grids B and C are nested within grid A, they may be either independent (occupying different space) or C may be nested within B.

3) The increase in spatial resolution of a nested grid may be any integer multiple of its parent grid resolution. Moreover, this multiple may be specified independently for the three coordinate directions.

4) A nested grid may, but need not, start from the ground and extend to the model domain top.

I/O structure For those machines with limited central memory and a "non-virtual" operating system or for efficiency on virtual systems, RAMS is constructed with a disk I/O scheme. When the scheme is operating, a subset of the model's three-dimensional variables will reside in central memory at any one time. Computations then can be performed with this subset. When these computations are finished, a new subset of three-dimensional variables are requested and computations performed with these. The RAMS structure, thus, is dependent on this I/O scheme and consists of a series of calls to the I/O scheme and to the routines which do the calculations.

Modularity For flexibility, RAMS is written as modular as possible. Each individual physical parameterization or numerical process is put in a separate subroutine so that the routines can easily be replaced for different options or with new developments.

Computational routines The routines that do the actual computations for the model are written so that the implementor of a new or replacement routine does not need to be concerned with most of the details of the rest of the model computations. All three-dimensional variables are "passed" to the subroutines through the call statement with other variables passed through COMMON. The implementor then has the flexibility to structure his routine in whatever manner he wishes to produce the desired result. This concept will also make the implementation of routines from other models and programs easier with less modification required.

Analyais rountines A set of subroutines has been developed for analyzing and plotting a variety of quantities from fields output from RAMS. This greatly facilitiates the interpretation and understanding of modeled atmospheric phenomena. The quantities diagnosed by these routines include vorticity, divergence, streamfunction, energy, momentum flux, most variances and covariances, and layer averaged quantities.

REFERENCES

Atwater, M.A. and P.S. Brown, Jr., 1974: Numerical calculation of the latitudinal variation of solar radiation for an atmosphere of varying opacity. *J. Appl. Meteor.*, **13**, 289-297.

Cotton, W.R., M.A. Stephens, T. Nehrkorn, and G.J. Tripoli, 1982: The Colorado State University three-dimensional cloud/mesoscale model - 1982. Part II: An ice phase parameterization. *J. de Rech. Atmos.*, **16**, 295-320.

Herman, G. and R. Goody, 1976: Formation and persistence of summertime arctic stratus clouds. *J. Atmos. Sci.*, **33**, 1537-1553.

Jacobs,C.A., J.P. Pandolfo and M.A. Atwater, 1974: A description of a general three dimensional numerical simulation model of a coupled air-water and/or air-land boundary layer. IFYGL final report, CEM Report No. 5131-509a.

Klemp, J.B. and D.R. Durran, 1983: An upper boundary condition permitting internal gravity wave radiation in numerical mesoscale models. *Mon. Wea. Rev.*, **111**, 430-444.

Klemp, J.B. and R.B. Wilhelmson, 1978a: The simulation of three-dimensional convective storm dynamics. *J. Atmos. Sci.*, **35**, 1070-1096.

Klemp, J.B. and R.B. Wilhelmson, 1978b: Simulations of right- and left-moving storms produced through storm splitting. *J. Atmos. Sci.*, **35**, 1097-1110.

Klemp, J.B. and D.K. Lilly, 1978: Numerical simulation of hydrostatic mountain waves. *J. Atmos. Sci.*, **35**, 78-107.

Kondrat'yev, J., 1969: *Radiation in the Atmosphere.* Academic Press, New York, 912 pp.

Lacis, A.A., and J. Hansen, 1974: A parameterization for the absorption of solar radiation in earth's atmosphere. *J. Atmos. Sci.*, **31**, 118-133.

Mahrer, Y. and R.A. Pielke, 1977: A numerical study of the airflow over irregular terrain. *Beitrage zur Physik der Atmosphare*, **50**, 98-113.

Manton, M.J., and W.R. Cotton, 1977: Parameterization of the atmospheric surface layer. *J. Atmos. Sci.*, **34**, 331-334.

McCumber, M.D., 1980: A numerical simulation of the influence of heat and moisture fluxes upon mesoscale circulation. Ph.D. dissertation, Dept. of Environmental Science, University of Virginia.

McCumber, M.C. and R.A. Pielke, 1981: Simulation of the effects of surface fluxes of heat and moisture in a mesoscale numerical model. Part I: Soil layer. *J. Geophys. Res.*, **86**, 9929-9938.

McCumber, M.C. and R.A. Pielke, 1983: Simulation of the Effects of Surface Fluxes of Heat and Moisture in a Mesoscale Numerical Model. Part 2: Vegetation. *J. Geophys. Res.*(submitted).

McDonald, J.E., 1960: Direct absorption of solar radiation by atmospheric water vapor. *J. Meteor.*, **17**, 319-328.

McNider, R.T., 1981: Investigation of the impact of topographic circulations on the transport and dispersion of air pollutants. Ph.D. dissertation, University of Virginia, Charlottesville, VA 22903.

Orlanski, I., 1976: A simple boundary condition for unbounded hyperbolic flows. *J. Comput. Phys.*, **21**, 251-269.

Perkey, D.J. and C.W. Kreitzberg, 1976: A time-dependent lateral boundary scheme for limited-area primitive equation models. *Mon. Wea. Rev.*, **104**, 744-755.

Rodgers, C.D., 1967: The use of emissiv.cy in atmospheric radiation calculations. *Quart. J. Roy. Meteor. Soc.*, **93**, 43-54.

Sasamori, T., 1972: A linear harmonic analysis of atmospheric motion with radiative dissipation. *J. Meteor. Soc. of Japan*, **50**, 505-518.

Stephens, G.L., 1977: The transfer or radiation in cloudy atmosphere. Ph.D. Thesis. Meteorology Department, University of Melbourne.

Stephens, G.L., 1978a: Radiation profiles in extended water clouds. Webster Theory. *J. Atmos. Sci.*, **35**, 2111-2122.

Tremback, C.J. and R. Kessler, 1985: A surface temperature and moisture parameterization for use in mesoscale numerical models. Preprints, 7th Conference on Numerical Weather Prediction, 17-20 June 1985, Montreal, Canada, AMS.

Tremback, C.J., J. Powell, W.R. Cotton, and R.A. Pielke, 1987: The forward in time upstream advection scheme: Extension to higher orders. *Mon. Wea. Rev.*, **115**, 540-555.

Tremback, C.J., G.J. Tripoli, and W.R. Cotton, 1985: A regional scale atmospheric numerical model including explicit moist physics and a hydrostatic time-split scheme. Preprints, 7th Conference on Numerical Weather Prediction, June 17-20, 1985, Montreal, Quebec, AMS.

Tripoli, G.J. and W.R. Cotton, 1980: A numerical investigation of several factors contributing to the observed variable intensity of deep convection over South Florida. *J. Appl. Meteor.*, **19**, 1037-1063.

Tripoli, G.J., and W.R. Cotton, 1982: The Colorado State University three-dimensional cloud/mesoscale model - 1982. Part I: General theoretical framework and sensitivity experiments. *J. de Rech. Atmos.*, **16**, 185-220.

Yamamoto, G., 1962: Direct absorption of solar radiation by atmospheric water vapor carbon dioxide and molecular oxygen. *J. Atmos. Sci.*, **19**, 182-188.

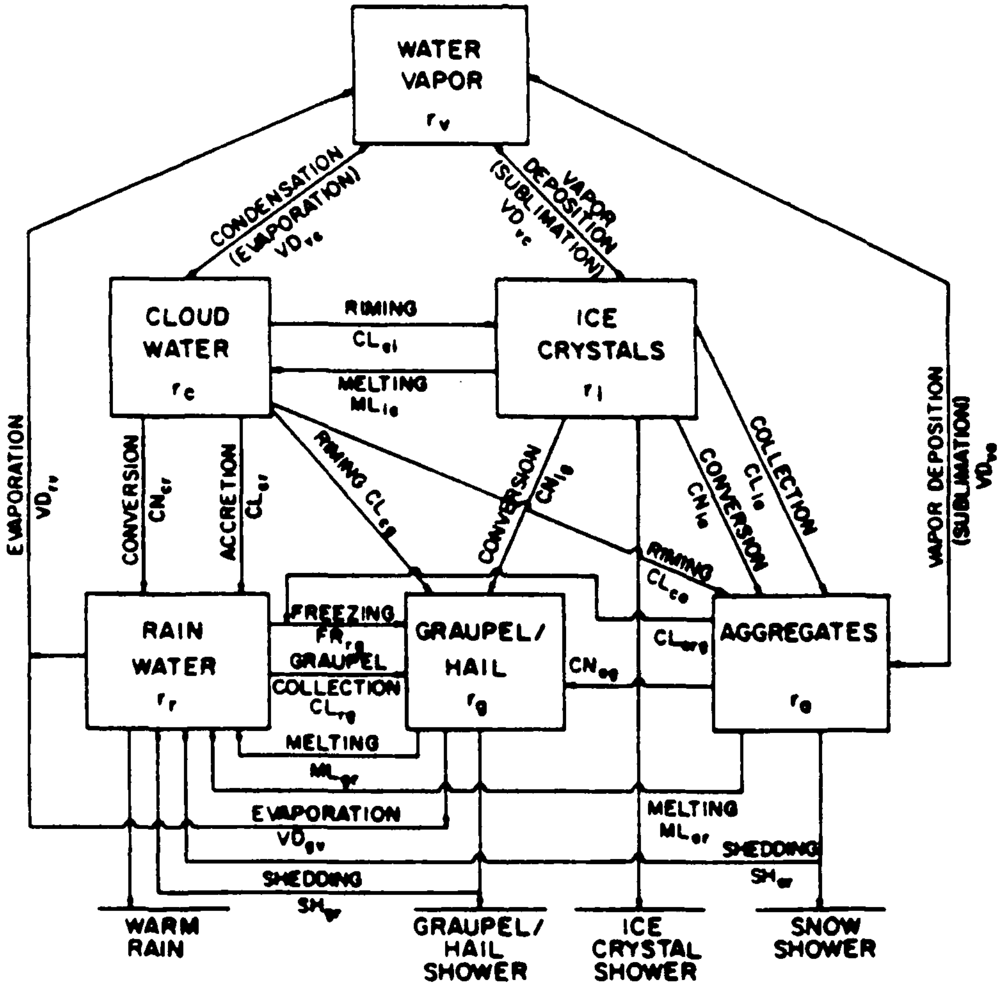

Figure 1: Flow diagram.

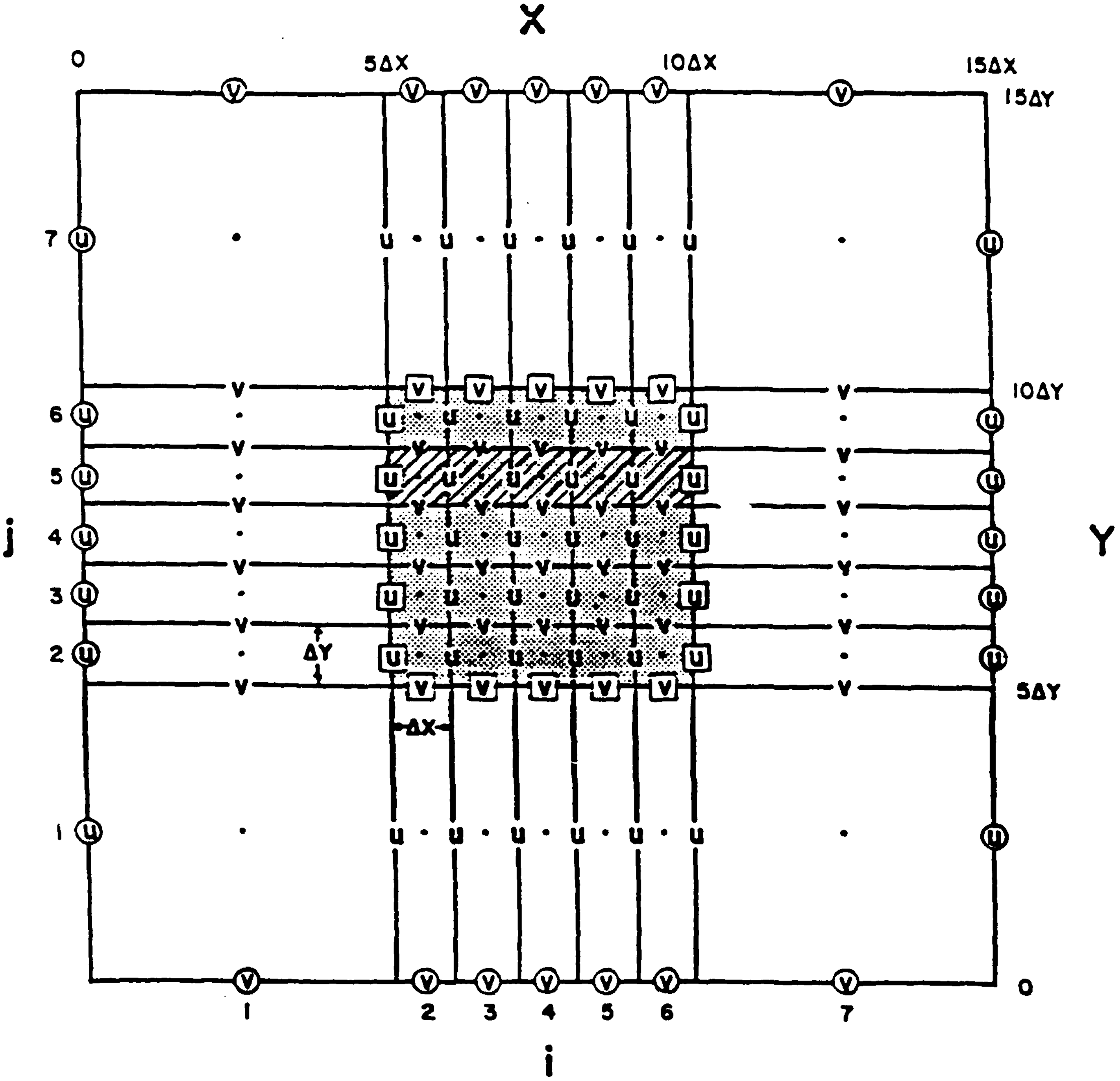

Figure 2: M .scale Compensation Region

Appendix B

Preprints, 24th Conference on Radar Meteorology, 27-31 March 1989, Tallahassee, FL.

Assimilation of Doppler Radar Wind Data into a Numerical Prediction Model: A Demonstration of Certain Hazards

R.L. Walko*, C.J. Tremback*, W.R. Cotton*
ASTeR, Inc.
P.O. Box 466
Ft Collins, CO 80523

1 Introduction

Four-dimensional assimilation of observational data into a numerical atmospheric prediction model over a period prior to the start of the pure prediction (during which the model receives no assistance from observations) is an alternative to a single *3D* assimilation at the startup time of the pure prediction. In *4D* assimilation, the model solution is weighted between the state predicted by its equations and the state defined by the assimilated data so that some information from earlier data inputs is preserved. One means for doing this is to "nudge" the model toward the input data by means of a forcing term whose strength is proportional to the input data minus the current model state. The success of *4D* assimilation depends in part on the ability of the model fields to properly adjust to the new information. The assimilated data does not necessarily represent a state of balance either with itself or with the current model solution. This is particularly true if the available data is incomplete in the sense that it contains only some of the total number of dynamic and thermodynamic fields which are intimately coupled. For example, there are currently widespread plans to assimilate wind information from NEXRAD radars and wind profilers into operational forecast models without simultaneously providing direct observational data on temperature or pressure. It is shown in the present study that this can have a very detrimental effect on model solutions. Two simulations are run in which the horizontal winds in the lowest kilometer are assumed completely known in real time by means of remote sensing and any required data processing scheme. The horizontal low level winds in the numerical model are nudged toward the observed wind field to attempt to bring the model state into closer agreement with the atmosphere. Any additional information on the atmosphere other than the initial sounding is assumed unavailable to the model.

2 Numerical Experiments

The framework for combining assimilated wind data with numerical integrations of the governing equations is the Colorado State University Regional Atmospheric Modeling System (RAMS). It is run in its nonhydrostatic mode with 20 nonuniformly-spaced vertical levels extending to a height of $12km$. All simulations are conceived as having slab symmetry in one horizontal direction, so the model is run as a *2D* domain spanning $120km$ in the other horizontal direction with $3km$ resolution. We choose the following simple physical scenario to illustrate the main point of this paper. A sounding representing a horizontally homogeneous, motionless, and statically stable state throughout the experimental domain is used to initialize the model. At some point after the initialization, a cold front or gust front moves into the domain and is detected by Doppler radar which is fully scanning the lowest kilometer of the atmosphere. The front is observed as a $6km$ wide convergence line advancing at $4ms^{-1}$ into the still air and being trailed by $8ms^{-1}$ winds blowing into the front. However, no information on the thermal structure of the front is available to the model. The model winds are nudged toward the observed field with an e-folding time of $1800s$.

Figure 1 illustrates the perturbation pressure field and the wind vectors in the plane of the model domain five minutes after the nudging has begun. At so early a time, the model winds have responded directly to the nudging, all other forces including pressure being much weaker, and a narrow convergence line begins to form as observed. Following a persistent two-hour application of the nudging, however, the structure of the model winds (shown in fig. 2) has deviated substantially from the observed structure of the front. Instead of

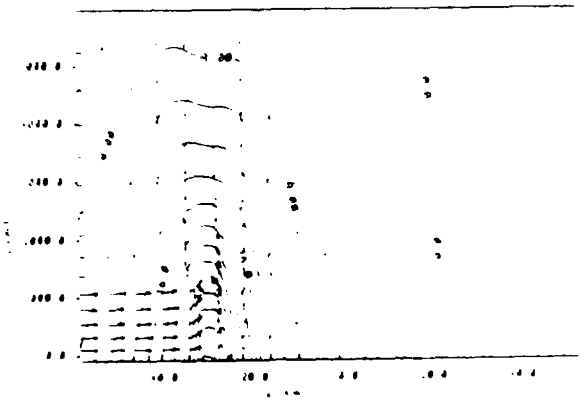

Fig. 1. Vector plot of the *2D* velocity field (peak horizontal magnitude is $1.1ms^{-1}$) and contour plot of the perturbation pressure field (in Pascals) for the stable case five minutes after nudging begins.

---

*Full time affiliation with Colorado State University

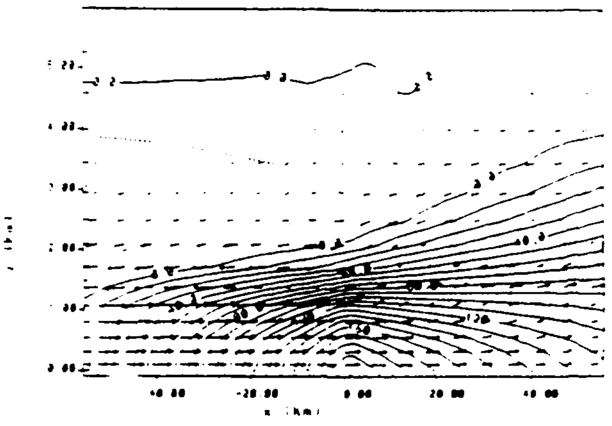

Fig. 2. Same as fig. 1 but two hours after nudging has begun. Peak horizontal velocity is $5.4ms^{-1}$.

a convergence line having a perpendicular wind component varying $8ms^{-1}$ over its $6km$ width, only a very weak and broad zone of convergence with winds varying only $2ms^{-1}$ over a $100km$ width is present. The reason for this is that the nudging force has been almost completely opposed by a horizontal pressure gradient force, which is apparent in fig. 2. The surface high pressure is maintained quasihydrostatically in the vertical by a dome of cold air (fig. 3) formed by upward motion of stable air over the convergence zone. The high pressure is of course not realistic for a frontal boundary. In summary, the modeled atmospheric response to the nudging of the velocity field was to counteract it. Had the assimilated data also contained the information that the air behind the front was significantly colder than the air ahead of it, the resulting direct nudging of the model temperature field would have allowed the modeled front to properly develop its convergence line structure.

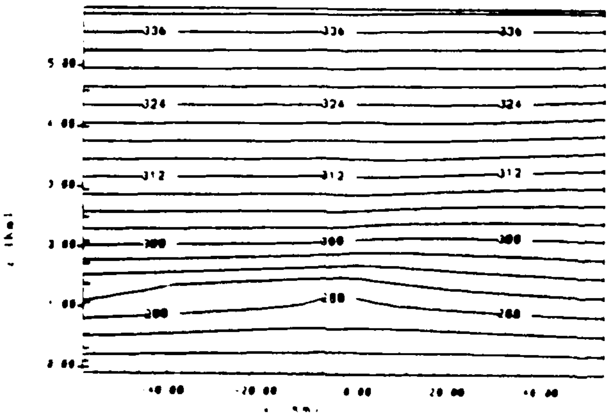

Fig. 3. Plot of the potential temperature field coinciding with the fields of fig. 2.

To further illustrate the problem caused by assimilating velocity data but not temperature information, we cease the velocity assimilation immediately following the two-hour period, as if the pure model forecast period is to begin then, and continue the model integration with no further nudging. Figure 4 shows the solution one half hour later. What had been a convergence zone (and still should be according to atmospheric observations) is now a region of divergence because the cold dome formerly built up and maintained by the nudging forces is in the process of collapsing. This solution is obviously grossly out of agreement with the continuing frontal passage that it should represent.

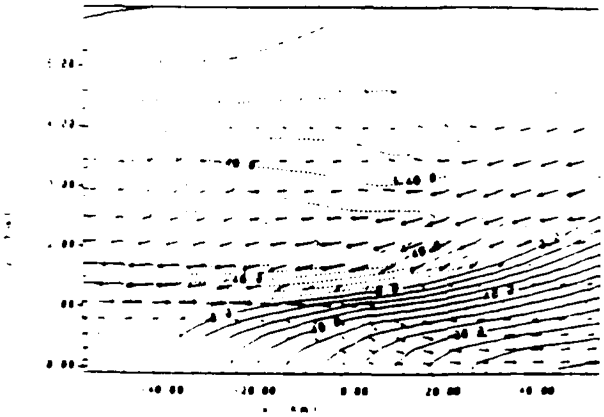

Fig. 4. Same as fig. 2 but one half hour later, nudging having been turned off during that half hour. Peak horizontal velocity is $-5.0ms^{-1}$.

The underlying fault of the above assimilation experiment is that only partial observational information was provided on an entire coupled system. In the example, the velocity and temperature fields are coupled because the atmosphere is stably stratified. In a nearly neutral atmosphere, the temperature field is much less relevant to the velocity field, and the velocity information supplied is alone sufficient to provide a good solution by nudging. This is demonstrated by a second experiment, identical to the first except that the lowest $3km$ of the atmosphere are very close to neutral instead of nearly isothermal. Figure 5 shows the velocity field after two hours of nudging to have a sharp convergence line as observed. Since the upward motion and compensating divergence above can all occur within the deep neutral layer, no significant perturbations of the temperature field are generated, and hence no large fluctuations in the pressure field result. We again turn off the nudging as in the first experiment, and show the velocity fields one half hour later (fig. 6). Although the convergence line has weakened somewhat, it is still convergent. Thus, in this neutral case, nudging has proved a benefit to the model solution.

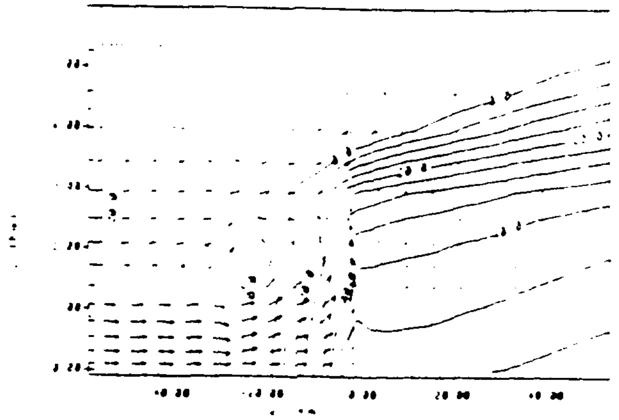

Fig. 5. Same as fig. 2 but for the neutral case. Peak horizontal velocity is $7.2 m s^{-1}$.

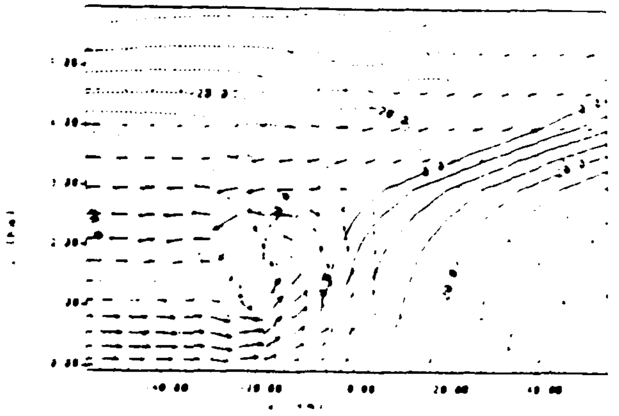

Fig. 6. Same as fig. 4 but for the neutral case. Peak horizontal velocity is $6.4 m s^{-1}$.

3 Summary and Discussion

This study has illustrated an example in which 4*D* data assimilation into a numerical prediction model produces erroneous results because the data does not contain complete, balanced information. In this case, velocity information is available but temperature information is not. From the information given, the only rational means for forcing the modeled velocity field to the observed convergence field is mechanically rather than thermally. Under the given stable atmospheric conditions, this produces an anomalous cold dome and surface high pressure at the convergence line rather than the typical frontal structure assumed to accompany the convergence line.

It is interesting to consider a different scenario which can likewise generate surface convergence. If, for example, the convergence had not been caused by baroclinity at the surface, but instead mechanically by cyclonic vorticity advection aloft, the formation of the cold dome over the convergence would have been realistic, although the surface high would not. One might also consider the result of nudging the temperature field in the model to assimilated data through a pseudo heating or cooling term, without any velocity observations being available. If a region of the model were heated to bring it closer to the observed temperature of a warm atmospheric region, and that atmospheric region had been diabatically heated by for example latent heat release, radiation, or surface heat flux, both the model and the atmosphere would tend to produce upward motion in the heated region and agreement would be good. If, on the other hand, the observed warm region of the atmosphere had instead been heated adiabatically by mechanically-forced subsidence (*e.g.* due to anticyclonic vorticity advection aloft), poor agreement between the atmosphere and the model would have resulted.

We conclude that 4*D* assimilation of incomplete atmospheric data will in some cases improve and in some cases impair the solution of a numerical prediction model. Nudging of only the wind field or the temperature field but not both to observational data will often produce an unbalanced state which drives the model solution away from rather than toward the observed state. Only if both wind velocity and thermodynamic information can be assimilated together can 4*D* assimilation be expected to work in the general case.

Acknowledgement. This research was supported by Air Force contract no. F19678-87-C-0182.

Unclassified
SECURITY CLASSIFICATION OF THIS PAGE

REPORT DOCUMENTATION PAGE

1a. REPORT SECURITY CLASSIFICATION Unclassified

1b. RESTRICTIVE MARKINGS

2a. SECURITY CLASSIFICATION AUTHORITY

2b. DECLASSIFICATION / DOWNGRADING SCHEDULE

3 DISTRIBUTION / AVAILABILITY OF REPORT approved for public release; distribution unlimited

4 PERFORMING ORGANIZATION REPORT NUMBER(S)

5. MONITORING ORGANIZATION REPORT NUMBER(S) AFGL-TR-89-0011

6a. NAME OF PERFORMING ORGANIZATION ASTeR, INC.

6b OFFICE SYMBOL *(If applicable)*

7a. NAME OF MONITORING ORGANIZATION Air Force Geophysics Laboratory

6c. ADDRESS *(City, State, and ZIP Code)*
P.O. BOX 466
FORT COLLINS, CO 80522

7b. ADDRESS *(City, State, and ZIP Code)*
Hanscom AFB
Massachusetts 01731-5000

8a. NAME OF FUNDING / SPONSORING ORGANIZATION

8b. OFFICE SYMBOL *(If applicable)*

9. PROCUREMENT INSTRUMENT IDENTIFICATION NUMBER F19628-87-C-0182

8c. ADDRESS *(City, State, and ZIP Code)*

10 SOURCE OF FUNDING NUMBERS

PROGRAM ELEMENT NO.	PROJECT NO.	TASK NO.	WORK UNIT ACCESSION NO.
62101F	6670	19	AA

11. TITLE *(Include Security Classification)*
A Dynamic Model for Forecasting New Cloud Development

12. PERSONAL AUTHOR(S)
Cotton, William R.; McAnelly, Ray; Tremback, Craig; Walko, Robert

13a. TYPE OF REPORT Final Report

13b. TIME COVERED FROM 11/01/87 TO 12/19/88

14. DATE OF REPORT *(Year, Month, Day)* 88/12/19

15. PAGE COUNT 88

16. SUPPLEMENTARY NOTATION

17. COSATI CODES

FIELD	GROUP	SUB-GROUP

18. SUBJECT TERMS *(Continue on reverse if necessary and identify by block number)*
Mesoscale Modeling
Doppler Radar Winds
Computer Simulation Models
Weather Forecasting
Remote Data Assimilation
Convective Cloud Development

19. ABSTRACT *(Continue on reverse if necessary and identify by block number)*

Two versions of RAMS were developed under this project: 1) a 3-D form simplified from the original version to speed up execution; and, 2) a mixed-layer model developed from scratch and grafted into the RAMS framework. Schemes for assimilating Doppler-observed horizontal winds, either in radial or cartesian component form, were devised and added to both models. Simulations were run with the assimilation of idealized wind data to test the response of each model to the assimilation, and with the assimilation of real observed wind data from three separate convection cases from CINDE to test the models' ability to forecast the convection using assimilated data. The idealized assimilation experiments demonstrated that wind data assimilation is often unsuccessful if simultaneous assimilation of temperature data is not done. If the assimilated wind field contains features generated by temperature anomalies, such as a cold thunderstorm outflow, which are not (continued on reverse)

20. DISTRIBUTION / AVAILABILITY OF ABSTRACT
☒ UNCLASSIFIED/UNLIMITED ☐ SAME AS RPT ☐ DTIC USERS

21. ABSTRACT SECURITY CLASSIFICATION Unclassified

22a. NAME OF RESPONSIBLE INDIVIDUAL Gerald Freeman, Capt, USAF

22b. TELEPHONE *(Include Area Code)*

22c. OFFICE SYMBOL GL/LYR

DD FORM 1473, 84 MAR

83 APR edition may be used until exhausted.
All other editions are obsolete.

SECURITY CLASSIFICATION OF THIS PAGE
Unclassified

contained in the model temperature field, the model responds to the wind data assimilation in a manner not in agreement with the actual fields. The CINDE cases simulated all fell into this category as they contained significant temperature anomalies.